



National Library
of Canada

Acquisitions and
Bibliographic Services Branch

395 Wellington Street
Ottawa, Ontario
K1A 0N4

Bibliothèque nationale
du Canada

Direction des acquisitions et
des services bibliographiques

395, rue Wellington
Ottawa (Ontario)
K1A 0N4

Your file Votre référence

Our file Notre référence

NOTICE

The quality of this microform is heavily dependent upon the quality of the original thesis submitted for microfilming. Every effort has been made to ensure the highest quality of reproduction possible.

If pages are missing, contact the university which granted the degree.

Some pages may have indistinct print especially if the original pages were typed with a poor typewriter ribbon or if the university sent us an inferior photocopy.

Reproduction in full or in part of this microform is governed by the Canadian Copyright Act, R.S.C. 1970, c. C-30, and subsequent amendments.

AVIS

La qualité de cette microforme dépend grandement de la qualité de la thèse soumise au microfilmage. Nous avons tout fait pour assurer une qualité supérieure de reproduction.

S'il manque des pages, veuillez communiquer avec l'université qui a conféré le grade.

La qualité d'impression de certaines pages peut laisser à désirer, surtout si les pages originales ont été dactylographiées à l'aide d'un ruban usé ou si l'université nous a fait parvenir une photocopie de qualité inférieure.

La reproduction, même partielle, de cette microforme est soumise à la Loi canadienne sur le droit d'auteur, SRC 1970, c. C-30, et ses amendements subséquents.

Canada

University of Alberta

A CO₂ Laser Burst Excitation Technique for Deep Penetration Welding

by

Stefan W. C. Scott



**A thesis submitted to the Faculty of Graduate Studies and Research in partial fulfillment
of the requirements for the degree of Doctor of Philosophy**

Department of Electrical Engineering

Edmonton, Alberta

Spring, 1996



National Library
of Canada

Acquisitions and
Bibliographic Services Branch

395 Wellington Street
Ottawa, Ontario
K1A 0N4

Bibliothèque nationale
du Canada

Direction des acquisitions et
des services bibliographiques

395, rue Wellington
Ottawa (Ontario)
K1A 0N4

Your file Votre référence

Your file Votre référence

The author has granted an irrevocable non-exclusive licence allowing the National Library of Canada to reproduce, loan, distribute or sell copies of his/her thesis by any means and in any form or format, making this thesis available to interested persons.

L'auteur a accordé une licence irrévocable et non exclusive permettant à la Bibliothèque nationale du Canada de reproduire, prêter, distribuer ou vendre des copies de sa thèse de quelque manière et sous quelque forme que ce soit pour mettre des exemplaires de cette thèse à la disposition des personnes intéressées.

The author retains ownership of the copyright in his/her thesis. Neither the thesis nor substantial extracts from it may be printed or otherwise reproduced without his/her permission.

L'auteur conserve la propriété du droit d'auteur qui protège sa thèse. Ni la thèse ni des extraits substantiels de celle-ci ne doivent être imprimés ou autrement reproduits sans son autorisation.

ISBN 0-612-10635-7

Canada

University of Alberta

Library Release Form

Name of Author: Stefan William Craig Scott

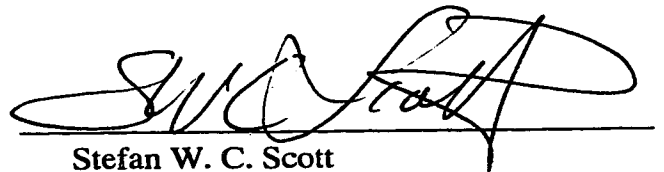
Title of Thesis: A CO₂ Laser Burst Excitation Technique for Deep Penetration Welding.

Degree: Doctor of Philosophy

Year this Degree is Granted: 1996

Permission is hereby granted to the University of Alberta Library to reproduce single copies of this thesis and to lend or sell such copies for private, scholarly, or scientific research purposes only.

The author reserves all other publication and other rights in association with the copyright in the thesis, and except as hereinbefore provided, neither the thesis nor any substantial portion thereof may be printed or otherwise reproduced in any material form whatever without the author's prior written permission.

A handwritten signature in black ink, appearing to read 'Stefan W. C. Scott', written over a horizontal line.

Stefan W. C. Scott
9828 - 81 Avenue
Edmonton, AB
T6E 1W3

April 15, 1996

University of Alberta

Faculty of Graduate Studies and Research

The undersigned certify that they have read, and recommended to the Faculty of Graduate Studies and Research for acceptance, a thesis entitled A CO₂ Laser Burst Excitation Technique for Deep Penetration Welding submitted by Stefan William Craig Scott in partial fulfillment of the requirements for the degree of Doctor of Philosophy.




Dr. H. J. J. Seguin (Supervisor)



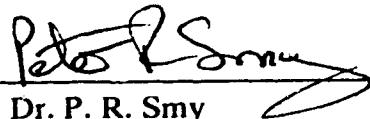
Dr. C. E. Capjack



Dr. R. P. W. Lawson



Dr. B. M. Patchett



Dr. P. R. Smy



Dr. W. M. Steen (External Examiner)

Date:

April 16/96

Dedication

*To Lisa, my family and all my friends for their patience,
support and encouragement.*

Abstract

The carbon dioxide laser has assumed a dominant role in the materials processing industry. In general, this dominance has principally been in substrate cutting applications. High capital and operating costs associated with multi-kilowatt continuous wave laser systems have thus far significantly limited their application for heavy section welding. Extension of the operating limitations of lower power laser systems, through optical pulsing techniques, represents a potential solution to this problem. Currently, pulsed carbon dioxide laser systems are available in high peak power, short pulse duration configurations. While such lasers have enjoyed broad utilization in a number of industries, insufficient average laser power has largely excluded them from deep-penetration welding applications.

The purpose of this research is to extend the concepts discussed above to a laser process which is capable of providing high peak power and high average power simultaneously. Modification of the excitation parameters of a photo-initiated, impulse-enhanced, electrically-excited carbon dioxide laser has yielded a major enhancement in system flexibility and overall utility.

Burst excitation of this system produced pulse shapes ranging from triangular to square having peak powers as much as 6 times the mean level. The temporal nature of the optical output was found to be independent of the average power level. Empirical expressions were derived which describe the relationship between burst frequency, number of pulses per burst, energy per pulse, peak power and optical duty cycle. Ultimately, these

expressions could be extended to the development of a pulsed laser welding specification.

Welding performance of this technique was investigated with respect to penetration depth. When compared to continuous wave weld penetration, burst welding was found to offer significant enhancement. Greatest gains were observed at low average power levels where burst welds produced in excess of 400% greater penetration than continuous wave welds at the same average power level. Burst welds were also found to yield improved weld profiles with narrow side-walls, as compared to continuous wave welds. Finally, a reduction in plasma suppression requirements is indicated through lack of steady state plasma formation during pulse-periodic welding.

Acknowledgment

I would like to take this opportunity to thank a number of people whose input has contributed significantly to this research. First and foremost, I would like to thank Dr. H. J. J. Seguin for his support, guidance and enthusiasm in my work.

Additional thanks goes to all the members of the high power laser group at the University of Alberta. Mr. H. W. Reshef is thanked for his assistance with all the complex systems involved in this work as well as for numerous insights into a wide variety of topics. Appreciation goes to Mr. D. Presakarchuk for his input on electrical systems and Mr. V. Pohnert for his assistance with CAD. Thanks go to Mr. H. Dixel for his expertise in machining numerous components and to Mr. K. Rogozinski for his welding knowledge and operation of the laser system.

I would also like to thank Dr. W. D. Bilida and Mr. J. D. Strohschein for their interest, participation and countless discussions in aid of this research.

Table of Contents

Chapter 1

Introduction	1
1.1 Principles of Laser Operation	4
1.2 The CO ₂ Laser	5
1.2.1 CO ₂ Laser Excitation	6
1.2.2 Physical Gas Laser Geometries	7
1.3 Pulsing Processes	9
1.3.1 Gated and Electronic Pulsing.....	10
1.3.2 Super-pulse or Enhanced-pulse Operation	11
1.3.3 Hyperpulse or CW with Super-pulses	15
1.4 Laser Welding	16
1.4.1 Continuous Wave Welding	17
1.4.2 Pulsed Welding	19

Chapter 2

System Components and Development	23
2.1 Laser System Overview	24
2.2 Discharge Systems	26
2.2.1 Grid Driver.....	29
2.2.2 DC Supply Current Monitoring	31
2.3 Optical Beam Handling Systems	38
2.3.1 Beam Delivery System	38
2.3.2 Optical Attenuation System	39
2.4 Optical Monitoring	41
2.4.1 PEM Detector	42
2.4.2 Optical Detector High-speed Low-noise Amplifier.....	44

2.5 Data Acquisition and Processing	48
---	----

Chapter 3

Discharge and Optical Performance	50
3.1 Data Collection	50
3.2 System Trends.	52
3.3 Discharge Characteristics	52
3.4 Optical Characteristics	56
3.5 Optical Results	61
3.6 Empirical Relationships	63
3.6.1 D_o Development.....	64
3.6.2 P_p Development	68
3.7 Empirical Relation Tests	70
3.7.1 Optical Duty Cycle Test	70
3.7.2 Peak Power Test.....	71
3.8 Discussion	73

Chapter 4

Welding Performance	79
4.1 Data Collection	79
4.2 Weld Trends	82
4.2.1 Weld Penetration and Burst Frequency	91
4.2.2 Weld Penetration and Welding Speed.	94
4.2.3 Comparison of CW and Burst Penetration Performance	95
4.2.4 Extension to High Average Power Levels	99
4.3 Discussion	101

Chapter 5

Conclusions and Proposals for Future Research	102
5.1 Summary of this Investigation	102
5.2 Proposals for Future Research	106
 References	 109
 Appendix A	 117

List of Tables

Table 2.1:	PIE IV laser system simplified discharge schematic component values, Figure 2.3	28
Table 2.2:	Grid driver block diagram components found in Figure 2.5	30
Table 2.3:	Transmitter circuit and power supply elements in Figure 2.6.	33
Table 2.4:	Receiver circuit components as illustrated in Figure 2.7.	35
Table 2.5:	Optical attenuation system components as shown in Figure 2.12.	40
Table 2.6:	PEM detector amplifier circuit components as found in Figure 2.14	45
Table 3.1:	Optical and discharge current data collection grid summary for the 3 power levels collected. Optical and current data taken at each combination of f_b and N.	51
Table 3.2:	Best fit linear relationships for all power levels.	67
Table 4.1:	Burst frequency and N combinations for laser welds performed in the complete study. Welds were performed at each combination of f_b and N at 2, 4 and 6kW laser power and 8, 12 and 16 mm/sec. welding speed.	80

List of Figures

Figure 1.1:	Laser discharge cavity schematic illustrating random and axial photon emission.	5
Figure 1.2:	Energy level diagram for the CO ₂ laser.	6
Figure 1.3:	Schematic representation of laser optical output with respect to time for gated or electronic pulsing.	10
Figure 1.4:	Schematic representation of laser optical output with respect to time for super-pulse or enhanced-pulse operation.	14
Figure 1.5:	Schematic representation of laser optical output with respect to time for super-pulses applied to the rising edge of a gated pulse.	14
Figure 1.6:	Schematic representation of laser optical output with respect to time for super-pulse superimposed on a CW level.	15
Figure 1.7:	Schematic representation of the keyhole welding process.	17
Figure 2.1:	Simplified block diagram of the systems involved in this study.	24
Figure 2.2:	PIE IV simplified mechanical schematic; (1) vacuum enclosure, (2) blower drive, (3) blower blades, (4) flow transition unit, (5) heat exchangers, (6) bailast delivery system, (7) multi-element electrode blocks, (8) vibration isolation optical bench, (9) discharge region.	25
Figure 2.3:	PIE IV simplified discharge system schematic. Component values given in Table 2.1.	27
Figure 2.4:	Grid driver output pulse stream; (A) CW excitation, (B) Burst excitation with N=7.	29
Figure 2.5:	Simplified Block diagram on digital grid oscillator/grid driver circuit. Component details are supplied in Table 2.2	30
Figure 2.6:	DC pumping supply current monitoring apparatus; (A) High voltage current monitor and transmitter, (B) Regulated Battery DC supply. Component values are given in Table 2.3	32
Figure 2.7:	High voltage current receiver. Component values given in Table 2.4	34

Figure 2.8: Current monitor receiver amplifier gain with respect to operating frequency.	36
Figure 2.9: Current monitor receiver amplifier phase with respect to operating frequency.	36
Figure 2.10: Spectral energy density for a typical current waveform. Significant harmonic content is contained below 20 kHz. Harmonic effect of 5 kHz pulser repetition is also evident. Current waveform: $P_{av}=4kW$, $f_b=200$ Hz and $N=3$	37
Figure 2.11: Optical beam delivery system.	38
Figure 2.12: Optical attenuation system.	40
Figure 2.13: PEM detector schematic	43
Figure 2.14: Optical detector high-speed, low-noise amplifier schematic.	45
Figure 2.15: PEM detector amplifier gain with respect to operating frequency.	46
Figure 2.16: PEM detector amplifier phase with respect to operating frequency.	46
Figure 2.17: Spectral energy density for a typical optical waveform. Significant harmonic content is contained below 20 kHz. Harmonic effect of 5 kHz pulser repetition is also evident. Optical waveform: $P_{av}=4kW$, $f_b=200$ Hz and $N=3$	47
Figure 3.1: 2 kW average power pulsed optical output, (A) 75 Hz, 7 pulses, (B) 75 Hz, 27 pulses (C) 200 Hz & 3 pulses, (D) 357 Hz & 3 pulses, (E) CW.	53
Figure 3.2: 4 kW average power pulsed optical output, (A) 75 Hz, 7 pulses, (B) 75 Hz, 27 pulses (C) 200 Hz & 3 pulses, (D) 357 Hz & 3 pulses, (E) CW.	54
Figure 3.3: 6 kW average power pulsed optical output, (A) 75 Hz, 7 pulses, (B) 75 Hz, 27 pulses (C) 200 Hz & 3 pulses, (D) 357 Hz & 3 pulses, (E) CW.	55
Figure 3.4: Discharge voltage and current with respect to f_b . $P_{av}=4kW$, $N=7$	56
Figure 3.5: 4 kW Optical output and discharge Current, $f_b=75$ Hz, $N=7$	57
Figure 3.6: 4 kW Optical output and discharge Current, $f_b=75$ Hz, $N=27$	58
Figure 3.7: 4 kW Optical output and discharge Current, $f_b=200$ Hz, $N=3$	58
Figure 3.8: 4 kW Optical output and discharge Current, $f_b=357$ Hz, $N=3$	59
Figure 3.9: 4 kW CW Optical output and discharge current.	59

Figure 3.10: Dependence of laser peak and offset power on burst frequency and average laser power for 7 pulses.	63
Figure 3.11: Peak laser power with respect to optical duty cycle at 4 kW average power.	65
Figure 3.12: Dependence of optical duty cycle on burst frequency and average laser power for the case of 7 pulses.	65
Figure 3.13: Optical duty cycle with respect to number of pulses at an average power of 4kW.	66
Figure 3.14: Optical duty cycle vs. N slope with respect to burst frequency.	67
Figure 3.15: Average peak laser power with respect to energy per pulse for all three power levels.	69
Figure 3.16: Average S_f with respect to E_p at the three power levels in question. Solid lines represent the distinct pulse regime, dashed lines indicate higher frequency operation.	70
Figure 3.17: Optical duty cycle as a function of number of pulses and burst frequency at an average power level of 2 kW. Points are experimental data and solid lines represent (3.6).	71
Figure 3.18: Optical duty cycle as a function of number of pulses and burst frequency at an average power level of 4 kW. Points are experimental data and solid lines represent (3.6).	72
Figure 3.19: Optical duty cycle as a function of number of pulses and burst frequency at an average power level of 6kW. Points are experimental data and solid lines represent (3.6).	73
Figure 3.20: D_o with respect to E_p and average laser power at a burst duty cycle of 10%. Points are experimental data and solid lines represent (3.6).	74
Figure 3.21: D_o with respect to E_p and average laser power at a burst duty cycle of 20%. Points are experimental data and solid lines represent (3.6).	74
Figure 3.22: D_o with respect to E_p and average laser power at a burst duty cycle of 40%. Points are experimental data and solid lines represent (3.6).	75
Figure 3.23: Dependence of P_p on E_p at $P_{av} = 2$ kW for $N < 15$. Points are experimental data and the solid line represents empirical (3.7).	75
Figure 3.24: Dependence of P_p on E_p at $P_{av} = 4$ kW for $N < 15$. Points are experimental	

data and the solid line represents empirical (3.7).	76
Figure 3.25: Dependence of P_p on E_p at $P_{av} = 6$ kW for $N < 15$ pulses. Points are experimental data and the solid line represents empirical (3.7).	76
Figure 3.26: P_p with respect to f_b at $P_{av} = 2$ kW with 7 pulses. Points are experimental data and the solid line represents (3.7).	77
Figure 3.27: P_p with respect to f_b at $P_{av} = 4$ kW with 7 pulses. Points are experimental data and the solid line represents (3.7).	77
Figure 3.28: P_p with respect to f_b at $P_{av} = 6$ kW with 7 pulses. Points are experimental data and the solid line represents (3.7).	78
Figure 4.1: 4 kW average power pulse profiles applied to welding in this section; (A) $f_b=75$ Hz, $N=7$, (B) $f_b=75$ Hz, $N=27$, $D_b=40\%$, (C) $f_b=125$ Hz, $N=7$, (D) $f_b=125$ Hz, $N=16$, $D_b=40\%$, (E) $f_b=172$ Hz, $N=7$, (F) $f_b=172$ Hz, $N=12$, $D_b=40\%$,	83
Figure 4.2: 4 kW Burst welds performed at $f_b=75$ Hz, $N=7$; (A) 8 mm/sec., (B) 12 mm/sec., (C) 16 mm/sec. 4.7x Magnification.	84
Figure 4.3: 4 kW Burst welds performed at $f_b=75$ Hz, $N=27$; (A) 8 mm/sec., (B) 12 mm/sec., (C) 16 mm/sec. 4.7x Magnification.	86
Figure 4.4: 4 kW Burst welds performed at $f_b=125$ Hz, $N=7$; (A) 8 mm/sec., (B) 12 mm/sec., (C) 16 mm/sec. 4.7x Magnification.	87
Figure 4.5: 4 kW Burst welds performed at $f_b=125$ Hz, $N=16$; (A) 8 mm/sec., (B) 12 mm/sec., (C) 16 mm/sec. 4.7x Magnification.	88
Figure 4.6: 4 kW Burst welds performed at $f_b=172$ Hz, $N=7$; (A) 8 mm/sec., (B) 12 mm/sec., (C) 16 mm/sec. 4.7x Magnification.	88
Figure 4.7: 4 kW Burst welds performed at $f_b=172$ Hz, $N=12$; (A) 8 mm/sec., (B) 12 mm/sec., (C) 16 mm/sec. 4.7x Magnification.	89
Figure 4.8: CW welds performed at; (A) 8 mm/sec., (B) 12 mm/sec., (C) 16 mm/sec. 4.7x Magnification.	90
Figure 4.9: Weld penetration with respect to burst frequency at $N = 7$ and $v = 8$ mm/sec.	91
Figure 4.10: Weld penetration with respect to burst frequency at $N = 7$ and $v = 12$ mm/sec.	92

Figure 4.11: Weld penetration with respect to burst frequency at $N = 7$ and $v = 16$ mm/sec.	93
Figure 4.12: Weld penetration with respect to weld speed at $P_{av} = 2$ kW.	94
Figure 4.13: Weld penetration with respect to weld speed at $P_{av} = 4$ kW.	95
Figure 4.14: Weld penetration with respect to weld speed at $P_{av} = 6$ kW.	96
Figure 4.15: Penetration performance difference between Burst and CW welds with respect to welding speed.	97
Figure 4.16: 6 kW laser welds, $v = 8$ mm/sec.; (A) CW weld, (B) burst weld with $f_b = 75$ and $N = 13$. Magnification = 4.7x.	98
Figure 4.17: CW weld micrograph, $P_{av} = 9$ kW, $v = 7$ mm/sec.	100
Figure 4.18: Burst weld micrograph, $P_{av} = 9$ kW, $f_b = 200$ Hz, $N = 7$, $v = 7$ mm/sec. .	100
Figure A.1: PIE IV Laser system illustrating the operators console, welding head, X-Y table and system controls.	117
Figure A.2: Laser welding head illustrating beam handling optics, welding nozzle, X-Y table, and weld sample mount.	118
Figure A.3: Laser pulser control box illustrating the oil immersed hydrogen thyatron, pulse capacitors pulse transformers and high voltage connections.	119
Figure A.4: Typical laser beam burn pattern in fire brick.	120
Figure A.5: Optical bench safety enclosure illustrating the beam delivery and optical attenuation system.	121
Figure A.6: Overhead view of the optical attenuation system and PEM detector apparatus.	122

List of Symbols

A	amperage
AC	alternating current
Ar	argon
B	magnetic field
CW	continuous wave
C	capacitor / capacitance
CN	counter
CO ₂	carbon dioxide
dB	decibels
D	diode, beam diameter or clear aperture
D _b	burst duty cycle
D _o	optical duty cycle
DC	direct current
E	energy
E _p	energy per pulse
f	frequency
<i>f</i>	focal length
<i>f</i> [#]	numerical f-number of a lens or mirror.
f _b	burst frequency
F	farads
FWHM	full width at one half maximum

G	logic gate
He	helium
HeNe	helium neon
Hz	hertz
J	joules
L	inductance / inductor
L_n	lens
M	voltage regulator
MCT	mercury cadmium telluride
MMI	man machine interface
MR	mirror
N	number of pulses per burst cycle
N₂	nitrogen
P	power
P_{av}	average laser power
P_p	peak laser power
P_{therm}	thermal offset power
PEM	photo-electromagnetic
PIE	photo-initiated impulse-enhanced electrically-excited
Q	operational amplifier
R	resistance / resistor
RT	room temperature
S	switch

S_f	shape factor
SCR	silicone controlled rectifier
T	coaxial cable
TEA	transversely excited atmospheric
T_a	ambient temperature
T_b	boiling temperature
T_m	melting temperature
Tx	transformer
UV	ultra-violet
v	welding speed
V	voltage
VA	volt amps
W	watts
ZnSe	zinc selenide
α	slope
β	y intercept
χ	power scaling factor
Λ	scaling factor
Ω	ohms
$^\circ$	degrees

Chapter 1

Introduction

Since its discovery by Patel in 1964¹, the Carbon Dioxide (CO₂) laser has become the dominant laser in the materials processing industry. This fact can be attributed to the high efficiency, high power and flexibility, characteristic of this device. Indeed, the CO₂ laser has had significant impact in a wide variety of applications. Average power systems up to 1 kW have found broad usage in micro-machining, scribing, cutting and medical applications^{2,3}. At average powers on the order of 1 to 5 kW, the CO₂ laser has revolutionized the custom fabrication, metal and textile cutting industries⁴. Until recently, these laser systems have dominated these specific applications in industry. Efficient heavy-section laser welding generally requires power levels in excess of 10 kW. Although systems ranging from 20 to 45 kW^{5,6} have been available, most have suffered from a number of significant limitations.

Based on these considerations, multi-kilowatt continuous wave (CW) CO₂ lasers have had limited application in deep-penetration welding. While such systems are indeed capable of producing excellent quality welds, complexity, lack of flexibility, large physical size and cost have restricted their use. Further, systems capable of producing CW output powers in excess of 10 kW seldom provide control of parameters other than average output power level.

Laser industry trends are towards development of high power, multi-channel, RF

excited laser systems^{7,8}. Here, diffusion cooling and area scaling offer tremendous advantages in terms of system complexity, physical size and reliability. Some of these systems feature superior materials processing characteristics as a result of enhanced beam quality^{9,10}. Currently, the majority of these systems are limited to 1 or 2 kW in maximum output power, thereby excluding them from use in deep-penetration welding. One potential solution to the lack of flexibility of these and traditional high power lasers lies in pulsed operation.

Processing a broader range of materials is now possible with the advent of a number of laser pulsing technologies. Pulsing low power CO₂ lasers with a variety of techniques has considerably enhanced flexibility. Several systems are investigated here in order to differentiate between the pulsing methodologies currently in use for materials processing. These pulsing techniques are referenced with varying nomenclature, including; gain switching, Q-switching, gating, super-pulses, enhanced-pulses and Hyperpulse^{11,12}.

Pulsing techniques for multi-kilowatt lasers are not generally available, due in large measure to the excitation techniques currently available. One CO₂ laser pumping approach which does not suffer such limitations is the Photo-initiated, Impulse-enhanced, Electrically-excited (PIE) system^{13,14,15}. Through manipulation of this unique laser excitation sequence, a wide range of output parameters become amenable to easy control. Parameters generally of interest in laser welding applications are: average power, peak power, duty cycle and pulse shape.

Recently, a new pulsing technique was developed at the University of Alberta based on the PIE laser excitation process. Burst excitation was shown to expand the laser's operating range significantly, through increased discharge stability at high pumping levels^{16,17,18}. One potential advantage of this process lies in the possibility that laser excitation can be controlled in such a manner as to allow manipulation of the peak power, shape and duration of the optical pulse. This system offers tremendous potential in the area of materials processing since the optical output of the laser can be easily modified to suit any number of situations.

The pulsing systems mentioned above all have unique properties which distinguish them from each other. To date, laser pulses with high average and peak power have been explored in little detail with respect to deep penetration welding.

Control of the optical profile of the laser output has the potential to expand the application of CO₂ lasers in the processing of extremely thick metal sections. With the ability to penetrate to great depths, material composition could be altered by addition of alloying elements. This feature, combined with the reduced heat affected zone (HAZ) associated with pulsed laser power, could lead to the creation of welds which no longer represent the "weak spot" in a finished product.

This work focuses on the development of a unique burst excitation technique for CO₂ lasers. The process significantly enhances flexibility of the laser system. Increased laser efficiency, expanded operating range and enhanced welding performance are found to be three major benefits derived through application of this process^{19,20}.

This chapter will present brief background on CO₂ laser dynamics and the essential features of the laser welding process. A summary of common pulsing techniques will also be included to clarify similarities and differences between existing processes and the burst technique considered here.

1.1 Principles of Laser Operation

LASER is an acronym for ‘Light Amplification by Stimulated Emission of Radiation.’ The concept is based on an atom or molecule in a high energy state undergoing a radiative transition to a lower state. Conservation of energy dictates that the energy difference must be released in some form. In the case of a laser constituent, this energy is released in the form of a photon. The process just described is referred to as spontaneous emission. Should the emitted photon interact with another excited atom having the same energy differential between states, a subsequent photon is released. This second photon, by nature of the interaction, has the same phase and frequency of the initial photon. This process is referred to as stimulated emission. Hence the process of cascaded stimulated emission leads to the generation of a great number of photons.

For the process of stimulated emission to dominate, the population of atoms in the upper state must exceed that in the ground state. Under normal equilibrium conditions, this “population inversion” does not exist. Thus, any gain medium within a laser system requires an energy pumping mechanism to create such a population inversion³.

Once a population inversion is established, spontaneous emission occurs in all directions. The majority of these emissions are lost, since they propagate away from the

laser cavity, Figure 1.1. However, a small portion of the emission does propagate perpen-

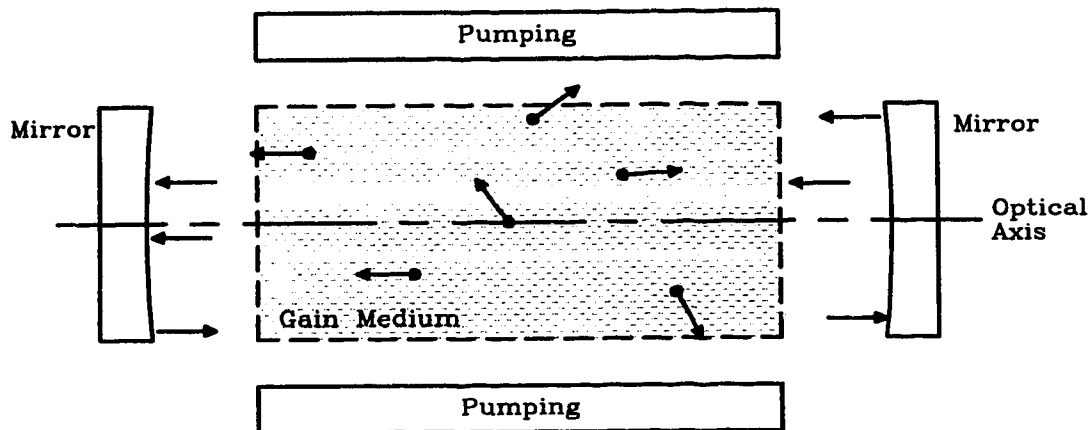


Figure 1.1: Laser discharge cavity schematic illustrating random and axial photon emission.

pendicular to the cavity mirrors. On-axis photons provide the basis for stimulated emission since they experience coherent amplification while passing through the gain media. If the excited gain media is adequate to compensate for losses within the cavity, the oscillations continue to grow. Ultimately, energy is extracted from the laser cavity through coupling techniques related to the mirror properties.

1.2 The CO₂ Laser

As indicated previously, the CO₂ laser has gained dominance in the materials processing industry due to its high efficiency, reliability and high output power capability. The PIE process represents a specific excitation technique developed previously for extended volume CO₂ laser systems. This section will provide background on the CO₂ laser process and the excitation techniques available.

1.2.1 CO₂ Laser Excitation

Figure 1.2 presents the energy level diagram for the 4 level CO₂ laser system. Las-

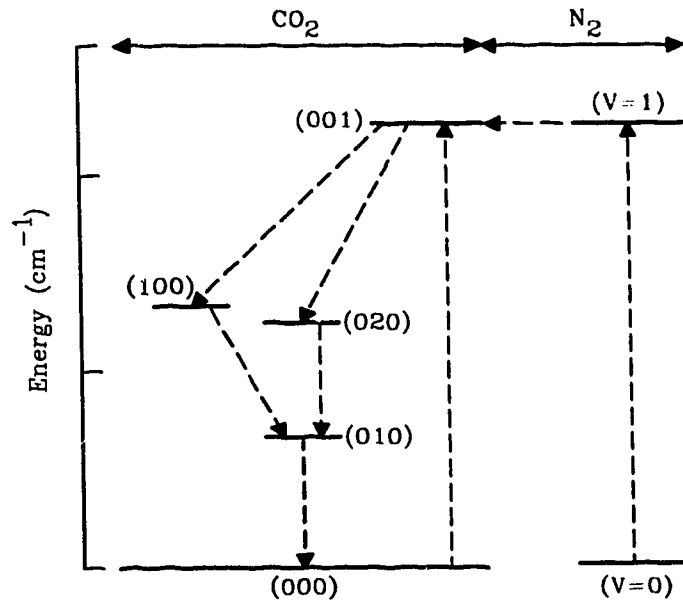


Figure 1.2: Energy level diagram for the CO₂ laser.

ing levels involve different vibrational modes of the CO₂ molecule. The upper laser level (001) is characterized by an asymmetric stretch of the molecule. At (100), symmetric stretch excitation is present. Bending excitation dominates energy levels (020) and (010). The most prevalent laser transition, (001) to (100), has the highest gain and radiates at 10.6 μm . A lower gain transition takes place at the second bending mode (020) and emits 9.6 μm radiation. Radiative decay from (100) and (020) populates the lowest bending mode level, (010). This level is subsequently depopulated through collisional relaxation to the ground state. The energy level diagram for N₂ is also included in Figure 1.2 to illustrate its role in the excitation process. Figure 1.2 demonstrates that the energy of the

excited vibrational state of N_2 is nearly the same energy as the upper CO_2 laser level. Vibrational energy can therefore be efficiently transferred from excited N_2 to CO_2 molecules through in-elastic collisions at this level.

Two techniques are available for exciting a CO_2 laser; direct current (DC) and alternating current (AC). The PIE laser system considered in this study utilizes high power DC electrical energy to provide excitation of the upper laser level. However, the laser-plasma is established and maintained through photo-impulse ionization sequences.

Specifically, under the PIE discharge excitation technique, opposite polarity 10 kV impulses are applied to multi-element, pin electrodes at both anode and cathode structures. A transient corona is formed at the tip of each pin which yields massive ultra-violet (UV) irradiation of the lasing gas mixture. Initially, this radiation photo-ionizes the gas mixture, leading ultimately to avalanche multiplication. Concomitant application of a high voltage DC electric field results in a massive net flow of electrons in this ionized gas mixture. The result is a highly excited gas column, or laser plasma, established between the anode and cathode elements of the structure. Thus, excitation of the lasing gases occurs as they pass through this inter-electrode volume.

1.2.2 Physical Gas Laser Geometries

Early CO_2 lasers were sealed discharge tubes having slow axial gas flow. Under such an arrangement, lasing mixture cooling was accomplished via diffusion to the outer walls of the tube. As such, output power was found to scale only with laser tube length²¹. Thus, high average power levels from such slow-flow axial systems resulted in physical

lengths which were impractical.

A primary limitation in extracting output energy from CW laser systems lies in the temperature rise associated with increased energy input. In the CO₂ laser, this limitation is principally manifest in the lower laser level, since its depopulation rate is heavily dependent upon gas temperature. Gas temperature is a reflection of the balance between input energy and the heat conduction within the gas. Since heat conductivity is independent of gas density, conduction heat transport is fixed for a given maximum gas temperature. This aspect represents the limitation on energy input³.

Increased power can only be obtained through convective cooling by means of gas transport. The addition of high speed convective cooling of the lasing mixture serves to increase the output power of axial systems by removing the hot gas from the discharge region. Here, laser power is found to be a direct function of gas flow velocity²². A drawback of these systems is the cost and complexity of high velocity gas transport compressors.

Introduction of the transverse flow gas transport configuration, where the optical axis, discharge field and gas flow direction are all mutually perpendicular, represents one of the most significant advancements in CO₂ laser design²². Here, gas flow velocity is greatly reduced, compared to an axial-flow geometry. Indeed, this configuration represents the vast majority of 5 kW or larger laser systems available today. The PIE laser system utilized in this study incorporates such a transverse-flow geometry.

1.3 Pulsing Processes

Pulsed operation of CO₂ lasers provides a number of advantages over CW operation. As mentioned previously, increasing laser power depends on gas temperature. The primary solution to this problem lies in gas transport and forced convective cooling. Another potential solution lies in the heat capacity of the medium itself, under pulsed operation. Since heat capacity is proportional to density, the maximum attainable output energy per pulse will be proportional to gas density, up to a thermal limit.

The ability to tailor the temporal profile of the laser energy provides a means to accurately control the energy deposited in materials processing applications. Control of peak power, pulse duration and pulse shape will ultimately effect the properties of processed materials.

In general, pulse duration depends on relaxation of the excited molecules. At higher operating pressures, these relaxation times become shorter. Therefore, pulse length depends on gas pressure. As a result, peak laser power is proportional to the square of the pressure³. Thus, higher peak power pulses with shorter duration are achieved with increasing pressure. This process is well demonstrated by the transversely excited atmospheric (TEA) CO₂ laser²³. In this process, extremely high peak powers with concomitant short pulse durations are possible. Pulsed lasers of this kind are well suited to laser scribing and ablating applications but are limited to situations requiring relatively low average power levels. The highly stable discharge associated with operation below approximately 50 torr is no longer achieved at these high operating pressures. At pressures well in excess of 50 torr the glow discharge often constricts into arcs. Arc discharges are inherently unstable,

non-uniform and therefore unsuitable for excitation of continuous systems. The focus of this study is a PIE laser system operated at 42 torr, well within the stable glow discharge pressure regime.

1.3.1 Gated and Electronic Pulsing

The simplest technique for achieving a pulsed laser output is by gating or chopping the output beam. Such operation may be realized with the aid of a mechanical chopper assembly, which can be physically modified to vary both the frequency and duty cycle of the output beam. Figure 1.3 represents laser output power with respect to time under such

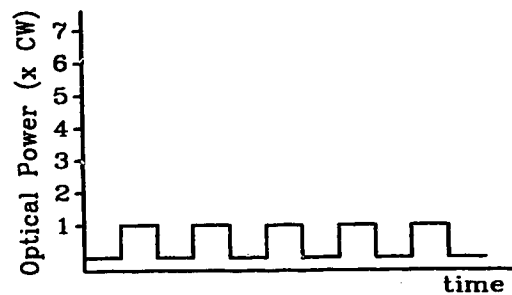


Figure 1.3: Schematic representation of laser optical output with respect to time for gated or electronic pulsing.

a pulsing scheme.

There are a number of significant disadvantages to this approach. First, the average output power is considerably less than at the CW level. Second, pulsing frequency is severely limited by the mechanical nature of the chopper assembly. Further, the chopper or shutter must be physically modified to change output frequency and/or duty cycle.

Mechanical systems are maintenance intensive and prone to calibration problems over time. A gating approach is also incapable of producing pulses or bursts of power since it only modulates the CW beam.

A more sophisticated pulsing approach which produces an output like that in Figure 1.3, is achieved by electronically pulsing the laser discharge itself; essentially turning the laser on and off. In this way, frequency and duty cycle of the resulting output waveform can be easily varied. In fact, the output frequency can be increased to the point where the pulses overlap and an essentially CW beam is produced. Electronic pulsing of this form is still limited, as with a gating system, to output powers which decrease as pulse frequency increases. Varying the electrical excitation within the laser is the basis of all subsequent pulsing methods discussed.

1.3.2 Super-pulse or Enhanced-pulse Operation

The terms super-pulse and enhanced-pulse both refer to an output waveform which achieves high peak power in the range of 2 to 7 times the CW level for a short period of time²⁴. In general, pulses with these characteristics are achieved in two ways with a CO₂ laser. Cavity Q-switching and gain switching are the most common “giant-pulse” laser techniques.

The concept of cavity Q-switching is an extension of techniques developed for high power extraction from low-frequency electronic circuits. Here, energy is stored in a capacitor at a controlled rate limited by a charging resistor. The capacitor is prevented from discharging by an open circuit switch. When the switch is closed, only the imped-

ance of the load limits the capacitor discharge. The important point here is that the peak power delivered to the load can be many times the peak instantaneous power extracted from the source²⁵.

Giant pulses can be created in a laser system by storing energy in a massive population inversion for subsequent use. The limitation here is the spontaneous emission rate which depletes the population inversion. A further complication lies in the fact that spontaneous emission is amplified by the laser cavity. If this process continues, the spontaneous emission will increase to a steady-state level limited only by the pumping rate. To avoid this drain on the population inversion, the laser cavity is prevented from oscillating. In other words, the cavity Q is spoiled to make the loss per pass very high while pumping the upper laser level.

Extraction of the stored energy is accomplished by suddenly lowering cavity loss. Instantaneously, gain in the system greatly exceeds loss and photon intensity rapidly increases. A number of techniques have been utilized for Q-switching in various laser systems. In high power CO₂ applications, an inter-cavity mechanical shutter is a common technique.

The other common form of giant pulse generation is known as gain switching. Here the population inversion derived from pumping builds up at a faster rate than the photon density in the cavity. This technique applies only to laser systems which have a low probability of spontaneous emission. The very low rate of spontaneous emission results in an insufficient number of photons in the laser cavity to start oscillations.

CO₂ lasers are especially well suited to gain switching as they have extremely low spontaneous emission rates. For example, a typical TEA laser has an upper laser level pumping rate essentially equal to the N₂/CO₂ gas kinetic collision rate. At these pressures, the rate is on the order of 10⁸ to 10⁹ sec⁻¹. Conversely, the spontaneous emission rate from the upper laser level of CO₂ is on the order of 0.3 sec⁻¹. As a result it takes many round trips through the laser cavity resonator before the photon density can build up to a level sufficient to affect the population inversion²⁵.

When a CO₂ laser is excited with large, short duration current pulses, it can produce peak power many times the CW level. In this case, energy is being deposited in the lasing gases at a rate which cannot be maintained without exceeding the thermal limit. Beyond this limit, there is no significant increase in laser output power with increasing input power²⁶. To achieve the required rapid electrical breakdown and large current pulses requires discharge voltages many times that of CW operation. If a large initial voltage spike is impressed upon the discharge volume, a current pulse having a relatively short rise time can be achieved. The result is an output pulse of very short duration and intensity much greater than the CW level. Figure 1.4 is an example of a repetitively super-pulsed laser output. It has been shown that pulse energy scales with the total heat capacity of the gas in the active region. Using this fact, the output pulse energy may be written as

$$E = \chi P_{av} t \quad (1.1)$$

where (χP_{av}) is the peak output power and t is pulse duration. The product (χt) has dimensions of time and represents the longest pulse for which any enhancement over the CW operational level would be observable²⁶.

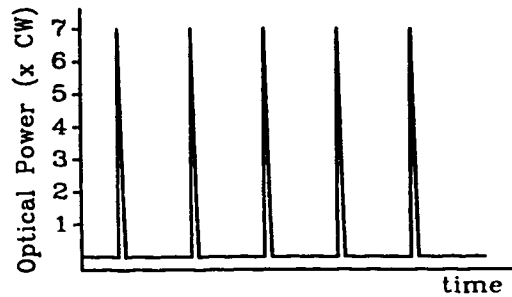


Figure 1.4: Schematic representation of laser optical output with respect to time for super-pulse or enhanced-pulse operation.

A disadvantage of running the laser discharge in this “super-pulsed” mode is that the pulse repetition rate must be sufficiently slow to allow the laser gases to cool in between pulses. Schock showed that as pulse repetition rate increased, laser output power reached a steady state level approaching CW intensity²⁷. Therefore, at the optimum repetition rate, peak power is maintained, but average laser output power is low. Slow repetition rates and low average power lend themselves more to laser drilling and spot welding than to welding or cutting. Another approach involves application of a super-pulse at the leading edge of an electronically gated pulse. This concept is illustrated in Figure 1.5.

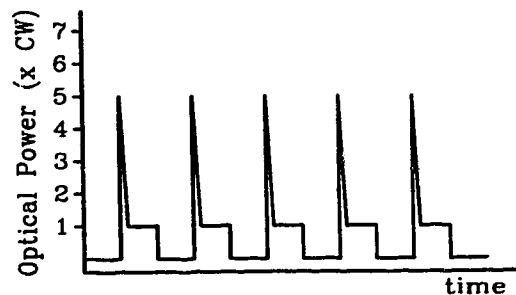


Figure 1.5: Schematic representation of laser optical output with respect to time for super-pulses applied to the rising edge of a gated pulse.

In the case of Figure 1.5, average output power has been increased only slightly. However, the repetition rate can be increased because the laser gas requires less time to recover to the higher average operating level. With such a system, Schwarzenbach achieved 300% of CW operation with 10-150 ms pulses up to a 4 kHz repetition rate²⁸. He further demonstrated that no significant advantage over CW performance was achieved at repetition rates over 2 kHz. This configuration produces an output level slightly higher than for pure gated pulses, but average output power is still lower than CW at low frequencies.

1.3.3 Hyperpulse or CW with Super-pulses

The optimum combination of the above modes, from a materials processing point of view, is demonstrated in Figure 1.6. Super-pulses superimposed on a CW beam com-

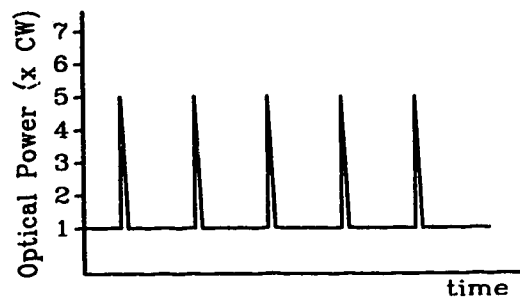


Figure 1.6: Schematic representation of laser optical output with respect to time for super-pulse superimposed on a CW level.

bines the advantages of high peak intermittent power with the high processing speeds of CW operation. One variation on this scheme is patented under the trade name Hyperpulse, a process developed by the PRC Corporation of Landing New Jersey^{11,12}. For the remain-

der of this thesis, super-pulses superimposed on a CW beam will be referred to as Hyperpulse, to distinguish between the above cases.

The result of this combination is a laser output with power equal to or greater than the CW level. Thus, the high peak power characteristic of super-pulsing is combined with the overall high average power of the CW mode. While the Hyperpulse apparatus is patented by the PRC Corporation, the concept of Hyperpulsing with some variation can be found in other references²⁸.

One result of the above work included the application of Hyperpulse CO₂ lasers in processing highly reflective materials^{29,30}. Historically, the CO₂ laser was thought to be ineffective in the processing of non-ferrous metals such as copper and aluminium³¹. These metals possess a high electrical and thermal conductivity and consequent high surface reflectivity in the mid to far infrared. Thus, penetration through such materials requires continuous wave (CW) lasers with extremely high power densities. In the past, cutting of these materials was accomplished with more traditional methods such as water jet or with lasers having more compatible output wavelengths.

1.4 Laser Welding

With the advent of higher average power lasers in the last decade, laser welding applications have grown dramatically. Laser welding is characterized by the application of high energy in a small area. Energy densities on the order of 10^6 W/cm² are common with multi-kilowatt laser systems. Intense optical energy incident on a material surface offers a number of advantages over traditional arc based welding processes. This section will dis-

cuss the general processes in both CW and pulsed laser welding.

1.4.1 Continuous Wave Welding

Deep penetration laser welding requires generation and maintenance of a vapour channel or keyhole throughout the thickness of the material, as illustrated in Figure 1.7.

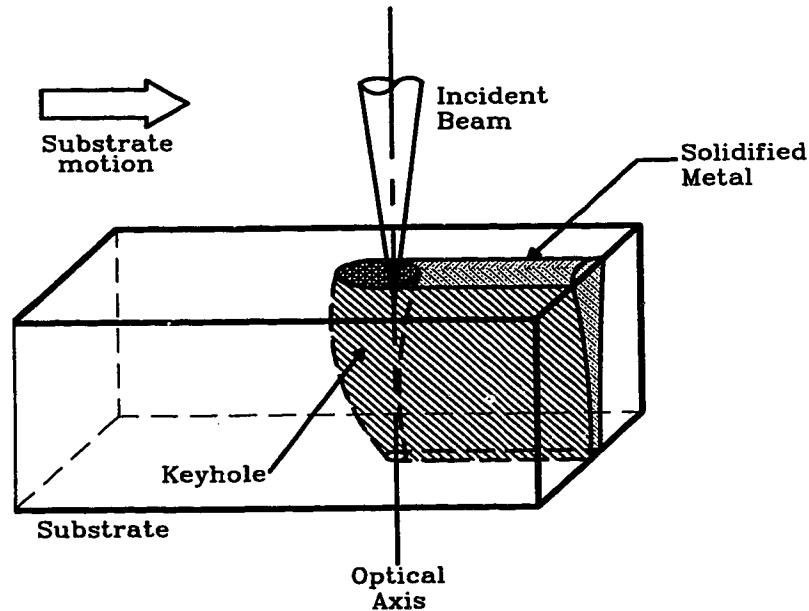


Figure 1.7: Schematic representation of the keyhole welding process.

Impinging CW laser energy must first overcome the surface reflectivity of the substrate. Once the temperature rises above a certain thermal threshold, $10.6\text{ }\mu\text{m}$ energy is rapidly absorbed. At this point, and if sufficient energy density is present in the incident beam, a keyhole quickly forms³². Energy densities on the order of 10^6 W/cm^2 are necessary for formation of the keyhole. Prior to keyhole formation, heat transfer from the beam is through conduction into the substrate bulk. With a stable keyhole, heat transfer occurs through liq-

fluid convection as a result of multiple reflections of the laser beam along the molten walls of the keyhole. Once formed, vapour pressure maintains the keyhole, provided sufficient energy is present in the incident beam. This improved rate of heat transfer via laser-metal-plasma interaction leads to a dramatic improvement in processing rate.

Characteristics of the laser-plasma-substrate interaction are of primary importance when developing laser welding procedures. Welding speed, penetration depth, heat affected zone (HAZ) and resulting microstructure are directly related to these interactions. Dynamics of the melt pool are best demonstrated by first considering CW welding and then comparing these results to a pulse regime.

Basov demonstrated that the behaviour of the vapour-plasma jet in continuous welding is unstable³³. The vapour-plasma phase is removed from the keyhole in a periodic manner at a frequency of several hundred hertz. Thus, transfer of the melt from front to rear of the keyhole is intermittent.

Pulsations detected in welding with a continuous laser beam are explained from a physical point of view by the following considerations. Once a keyhole is formed, the metal at the front of the keyhole is heated from its melting point (T_m) to its boiling point (T_b). During keyhole welding, the primary driving force is the reactive pressure of the vapour phase. Vapour pressure transfers the molten metal from the front of the keyhole towards the rear where it mixes and solidifies. Transfer of the melt is extremely rapid, approaching 1 meter per second, at high welding rates. Since the majority of the melt is removed rapidly, temperature at the front of the keyhole, from which the melt was removed, is approximately T_m . It follows that this surface must be heated to T_b to continue

the melting and transfer of melt during a continuous weld. Therefore, laser welding in the continuous regime can be considered a periodic process.

The intermittent nature of continuous welding processes has also been attributed to blockage caused by the plasma phase formed at the material surface. This problem has been controlled to some extent through introduction of plasma suppression gases such as helium. Results have shown that gas suppression must be applied at high pressures to be effective. Such pressures can cause detrimental mechanical effects upon the melt pool, thereby reducing the overall quality of the resulting weld. One efficient method of preventing the development of the plasma jet is periodic interruption of the laser radiation.

1.4.2 Pulsed Welding

During pulse-periodic laser welding at least five parameters act independently on the substrate: mean power, peak power, pulse duration, pulse frequency, and pulse shape. With this in mind, it can be assumed that the pulse periodic regime has four or more degrees of freedom than continuous operation in which only average power is regulated. All these factors have a significant effect on the formation, maintenance and re-solidification of the melt pool.

It is well known that carbon steel laser welding processes are hampered by high initial reflectivity of the metallic substrate to 10.6 μm radiation. As mentioned, reflection continues until sufficient energy is absorbed to raise the material temperature to a more efficient energy absorption point. As such, higher peak power in the incident beam results in a more rapid absorption of energy, as compared to steady state application of power. Rapid

absorption and subsequent vaporization of the substrate is a characteristic of all “giant-pulse” laser processes. In most lasers, these processes are limited to ablating or scribing the material surface, due to lack of energy in the pulse. Such systems are incapable of deep penetration welding, since they are unable to form and maintain a stable keyhole.

During pulse-periodic irradiation, behaviour of the melt both during the pulse and in the inter-pulse period differs markedly. Drobyazko investigated movement of the melt under the effect of averaged forces during the pulse repetition time and periods between pulses³⁴. High speed photography allowed observation of molten material dynamics during the entire sequence of pulse application.

Under the action of a pulse, the melt pool acts in a manner similar to that described for continuous wave welding. Figure 1.7 depicts that the front wall of the keyhole is inclined in the direction of processing. Flow of the melt is horizontal to the substrate surface, flowing to the back of the keyhole where it mixes and solidifies.

During the period between pulses, melt dynamics change drastically. After a slight delay, the melt moves rapidly from the rear wall of the keyhole to the front, decreasing in speed as re-solidification takes place. Drobyazko observed that in the initial period after the pulse, the front wall of the keyhole solidified at a higher rate than the rear wall. The reverse movement of the melt started after maximum temperature was reached at the rear wall of the keyhole. These results were attributed to capillary forces, which caused reverse movement of the liquid metal after the pulse³⁴.

Efficient energy coupling to the substrate is of primary importance when deep pen-

etration is desired. As discussed earlier, the problem of surface plasma beam absorption is significantly reduced in the pulse periodic regime. At carefully chosen repetition rates, the plasma will recombine prior to onset of the next pulse. A certain finite time is also required for formation of the plasma jet. Therefore, for a significant portion of the laser pulse, the beam is not subjected to any plasma interference. Consequently, plasma suppression gas requirements are reduced, thereby effecting a significant cost savings.

From the above discussions, it can easily be inferred that higher peak power (P_p) in the incident beam leads to more rapid keyhole formation, for a given focal spot size. This aspect conveys the benefits derived through the burst excitation technique, which constitutes the essence of this thesis.

Burst excitation enhanced welding is unique in comparison to existing laser processes. Current literature on high power pulsed laser welding stresses two main areas; high repetition rate application of high peak power, low average power pulse trains^{24,27,28} and gated operation of CW laser systems^{35,36}. These concepts are not easily applied to deep penetration welding, due to a lack of average power. As discussed previously, maintaining an economical welding rate in heavy metal sections necessitates formation of a keyhole in the material. Critical factors in establishing and maintaining such a keyhole are peak intensity and average power. Burst operation of the PIE system considered here produces variable duty cycle, pulse periodic output with high peak power at multi-kilowatt average power levels.

Technological excitation limitations in existing high power lasers restrict the range of temporal optical outputs. Burst excitation provides a means to create a wide variety of

optical output pulse shapes. It has been suggested that in under certain pulse conditions weld solidification may ensue prior to completion of a laser pulse. Under these conditions, it may be possible to control the weld properties through manipulation of the temporal profile of the laser pulse^{37,38,39}.

Chapter 1

Introduction

Since its discovery by Patel in 1964¹, the Carbon Dioxide (CO₂) laser has become the dominant laser in the materials processing industry. This fact can be attributed to the high efficiency, high power and flexibility, characteristic of this device. Indeed, the CO₂ laser has had significant impact in a wide variety of applications. Average power systems up to 1 kW have found broad usage in micro-machining, scribing, cutting and medical applications^{2,3}. At average powers on the order of 1 to 5 kW, the CO₂ laser has revolutionized the custom fabrication, metal and textile cutting industries⁴. Until recently, these laser systems have dominated these specific applications in industry. Efficient heavy-section laser welding generally requires power levels in excess of 10 kW. Although systems ranging from 20 to 45 kW^{5,6} have been available, most have suffered from a number of significant limitations.

Based on these considerations, multi-kilowatt continuous wave (CW) CO₂ lasers have had limited application in deep-penetration welding. While such systems are indeed capable of producing excellent quality welds, complexity, lack of flexibility, large physical size and cost have restricted their use. Further, systems capable of producing CW output powers in excess of 10 kW seldom provide control of parameters other than average output power level.

Laser industry trends are towards development of high power, multi-channel, RF

excited laser systems^{7,8}. Here, diffusion cooling and area scaling offer tremendous advantages in terms of system complexity, physical size and reliability. Some of these systems feature superior materials processing characteristics as a result of enhanced beam quality^{9,10}. Currently, the majority of these systems are limited to 1 or 2 kW in maximum output power, thereby excluding them from use in deep-penetration welding. One potential solution to the lack of flexibility of these and traditional high power lasers lies in pulsed operation.

Processing a broader range of materials is now possible with the advent of a number of laser pulsing technologies. Pulsing low power CO₂ lasers with a variety of techniques has considerably enhanced flexibility. Several systems are investigated here in order to differentiate between the pulsing methodologies currently in use for materials processing. These pulsing techniques are referenced with varying nomenclature, including; gain switching, Q-switching, gating, super-pulses, enhanced-pulses and Hyperpulse^{11,12}.

Pulsing techniques for multi-kilowatt lasers are not generally available, due in large measure to the excitation techniques currently available. One CO₂ laser pumping approach which does not suffer such limitations is the Photo-initiated, Impulse-enhanced, Electrically-excited (PIE) system^{13,14,15}. Through manipulation of this unique laser excitation sequence, a wide range of output parameters become amenable to easy control. Parameters generally of interest in laser welding applications are: average power, peak power, duty cycle and pulse shape.

Recently, a new pulsing technique was developed at the University of Alberta based on the PIE laser excitation process. Burst excitation was shown to expand the laser's operating range significantly, through increased discharge stability at high pumping levels^{16,17,18}. One potential advantage of this process lies in the possibility that laser excitation can be controlled in such a manner as to allow manipulation of the peak power, shape and duration of the optical pulse. This system offers tremendous potential in the area of materials processing since the optical output of the laser can be easily modified to suit any number of situations.

The pulsing systems mentioned above all have unique properties which distinguish them from each other. To date, laser pulses with high average and peak power have been explored in little detail with respect to deep penetration welding.

Control of the optical profile of the laser output has the potential to expand the application of CO₂ lasers in the processing of extremely thick metal sections. With the ability to penetrate to great depths, material composition could be altered by addition of alloying elements. This feature, combined with the reduced heat affected zone (HAZ) associated with pulsed laser power, could lead to the creation of welds which no longer represent the "weak spot" in the finished product.

This work focuses on the development of a unique burst excitation technique for CO₂ lasers. The process significantly enhances flexibility of the laser system. Increased laser efficiency, expanded operating range and enhanced welding performance are found to be three major benefits derived through application of this process^{19,20}.

This chapter will present brief background on CO₂ laser dynamics and the essential features of the laser welding process. A summary of common pulsing techniques will also be included to clarify similarities and differences between existing processes and the burst technique considered here.

1.1 Principles of Laser Operation

LASER is an acronym for ‘Light Amplification by Stimulated Emission of Radiation.’ The concept is based on an atom or molecule in a high energy state undergoing a radiative transition to a lower state. Conservation of energy dictates that the energy difference must be released in some form. In the case of a laser constituent, this energy is released in the form of a photon. The process just described is referred to as spontaneous emission. Should the emitted photon interact with another excited atom having the same energy differential between states, a subsequent photon is released. This second photon, by nature of the interaction, has the same phase and frequency of the initial photon. This process is referred to as stimulated emission. Hence the process of cascaded stimulated emission leads to the generation of a great number of photons.

For the process of stimulated emission to dominate, the population of atoms in the upper state must exceed that in the ground state. Under normal equilibrium conditions, this “population inversion” does not exist. Thus, any gain medium within a laser system requires an energy pumping mechanism to create such a population inversion³.

Once a population inversion is established, spontaneous emission occurs in all directions. The majority of these emissions are lost, since they propagate away from the

laser cavity, Figure 1.1. However, a small portion of the emission does propagate perpen-

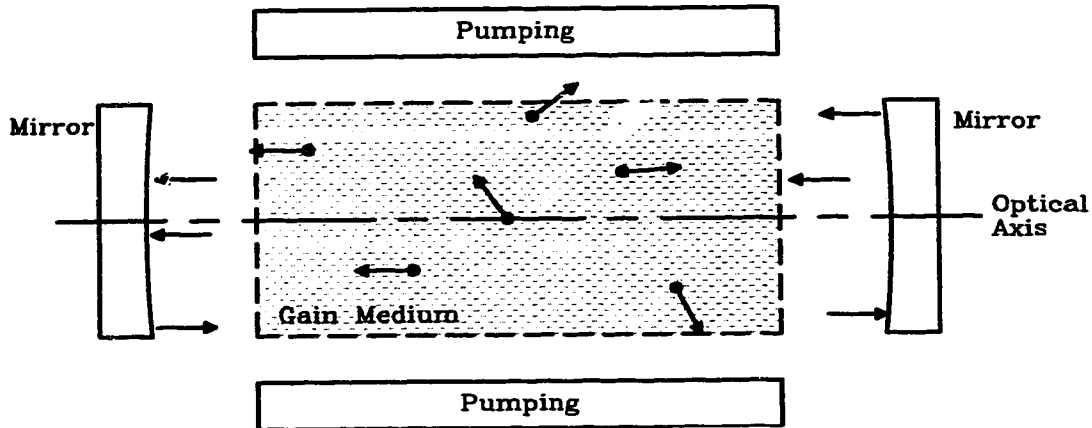


Figure 1.1: Laser discharge cavity schematic illustrating random and axial photon emission.

dicular to the cavity mirrors. On-axis photons provide the basis for stimulated emission since they experience coherent amplification while passing through the gain media. If the excited gain media is adequate to compensate for losses within the cavity, the oscillations continue to grow. Ultimately, energy is extracted from the laser cavity through coupling techniques related to the mirror properties.

1.2 The CO₂ Laser

As indicated previously, the CO₂ laser has gained dominance in the materials processing industry due to its high efficiency, reliability and high output power capability. The PIE process represents a specific excitation technique developed previously for extended volume CO₂ laser systems. This section will provide background on the CO₂ laser process and the excitation techniques available.

1.2.1 CO₂ Laser Excitation

Figure 1.2 presents the energy level diagram for the 4 level CO₂ laser system. Las-

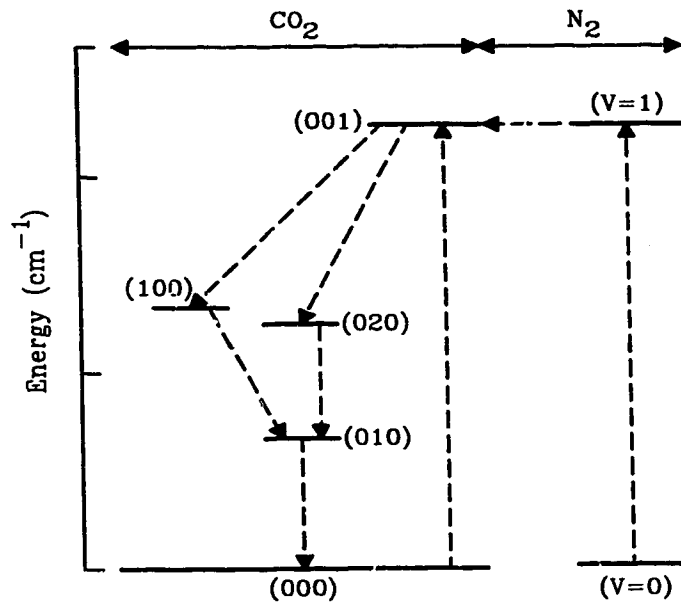


Figure 1.2: Energy level diagram for the CO₂ laser.

ing levels involve different vibrational modes of the CO₂ molecule. The upper laser level (001) is characterized by an asymmetric stretch of the molecule. At (100), symmetric stretch excitation is present. Bending excitation dominates energy levels (020) and (010). The most prevalent laser transition, (001) to (100), has the highest gain and radiates at 10.6 μm . A lower gain transition takes place at the second bending mode (020) and emits 9.6 μm radiation. Radiative decay from (100) and (020) populates the lowest bending mode level, (010). This level is subsequently depopulated through collisional relaxation to the ground state. The energy level diagram for N₂ is also included in Figure 1.2 to illustrate its role in the excitation process. Figure 1.2 demonstrates that the energy of the

excited vibrational state of N_2 is nearly the same energy as the upper CO_2 laser level. Vibrational energy can therefore be efficiently transferred from excited N_2 to CO_2 molecules through in-elastic collisions at this level.

Two techniques are available for exciting a CO_2 laser; direct current (DC) and alternating current (AC). The PIE laser system considered in this study utilizes high power DC electrical energy to provide excitation of the upper laser level. However, the laser-plasma is established and maintained through photo-impulse ionization sequences.

Specifically, under the PIE discharge excitation technique, opposite polarity 10 kV impulses are applied to multi-element, pin electrodes at both anode and cathode structures. A transient corona is formed at the tip of each pin which yields massive ultra-violet (UV) irradiation of the lasing gas mixture. Initially, this radiation photo-ionizes the gas mixture, leading ultimately to avalanche multiplication. Concomitant application of a high voltage DC electric field results in a massive net flow of electrons in this ionized gas mixture. The result is a highly excited gas column, or laser plasma, established between the anode and cathode elements of the structure. Thus, excitation of the lasing gases occurs as they pass through this inter-electrode volume.

1.2.2 Physical Gas Laser Geometries

Early CO_2 lasers were sealed discharge tubes having slow axial gas flow. Under such an arrangement, lasing mixture cooling was accomplished via diffusion to the outer walls of the tube. As such, output power was found to scale only with laser tube length²¹. Thus, high average power levels from such slow-flow axial systems resulted in physical

lengths which were impractical.

A primary limitation in extracting output energy from CW laser systems lies in the temperature rise associated with increased energy input. In the CO₂ laser, this limitation is principally manifest in the lower laser level, since its depopulation rate is heavily dependent upon gas temperature. Gas temperature is a reflection of the balance between input energy and the heat conduction within the gas. Since heat conductivity is independent of gas density, conduction heat transport is fixed for a given maximum gas temperature. This aspect represents the limitation on energy input³.

Increased power can only be obtained through convective cooling by means of gas transport. The addition of high speed convective cooling of the lasing mixture serves to increase the output power of axial systems by removing the hot gas from the discharge region. Here, laser power is found to be a direct function of gas flow velocity²². A drawback of these systems is the cost and complexity of high velocity gas transport compressors.

Introduction of the transverse flow gas transport configuration, where the optical axis, discharge field and gas flow direction are all mutually perpendicular, represents one of the most significant advancements in CO₂ laser design²². Here, gas flow velocity is greatly reduced, compared to an axial-flow geometry. Indeed, this configuration represents the vast majority of 5 kW or larger laser systems available today. The PIE laser system utilized in this study incorporates such a transverse-flow geometry.

1.3 Pulsing Processes

Pulsed operation of CO₂ lasers provides a number of advantages over CW operation. As mentioned previously, increasing laser power depends on gas temperature. The primary solution to this problem lies in gas transport and forced convective cooling. Another potential solution lies in the heat capacity of the medium itself, under pulsed operation. Since heat capacity is proportional to density, the maximum attainable output energy per pulse will be proportional to gas density, up to a thermal limit.

The ability to tailor the temporal profile of the laser energy provides a means to accurately control the energy deposited in materials processing applications. Control of peak power, pulse duration and pulse shape will ultimately effect the properties of processed materials.

In general, pulse duration depends on relaxation of the excited molecules. At higher operating pressures, these relaxation times become shorter. Therefore, pulse length depends on gas pressure. As a result, peak laser power is proportional to the square of the pressure³. Thus, higher peak power pulses with shorter duration are achieved with increasing pressure. This process is well demonstrated by the transversely excited atmospheric (TEA) CO₂ laser²³. In this process, extremely high peak powers with concomitant short pulse durations are possible. Pulsed lasers of this kind are well suited to laser scribing and ablating applications but are limited to situations requiring relatively low average power levels. The highly stable discharge associated with operation below approximately 50 torr is no longer achieved at these high operating pressures. At pressures well in excess of 50 torr the glow discharge often constricts into arcs. Arc discharges are inherently unstable,

non-uniform and therefore unsuitable for excitation of continuous systems. The focus of this study is a PIE laser system operated at 42 torr, well within the stable glow discharge pressure regime.

1.3.1 Gated and Electronic Pulsing

The simplest technique for achieving a pulsed laser output is by gating or chopping the output beam. Such operation may be realized with the aid of a mechanical chopper assembly, which can be physically modified to vary both the frequency and duty cycle of the output beam. Figure 1.3 represents laser output power with respect to time under such

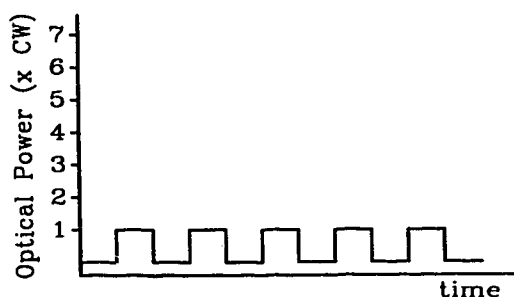


Figure 1.3: Schematic representation of laser optical output with respect to time for gated or electronic pulsing.

a pulsing scheme.

There are a number of significant disadvantages to this approach. First, the average output power is considerably less than at the CW level. Second, pulsing frequency is severely limited by the mechanical nature of the chopper assembly. Further, the chopper or shutter must be physically modified to change output frequency and/or duty cycle.

Mechanical systems are maintenance intensive and prone to calibration problems over time. A gating approach is also incapable of producing pulses or bursts of power since it only modulates the CW beam.

A more sophisticated pulsing approach which produces an output like that in Figure 1.3, is achieved by electronically pulsing the laser discharge itself; essentially turning the laser on and off. In this way, frequency and duty cycle of the resulting output waveform can be easily varied. In fact, the output frequency can be increased to the point where the pulses overlap and an essentially CW beam is produced. Electronic pulsing of this form is still limited, as with a gating system, to output powers which decrease as pulse frequency increases. Varying the electrical excitation within the laser is the basis of all subsequent pulsing methods discussed.

1.3.2 Super-pulse or Enhanced-pulse Operation

The terms super-pulse and enhanced-pulse both refer to an output waveform which achieves high peak power in the range of 2 to 7 times the CW level for a short period of time²⁴. In general, pulses with these characteristics are achieved in two ways with a CO₂ laser. Cavity Q-switching and gain switching are the most common “giant-pulse” laser techniques.

The concept of cavity Q-switching is an extension of techniques developed for high power extraction from low-frequency electronic circuits. Here, energy is stored in a capacitor at a controlled rate limited by a charging resistor. The capacitor is prevented from discharging by an open circuit switch. When the switch is closed, only the imped-

ance of the load limits the capacitor discharge. The important point here is that the peak power delivered to the load can be many times the peak instantaneous power extracted from the source²⁵.

Giant pulses can be created in a laser system by storing energy in a massive population inversion for subsequent use. The limitation here is the spontaneous emission rate which depletes the population inversion. A further complication lies in the fact that spontaneous emission is amplified by the laser cavity. If this process continues, the spontaneous emission will increase to a steady-state level limited only by the pumping rate. To avoid this drain on the population inversion, the laser cavity is prevented from oscillating. In other words, the cavity Q is spoiled to make the loss per pass very high while pumping the upper laser level.

Extraction of the stored energy is accomplished by suddenly lowering cavity loss. Instantaneously, gain in the system greatly exceeds loss and photon intensity rapidly increases. A number of techniques have been utilized for Q-switching in various laser systems. In high power CO₂ applications, an inter-cavity mechanical shutter is a common technique.

The other common form of giant pulse generation is known as gain switching. Here the population inversion derived from pumping builds up at a faster rate than the photon density in the cavity. This technique applies only to laser systems which have a low probability of spontaneous emission. The very low rate of spontaneous emission results in an insufficient number of photons in the laser cavity to start oscillations.

CO₂ lasers are especially well suited to gain switching as they have extremely low spontaneous emission rates. For example, a typical TEA laser has an upper laser level pumping rate essentially equal to the N₂/CO₂ gas kinetic collision rate. At these pressures, the rate is on the order of 10⁸ to 10⁹ sec⁻¹. Conversely, the spontaneous emission rate from the upper laser level of CO₂ is on the order of 0.3 sec⁻¹. As a result it takes many round trips through the laser cavity resonator before the photon density can build up to a level sufficient to affect the population inversion²⁵.

When a CO₂ laser is excited with large, short duration current pulses, it can produce peak power many times the CW level. In this case, energy is being deposited in the lasing gases at a rate which cannot be maintained without exceeding the thermal limit. Beyond this limit, there is no significant increase in laser output power with increasing input power²⁶. To achieve the required rapid electrical breakdown and large current pulses requires discharge voltages many times that of CW operation. If a large initial voltage spike is impressed upon the discharge volume, a current pulse having a relatively short rise time can be achieved. The result is an output pulse of very short duration and intensity much greater than the CW level. Figure 1.4 is an example of a repetitively super-pulsed laser output. It has been shown that pulse energy scales with the total heat capacity of the gas in the active region. Using this fact, the output pulse energy may be written as

$$E = \chi P_{av} t \quad (1.1)$$

where (χP_{av}) is the peak output power and t is pulse duration. The product (χt) has dimensions of time and represents the longest pulse for which any enhancement over the CW operational level would be observable²⁶.

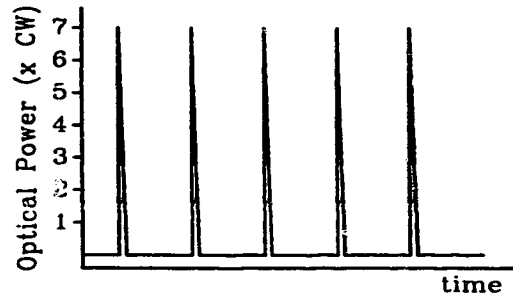


Figure 1.4: Schematic representation of laser optical output with respect to time for super-pulse or enhanced-pulse operation.

A disadvantage of running the laser discharge in this “super-pulsed” mode is that the pulse repetition rate must be sufficiently slow to allow the laser gases to cool in between pulses. Schock showed that as pulse repetition rate increased, laser output power reached a steady state level approaching CW intensity²⁷. Therefore, at the optimum repetition rate, peak power is maintained, but average laser output power is low. Slow repetition rates and low average power lend themselves more to laser drilling and spot welding than to welding or cutting. Another approach involves application of a super-pulse at the leading edge of an electronically gated pulse. This concept is illustrated in Figure 1.5.

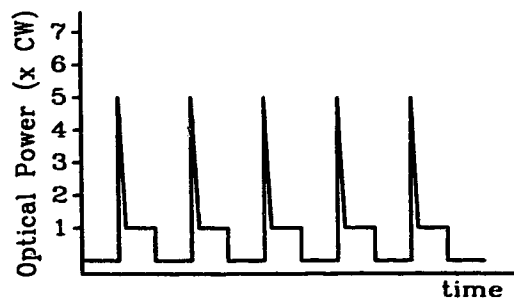


Figure 1.5: Schematic representation of laser optical output with respect to time for super-pulses applied to the rising edge of a gated pulse.

In the case of Figure 1.5, average output power has been increased only slightly. However, the repetition rate can be increased because the laser gas requires less time to recover to the higher average operating level. With such a system, Schwarzenbach achieved 300% of CW operation with 10-150 ms pulses up to a 4 kHz repetition rate²⁸. He further demonstrated that no significant advantage over CW performance was achieved at repetition rates over 2 kHz. This configuration produces an output level slightly higher than for pure gated pulses, but average output power is still lower than CW at low frequencies.

1.3.3 Hyperpulse or CW with Super-pulses

The optimum combination of the above modes, from a materials processing point of view, is demonstrated in Figure 1.6. Super-pulses superimposed on a CW beam com-

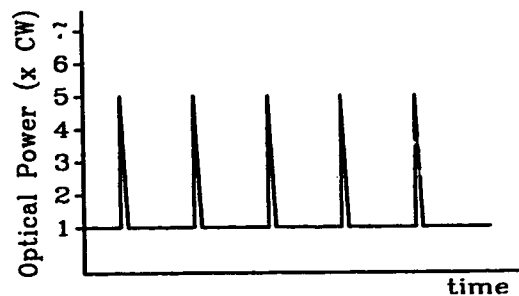


Figure 1.6: Schematic representation of laser optical output with respect to time for super-pulse superimposed on a CW level.

bines the advantages of high peak intermittent power with the high processing speeds of CW operation. One variation on this scheme is patented under the trade name Hyperpulse, a process developed by the PRC Corporation of Landing New Jersey^{11,12}. For the remain-

der of this thesis, super-pulses superimposed on a CW beam will be referred to as Hyperpulse, to distinguish between the above cases.

The result of this combination is a laser output with power equal to or greater than the CW level. Thus, the high peak power characteristic of super-pulsing is combined with the overall high average power of the CW mode. While the Hyperpulse apparatus is patented by the PRC Corporation, the concept of Hyperpulsing with some variation can be found in other references²⁸.

One result of the above work included the application of Hyperpulse CO₂ lasers in processing highly reflective materials^{29,30}. Historically, the CO₂ laser was thought to be ineffective in the processing of non-ferrous metals such as copper and aluminium³¹. These metals possess a high electrical and thermal conductivity and consequent high surface reflectivity in the mid to far infrared. Thus, penetration through such materials requires continuous wave (CW) lasers with extremely high power densities. In the past, cutting of these materials was accomplished with more traditional methods such as water jet or with lasers having more compatible output wavelengths.

1.4 Laser Welding

With the advent of higher average power lasers in the last decade, laser welding applications have grown dramatically. Laser welding is characterized by the application of high energy in a small area. Energy densities on the order of 10^6 W/cm² are common with multi-kilowatt laser systems. Intense optical energy incident on a material surface offers a number of advantages over traditional arc based welding processes. This section will dis-

cuss the general processes in both CW and pulsed laser welding.

1.4.1 Continuous Wave Welding

Deep penetration laser welding requires generation and maintenance of a vapour channel or keyhole throughout the thickness of the material, as illustrated in Figure 1.7.

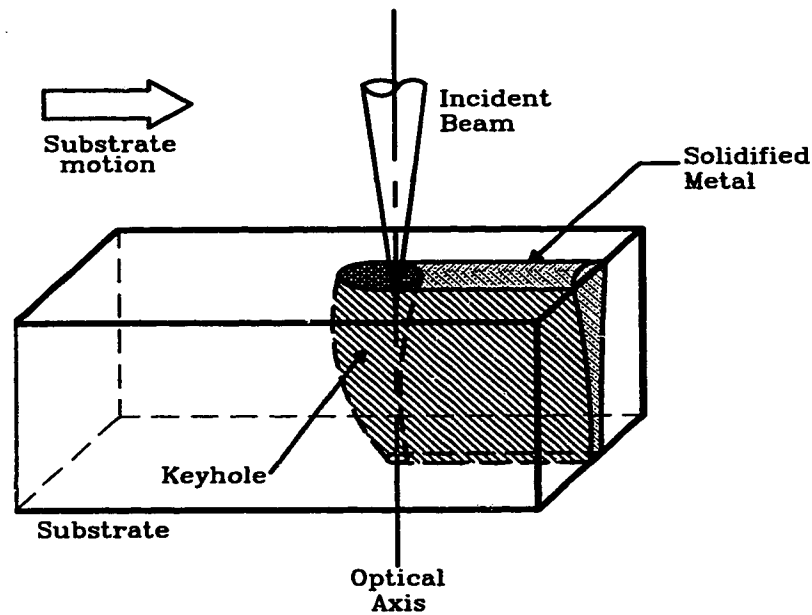


Figure 1.7: Schematic representation of the keyhole welding process.

Impinging CW laser energy must first overcome the surface reflectivity of the substrate. Once the temperature rises above a certain thermal threshold, $10.6\ \mu\text{m}$ energy is rapidly absorbed. At this point, and if sufficient energy density is present in the incident beam, a keyhole quickly forms³². Energy densities on the order of $10^6\ \text{W}/\text{cm}^2$ are necessary for formation of the keyhole. Prior to keyhole formation, heat transfer from the beam is through conduction into the substrate bulk. With a stable keyhole, heat transfer occurs through liq-

uid convection as a result of multiple reflections of the laser beam along the molten walls of the keyhole. Once formed, vapour pressure maintains the keyhole, provided sufficient energy is present in the incident beam. This improved rate of heat transfer via laser-metal-plasma interaction leads to a dramatic improvement in processing rate.

Characteristics of the laser-plasma-substrate interaction are of primary importance when developing laser welding procedures. Welding speed, penetration depth, heat affected zone (HAZ) and resulting microstructure are directly related to these interactions. Dynamics of the melt pool are best demonstrated by first considering CW welding and then comparing these results to a pulse regime.

Basov demonstrated that the behaviour of the vapour-plasma jet in continuous welding is unstable³³. The vapour-plasma phase is removed from the keyhole in a periodic manner at a frequency of several hundred hertz. Thus, transfer of the melt from front to rear of the keyhole is intermittent.

Pulsations detected in welding with a continuous laser beam are explained from a physical point of view by the following considerations. Once a keyhole is formed, the metal at the front of the keyhole is heated from its melting point (T_m) to its boiling point (T_b). During keyhole welding, the primary driving force is the reactive pressure of the vapour phase. Vapour pressure transfers the molten metal from the front of the keyhole towards the rear where it mixes and solidifies. Transfer of the melt is extremely rapid, approaching 1 meter per second, at high welding rates. Since the majority of the melt is removed rapidly, temperature at the front of the keyhole, from which the melt was removed, is approximately T_m . It follows that this surface must be heated to T_b to continue

the melting and transfer of melt during a continuous weld. Therefore, laser welding in the continuous regime can be considered a periodic process.

The intermittent nature of continuous welding processes has also been attributed to blockage caused by the plasma phase formed at the material surface. This problem has been controlled to some extent through introduction of plasma suppression gases such as helium. Results have shown that gas suppression must be applied at high pressures to be effective. Such pressures can cause detrimental mechanical effects upon the melt pool, thereby reducing the overall quality of the resulting weld. One efficient method of preventing the development of the plasma jet is periodic interruption of the laser radiation.

1.4.2 Pulsed Welding

During pulse-periodic laser welding at least five parameters act independently on the substrate: mean power, peak power, pulse duration, pulse frequency, and pulse shape. With this in mind, it can be assumed that the pulse periodic regime has four or more degrees of freedom than continuous operation in which only average power is regulated. All these factors have a significant effect on the formation, maintenance and re-solidification of the melt pool.

It is well known that carbon steel laser welding processes are hampered by high initial reflectivity of the metallic substrate to 10.6 μm radiation. As mentioned, reflection continues until sufficient energy is absorbed to raise the material temperature to a more efficient energy absorption point. As such, higher peak power in the incident beam results in a more rapid absorption of energy, as compared to steady state application of power. Rapid

absorption and subsequent vaporization of the substrate is a characteristic of all “giant-pulse” laser processes. In most lasers, these processes are limited to ablating or scribing the material surface, due to lack of energy in the pulse. Such systems are incapable of deep penetration welding, since they are unable to form and maintain a stable keyhole.

During pulse-periodic irradiation, behaviour of the melt both during the pulse and in the inter-pulse period differs markedly. Drobyazko investigated movement of the melt under the effect of averaged forces during the pulse repetition time and periods between pulses³⁴. High speed photography allowed observation of molten material dynamics during the entire sequence of pulse application.

Under the action of a pulse, the melt pool acts in a manner similar to that described for continuous wave welding. Figure 1.7 depicts that the front wall of the keyhole is inclined in the direction of processing. Flow of the melt is horizontal to the substrate surface, flowing to the back of the keyhole where it mixes and solidifies.

During the period between pulses, melt dynamics change drastically. After a slight delay, the melt moves rapidly from the rear wall of the keyhole to the front, decreasing in speed as re-solidification takes place. Drobyazko observed that in the initial period after the pulse, the front wall of the keyhole solidified at a higher rate than the rear wall. The reverse movement of the melt started after maximum temperature was reached at the rear wall of the keyhole. These results were attributed to capillary forces, which caused reverse movement of the liquid metal after the pulse³⁴.

Efficient energy coupling to the substrate is of primary importance when deep pen-

etration is desired. As discussed earlier, the problem of surface plasma beam absorption is significantly reduced in the pulse periodic regime. At carefully chosen repetition rates, the plasma will recombine prior to onset of the next pulse. A certain finite time is also required for formation of the plasma jet. Therefore, for a significant portion of the laser pulse, the beam is not subjected to any plasma interference. Consequently, plasma suppression gas requirements are reduced, thereby effecting a significant cost savings.

From the above discussions, it can easily be inferred that higher peak power (P_p) in the incident beam leads to more rapid keyhole formation, for a given focal spot size. This aspect conveys the benefits derived through the burst excitation technique, which constitutes the essence of this thesis.

Burst excitation enhanced welding is unique in comparison to existing laser processes. Current literature on high power pulsed laser welding stresses two main areas; high repetition rate application of high peak power, low average power pulse trains^{24,27,28} and gated operation of CW laser systems^{35,36}. These concepts are not easily applied to deep penetration welding, due to a lack of average power. As discussed previously, maintaining an economical welding rate in heavy metal sections necessitates formation of a keyhole in the material. Critical factors in establishing and maintaining such a keyhole are peak intensity and average power. Burst operation of the PIE system considered here produces variable duty cycle, pulse periodic output with high peak power at multi-kilowatt average power levels.

Technological excitation limitations in existing high power lasers restrict the range of temporal optical outputs. Burst excitation provides a means to create a wide variety of

optical output pulse shapes. It has been suggested that in under certain pulse conditions weld solidification may ensue prior to completion of a laser pulse. Under these conditions, it may be possible to control the weld properties through manipulation of the temporal profile of the laser pulse^{37,38,39}.

Chapter 2

System Components and Development

Investigation of this burst excitation optical pulsing process required design, development and modification of a broad range of new and existing equipment. Central to this study was a 30 kW, fourth generation, prototype of the PIE geometry laser, PIE IV. In order to maintain this relatively complex device, a number of key peripheral sub-systems were necessary. Power supplies, driver circuits, beam delivery equipment, optical attenuation systems, current and optical sensing, data acquisition and data processing apparatus were all essential elements in successful laser operation.

A complex laser system with output powers of this magnitude presented a number of safety issues. Since the purpose of this work was to develop a pulsing technique for deep penetration welding, average laser powers on the order of many kilowatts were desired. Sampling and manipulation of multi-kilowatt laser beams necessitated careful attention to apparatus damage thresholds and operator safety. During the course of this work, a variety of systems were developed to address these issues.

Figure 2.1 is a block diagram, presented to simplify the apparatus and sub-systems involved in this study. Primary areas of importance are presented in each block. This chapter thus serves to expand details contained within each of the blocks presented in Figure 2.1.

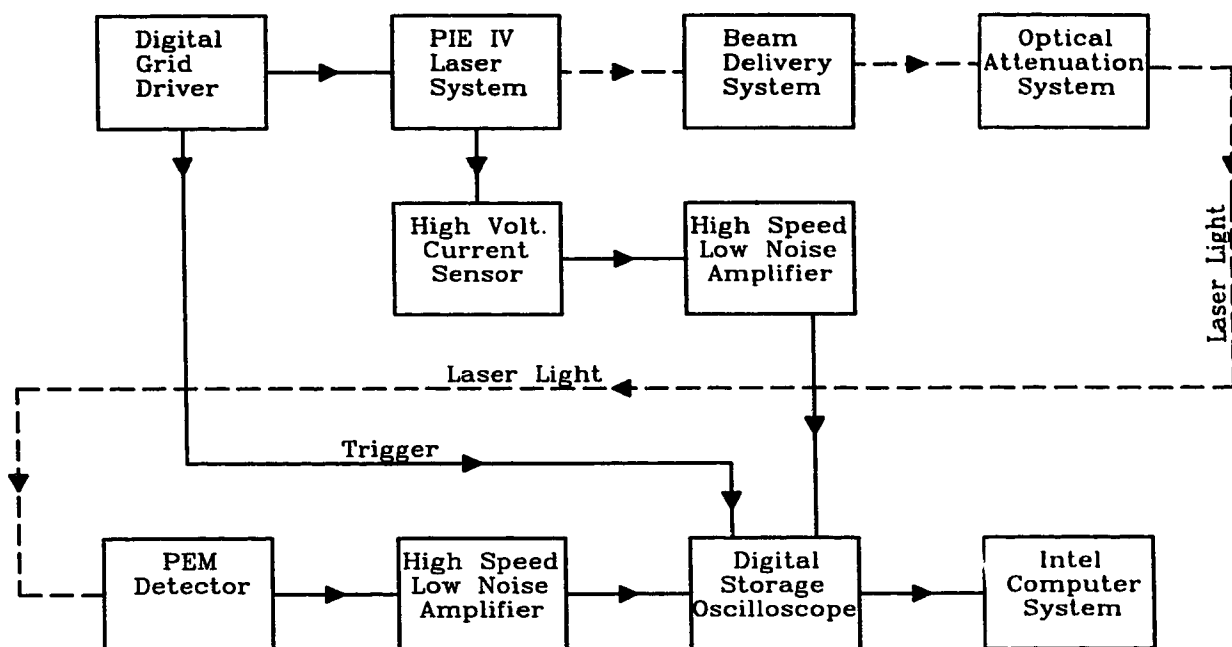


Figure 2.1: Simplified block diagram of the systems involved in this study.

2.1 Laser System Overview

Development of the PIE process is covered extensively elsewhere^{13,14} and consequently will only be summarized here. The PIE IV laser system is comprised of a 20,000 liter vacuum chamber which contains fluid-ballasted, multi-element electrodes⁴⁰, axial flow compressors, heat exchangers and a folded optical extraction system,⁴¹ all shown schematically in Figure 2.2. This figure also illustrates the basic principles of this transverse-flow system. Gas leaving the discharge region is split into two separate streams, each passing through a chilled water heat exchanger. After leaving the heat exchangers, the gas streams converge at the entrance to high-speed blowers. From here, the lasant mixture passes through a flow transition unit and then on to the discharge region as a uniformly collimated stream.

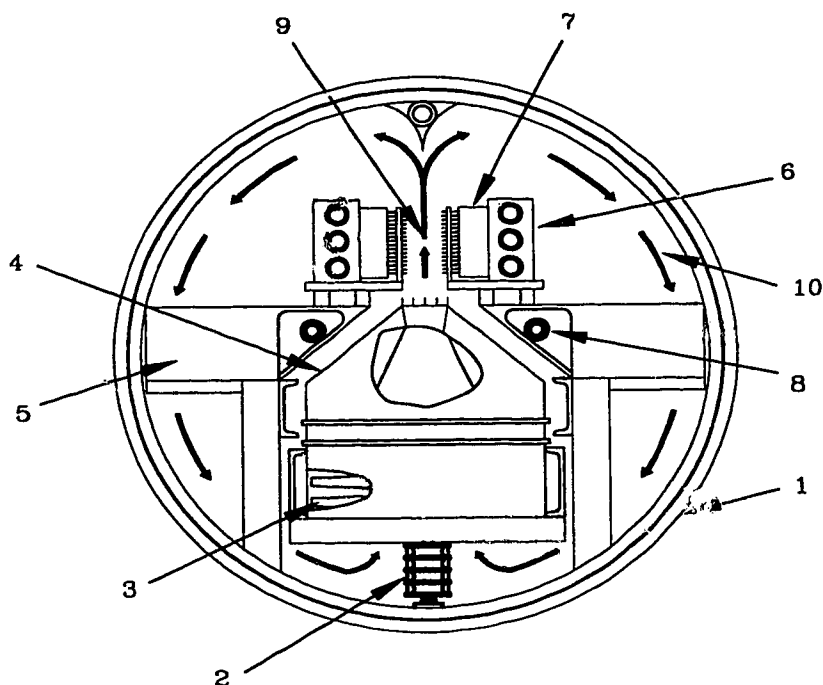


Figure 2.2: PIE IV simplified mechanical schematic; (1) vacuum enclosure, (2) blower drive, (3) blower blades, (4) flow transition unit, (5) heat exchangers, (6) ballast delivery system, (7) multi-element electrode blocks, (8) vibration isolation optical bench, (9) discharge region.

All controls are mounted at either end of the chamber, with motors and pumps mounted underneath. Ionization and DC pumping power supplies are located external to the vacuum enclosure with energy being delivered through high-voltage, shielded, coaxial cables. The laser also features real-time beam mode and power control sub-systems^{42,43}. A photograph of the overall laser is provided in Figure A.1 of the Appendix. The area of greatest interest in this research is the electrical excitation systems.

The PIE process is characterized by high frequency application of dual polarity 10 kV photoionization impulses coupled with high voltage DC excitation to produce a highly stable, large volume discharge. Production of photoionization impulses is

accomplished utilizing a digitally controlled hydrogen thyatron circuit. Previous investigations of pulse-periodic operation of a PIE system were performed on a 10 kW predecessor, PIE III^{16,17,18}. These results were concerned primarily with discharge effects during pulsed operation. Results presented here reflect investigations on PIE IV, a more recent 30 kW CW version, and are particularly focused on optical power extraction and materials processing sequences.

2.2 Discharge Systems

The PIE process involves the generation of a continuous gaseous gain media by means of controlled and sequential application of a series of photo-ionization and avalanching electrical impulses. At present, the pulser is designed to deliver such conditions at a repetition rate of 5 kHz. Despite the fact that the ionization process is pulsed, the resulting laser plasma can be operated in a continuous mode. This aspect follows from the fact that the pulser period is significantly shorter than the plasma relaxation time. Optimization studies on a similar system have shown that the sequential process of photo and impulse ionization is extremely fast. Therefore, only minimal duration impulses are required¹³.

A circuit diagram of the excitation apparatus used in this laser is presented in Figure 2.3. A pentode hydrogen thyatron, interfaced to a digital pulse generator, is the primary switching element. Oil immersion serves to both cool and insulate the thyatron and other high voltage components. Operation can be understood as follows. Assuming capacitors C1 and C2 are fully charged, a pulse event from the digital pulse generator triggers the thyatron, through the grid driver circuits. The thyatron switches to full

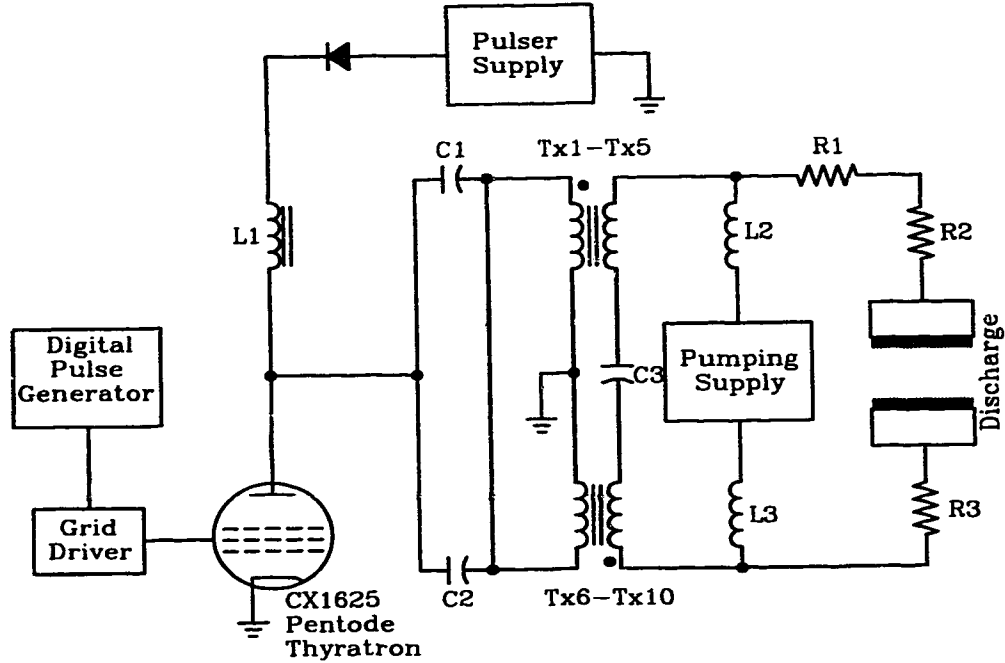


Figure 2.3: PIE IV simplified discharge system schematic. Component values given in Table 2.1.

conduction very rapidly, thereby discharging C1 and C2. As these capacitors discharge, current flows through the primaries of pulse transformers⁴⁴ Tx1 through Tx10. Opposite polarity pulses are extracted from these pulse transformer networks and are subsequently combined with DC excitation. Ionization impulses are characterized by a full width at half maximum (FWHM) duration of approximately 80 ns. Isolation of impulse and DC circuits is provided by inductors L2 and L3. Table 2.1 provides a summary of the component values in Figure 2.3. These combined ionizational and vibrational excitation processes are imposed upon the discharge region through a multi-element, fluid ballasted electrode pair. Ballast resistance is on the order of 10 Ω . A photograph of the pulser thyatron box is included in the Appendix as Figure A.3.

To complete the cycle, the thyatron shuts off as a result of the saturation of L1,

Component	Description	Value
L1	Saturable inductor	-
C1,C2	Low inductance capacitors	8 nF
C3	Blocking capacitor	1 μ F
Tx1-Tx5 Tx6-Tx10	Distributed core pulse transformers	1:3
L2,L3	Isolation inductors	83 mH
R1	Precision resistor 25 mV @ 50 Amps	-
R2,R3	Ballast Resistance	\sim 10 Ω
Pulser Supply	Provides ionization voltage	24 kVA 6 kV Variable
Pumping Supply	Provides upper laser level pumping	340 kVA +/- 3.5 kV Variable

Table 2.1: PIE IV laser system simplified discharge schematic component values, Figure 2.3

subsequent to the discharge of C1 and C2. Once the thyatron is no longer conducting, C1 and C2 are recharged through the resonant charging circuit of L1 and C1 and C2.

Both ionization and pulser DC power supplies are 3 phase primary, diode rectified, SCR controlled, variable sources. Each consists of filter networks designed to minimize the presence of pulser noise throughout the system. Final output of the DC pumping supply consists of 700 μ F filter capacitors followed by 10 mH arc prevention inductors. These inductors, combined with 83 μ H isolation inductors L2 and L3, strongly influence current waveform characteristics.

2.2.1 Grid Driver

CW operation of this laser is characterized by the digital pulse stream represented by Figure 2.4(A). Pulsed operation is accomplished through manipulation of the digital

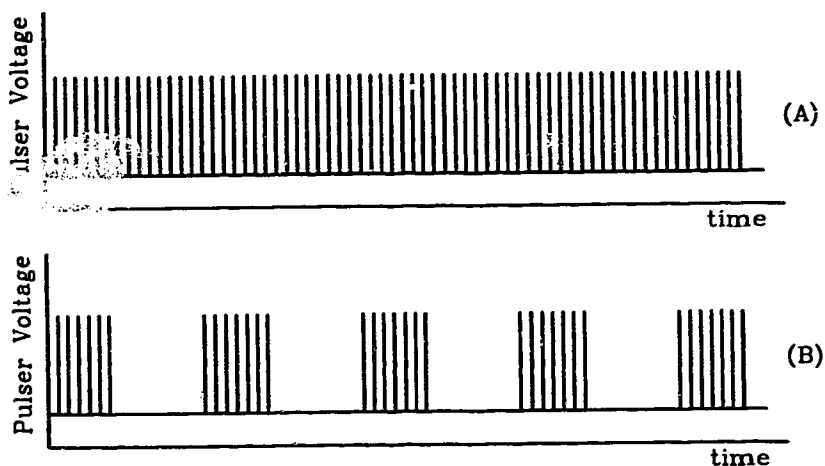


Figure 2.4: Grid driver output pulse stream; (A) CW excitation, (B) Burst excitation with $N=7$.

drive signal. In its simplest form, pulsing is achieved by simply gating the CW drive as represented by Figure 2.4(B). This waveform is characterized by a grouping of individual impulses, defined here as a burst and an envelope of bursts, defined as the burst frequency (f_b). Frequency and duration of optical output pulses are proportional to the burst frequency. For the purpose of these experiments, pulse frequency was held constant at 5 kHz with a 1% duty cycle. Incorporation of a digital drive oscillator permitted manipulation of the number of impulses per burst (N) and the overall burst frequency.

A simplified block diagram of the digital grid driver system developed specifically for this application is presented in Figure 2.5. Component details are given in Table 2.2.

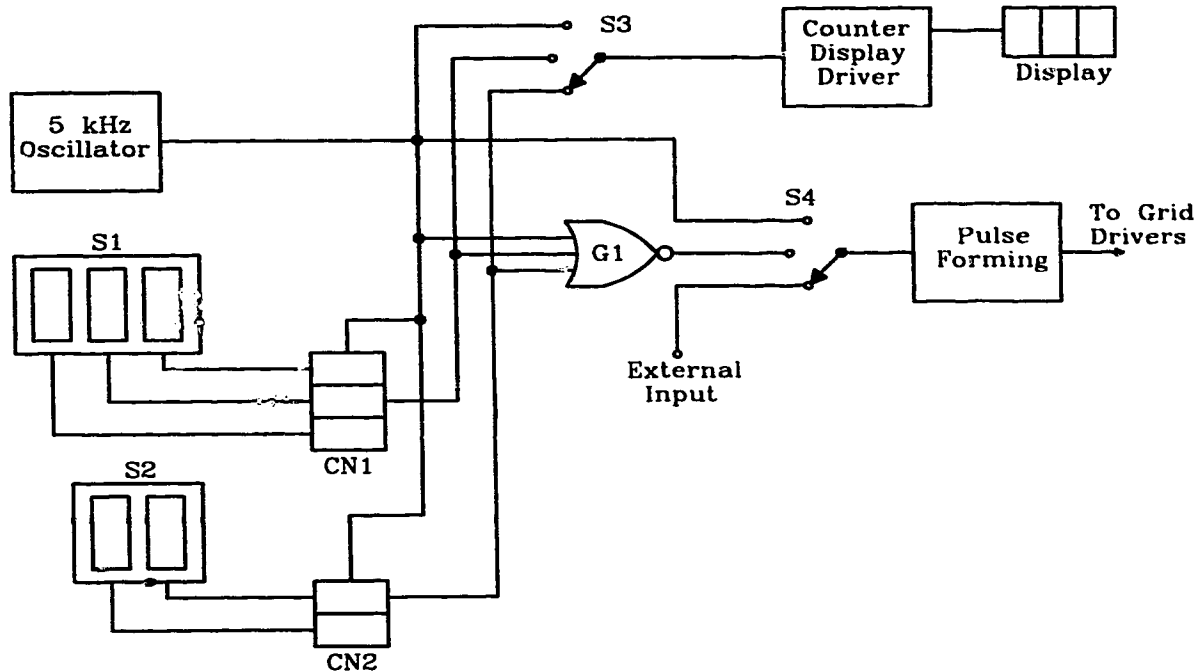


Figure 2.5: Simplified Block diagram on digital grid oscillator/grid driver circuit. Component details are supplied in Table 2.2

Component	Description	Value
S1	Thumbwheel switches	f_b
S2		N
S3	Rotary switches	clock
		f_b
		N
S4		CW int. burst ext. burst
CN1,CN2	Counters	
G1	4025 logic gate	

Table 2.2: Grid driver block diagram components found in Figure 2.5

Here, the primary element is a 5 kHz oscillator. Driver operation is enabled through

manipulation of switch S4. CW operation is achieved by connecting a 5 kHz clock signal directly to the grid drivers through S4. In the middle position, S4 connects the internally generated burst signal to the grid drivers. Control of burst parameters f_b and N is achieved through manipulation of thumbwheel switches S1 and S2. Burst frequency is set with switch S1, where the 5 kHz clock is divided by the decimal thumbwheel setting. For example, a thumbwheel setting of 100 results in a f_b of 50 Hz. N is controlled by the setting of switch S2. Counters, CN1 and CN2 convert numerical thumbwheel input to signals proportional to the thumbwheel settings. CN1 produces a pulse stream which represents the overall envelope of the burst frequency, while CN2 generates a signal representing the “on-time” or number of pulses. Clock and counter signals are superimposed by logic gate G1 and transmitted through S4 to grid driver circuits. Thus, the combination of the counter signals results in a gating of the 5 kHz clock to produce the required waveform. S3 toggles the seven segment display to indicate either clock frequency, burst frequency or number of pulses.

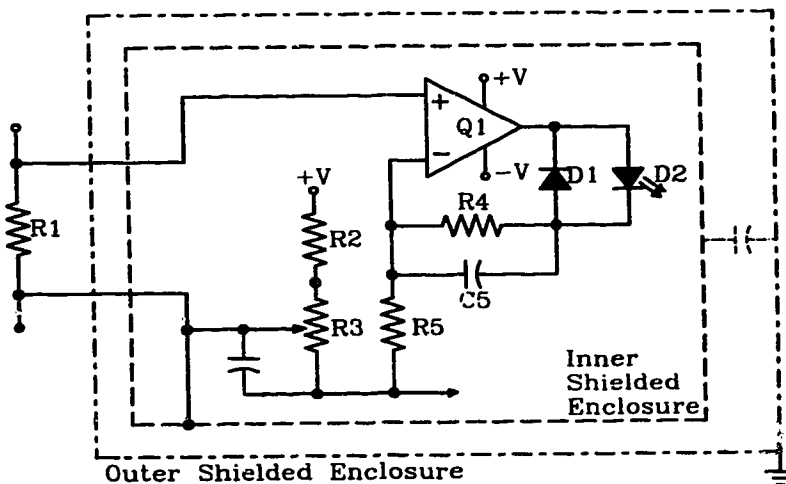
2.2.2 DC Supply Current Monitoring

Current monitoring for high-current, high-voltage applications is possible in a number of forms, including, in-line resistors, shunts, magnetic pickups and inductive coils. This application required monitoring current levels as high as 100A, at constant DC voltage levels up to 3.5 kV. Under burst excitation conditions, at the power levels in this study, current levels did not exceed 50A. Based on the extremely broad range of frequencies found in the current waveforms, both magnetic pickup and inductive coil measuring devices were impractical. For reasons of simplicity and accuracy, a single high-

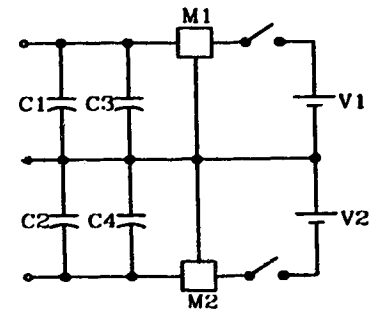
precision in-line resistor was chosen as the sampling device. Current waveforms were obtained by observing the voltage impressed across this 1 m Ω precision resistor, when inserted in series with the discharge circuit, shown in Figures 2.3 and 2.6(A), as R1.

With this configuration, resistor potential floated up to 3.5 kV under normal laser operating conditions. This, coupled with a low signal output of 25 mV at 50A, required the development of a high-gain, low-noise amplifier. The OP37 operational amplifier well suited the broad band frequency spectrum associated with these waveforms. As a further requirement, the data acquisition system required that the signal be isolated from the high voltage level. An optically isolated sampling and transmission system was therefore developed to accomplish this task.

Figures 2.6(A) and (B) are schematics for the current transmitter and regulated



(A)



(B)

Figure 2.6: DC pumping supply current monitoring apparatus; (A) High voltage current monitor and transmitter, (B) Regulated Battery DC supply. Component values are given in Table 2.3

battery supply, respectively. A summary of the components used in this figure are presented in Table 2.3. The transmitter circuit consists of a high-speed, ultra-low-noise

Component	Description	Value
E1, E2	batteries	9 V
C1, C2	line filters	100 μ F
C3, C4	regulator filters	0.1 nF
C5	stabilization capacitor	1.5 nF
D1	reverse spike protection diode high speed switching	1N4148
D2	Red LED emitter	MFOE76
Q1	high speed ultra-low noise op-amp	OP 37
M1	voltage regulators	78L05 (+5V)
M2		79L05 (- 5V)
R1	Precision Resistor	25 mV @ 50 A
R2	set point (I_f bias) resistors	3.9 k Ω
R3		0.5 k Ω potentiometer
R4	feedback and protection resistor	39 Ω
R5	transconductance resistor	820 k Ω
+V	battery supply	+9 V
-V		-9 V

Table 2.3: Transmitter circuit and power supply elements in Figure 2.6.

OP37 amplifier, a precision resistor and a MFOE76 photodiode. Here, R2 and R3 establish a 5 mA bias current in the photodiode. With a maximum signal of 2 mA, operation occurs within the MFOE76's linear region of 5 to 7 mA. Voltage differentials across the precision resistor are then converted to light signals via the photodiode. The inner hatched box in Figure 2.6(A) represents a copper shielded enclosure which floats at

the potential of the precision resistor. For safety and shielding considerations, this box is isolated and enclosed within a larger grounded box. A small displacement current exists between the inner and outer boxes as a result of the structure capacitance. Light signals are transported from the circuit within the inner box through a 1000 micron core, plastic, fibre optic link to the isolated receiver circuit. A regulated battery supply shown in Figure 2.6(B) is housed within the high voltage copper enclosure for ease of shielding and high voltage isolation. Thus, the fibre optic cable provides the necessary voltage isolation between transmitter and receiver.

Figure 2.7 illustrates the receiver circuit with component values summarized in

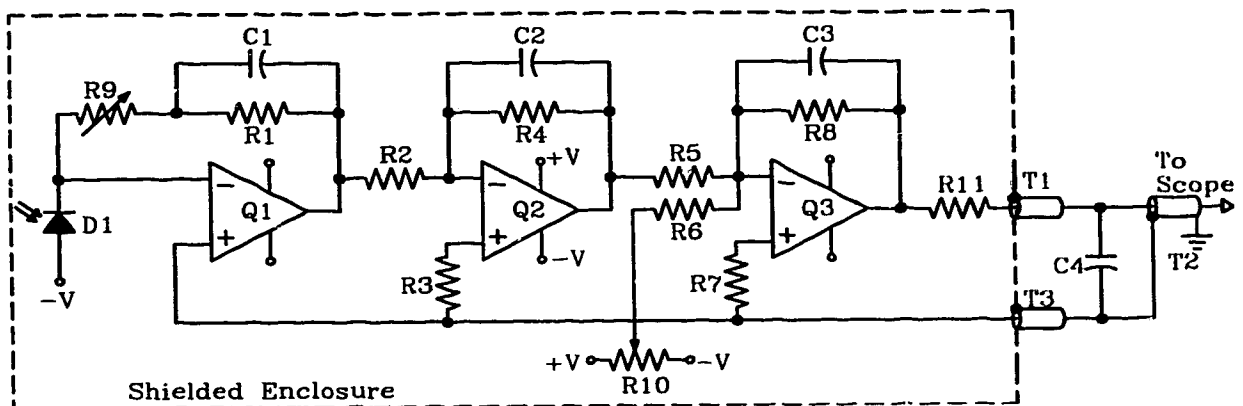


Figure 2.7: High voltage current receiver. Component values given in Table 2.4

Table 2.4. Light incident on the diode, from the fibre link, produces a proportional current at the non-inverting input of Q1. Amplification of the signal is accomplished through 3 cascaded stages. Noise in the circuit is minimized through shielding and single point grounding achieved by connecting the circuit common and earth ground at the

Component	Description	Value
D1	PIN diode	MFOD71
C1, C2	stabilization capacitor	22 pF
C3		3.3 pF
C4	filter	8 pF
Q1, Q2, Q3	op-amp: ultra-low noise, high gain	OP 37
R1, R4	feedback resistors	5.6 k Ω
R8		51 k Ω
R2	input resistors	820 k Ω
R5		8.2 k Ω
R3	offset compensation	680 Ω
R7	offset compensation	6.8 k Ω
R9	gain adjustment	10 k Ω pot
R11	noise reduction/matching	51 Ω
R6	offset correction	39 k Ω
R10	offset correction	10 k Ω pot
T1, T2, T3	coax cable	-
+V	battery supply	+9 V
-V		-9 V

Table 2.4: Receiver circuit components as illustrated in Figure 2.7.

oscilloscope only.

The receiver amplifier was tested against original design constraints as listed above. Figure 2.8 illustrates overall voltage gain with respect to frequency. Here, the 3dB point is found to be approximately 700 MHz. Figure 2.9 represents the phase performance of the amplifier over the frequency range in question.

Signal bandwidth was estimated as DC to 1 MHz. Spectral energy density analysis⁴⁵ was performed over the range of 4 kW current samples illustrated in Figures 3.5

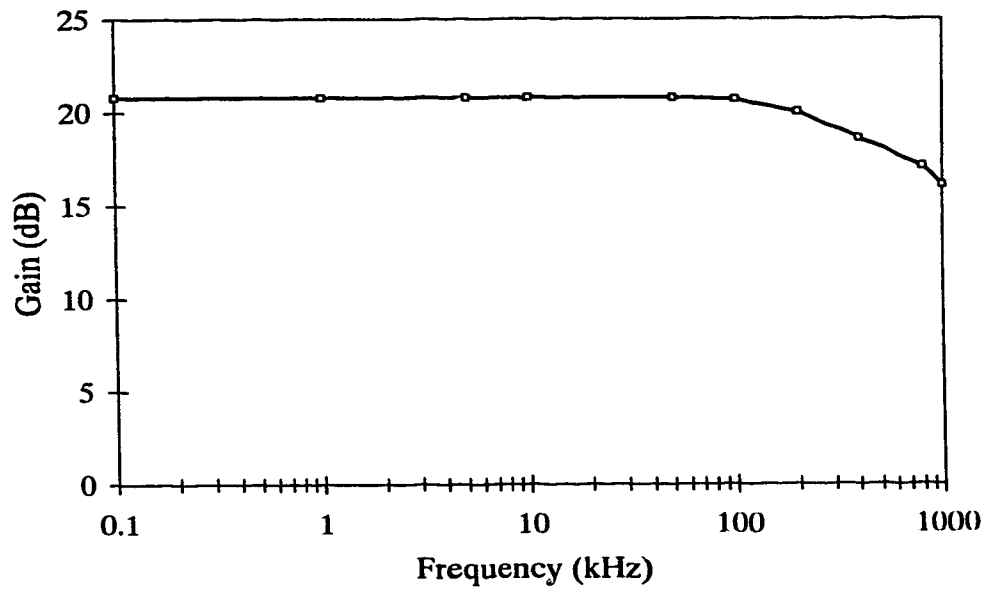


Figure 2.8: Current monitor receiver amplifier gain with respect to operating frequency.

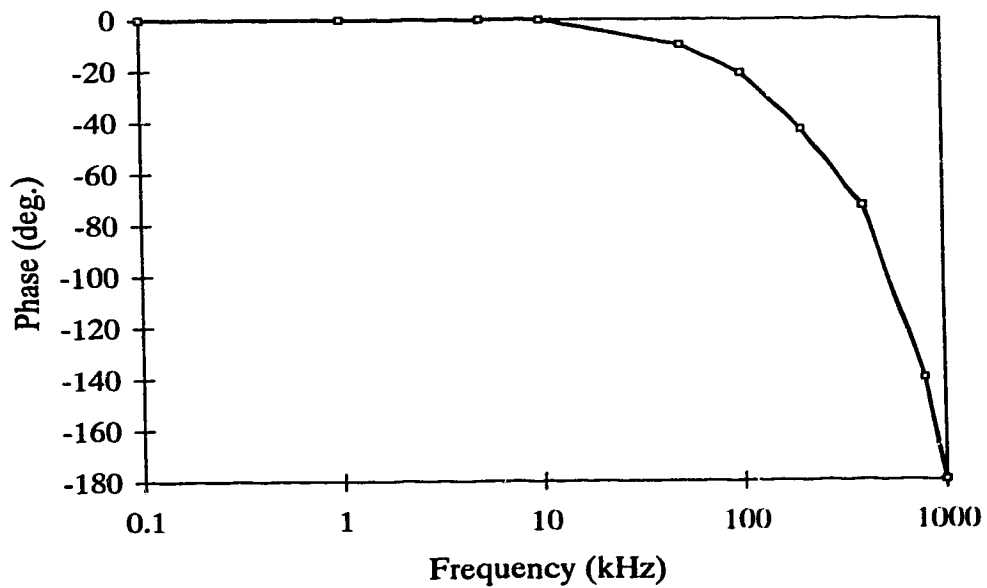


Figure 2.9: Current monitor receiver amplifier phase with respect to operating frequency.

through 3.9 and also at 2 and 6 kW. Figure 2.10 presents spectral energy density,

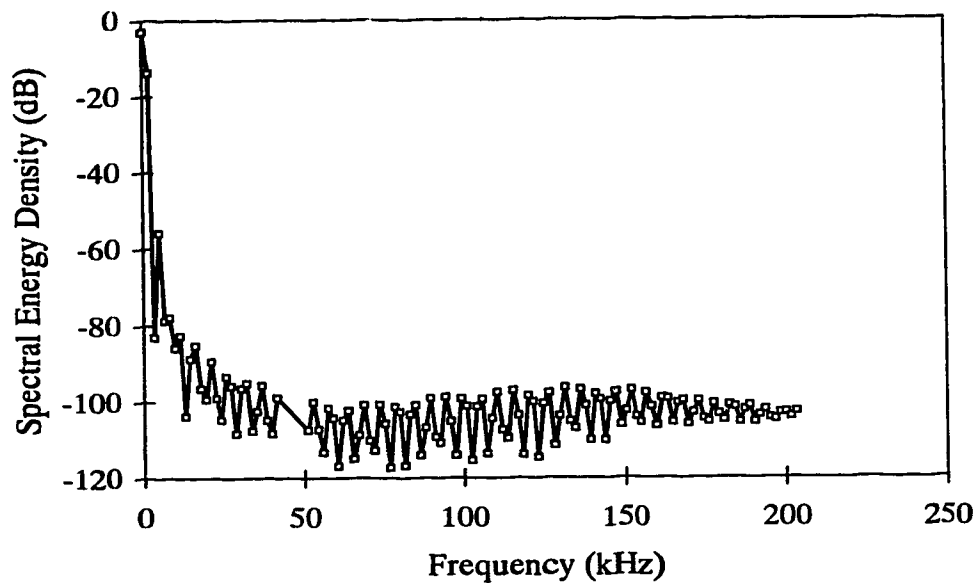


Figure 2.10: Spectral energy density for a typical current waveform. Significant harmonic content is contained below 20 kHz. Harmonic effect of 5 kHz pulser repetition is also evident. Current waveform: $P_{av}=4\text{kW}$, $f_b=200\text{ Hz}$ and $N=3$.

normalized with respect to the total power in the signal, of a typical current signal. Here, the spectral energy density is found to drop about 90 dB in the first 20 kHz. Thus, the significant portion of the spectral energy density is contained well within the linear operating region of the amplifier, as illustrated in Figures 2.8 and 2.9. Based on this observation, the original bandwidth assumption was conservative and thereby yielded a high degree of confidence in the amplifier output.

2.3 Optical Beam Handling Systems

Transport of the multi-kilowatt laser beams, inherent in this investigation, required use of highly reflective, robust, water cooled optical components. Further, it was necessary to contain the beam within adequate enclosures to ensure safety. In order to facilitate the complex optical monitoring systems utilized in this study, it was necessary to transport the beam from the laser device to a self contained optical bench.

Despite relative insensitivity of the detector used, it was still necessary to attenuate the optical laser output by 6 orders of magnitude. Attenuation was achieved with a combination of reflecting and transmissive optics.

2.3.1 Beam Delivery System

Figure 2.11 is a schematic representation of the beam delivery system used to

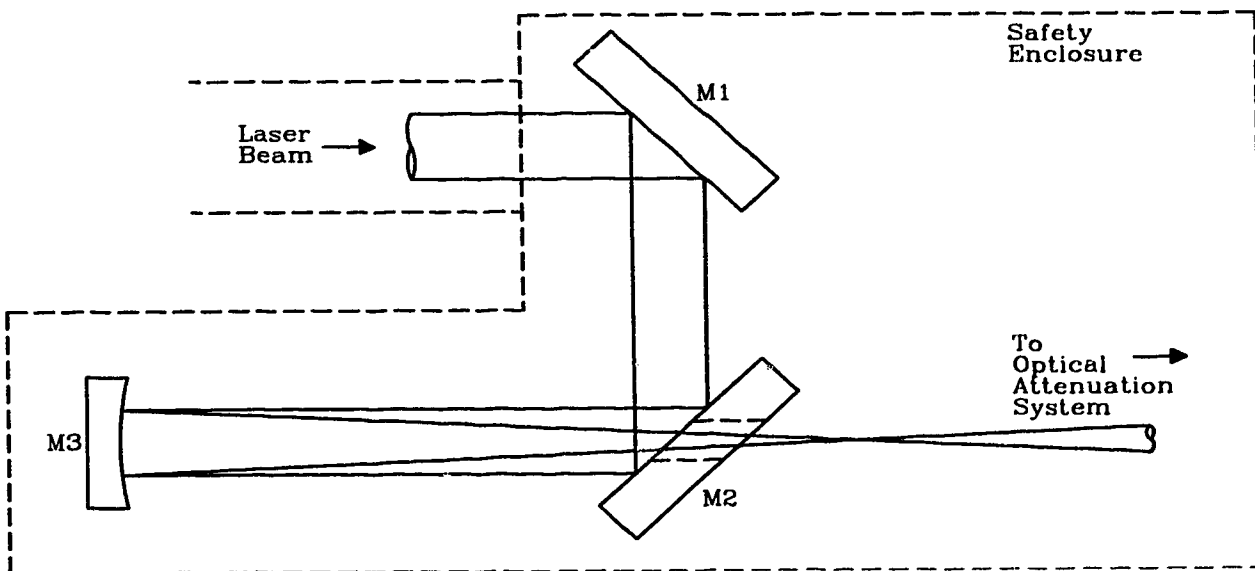


Figure 2.11: Optical beam delivery system.

transport the laser beam to the optical bench. The beam was conducted, in a tubular steel enclosure, approximately 2 meters from the laser to the first optic in Figure 2.11. An optical bench approximately 3 meters in length by 0.5 meters deep, was constructed from heavy steel sections for maximum stability. A 10 mm thick plexiglass screen enclosed the entire bench, to facilitate observation of the optical systems while providing protection from scattered radiation. Space limitations required use of a skimner and focusing mirror configuration, commonly found in laser welding heads. Translation of the beam from a perpendicular to horizontal orientation with respect to the bench surface was achieved with this apparatus. Once in the horizontal orientation, the laser beam propagated into the optical attenuation system as discussed in the following section. Figure A.5 presents a photograph of the beam delivery system and safety enclosure described above.

2.3.2 Optical Attenuation System

As mentioned, it was necessary to attenuate the optical output by 6 orders of magnitude for detector safety. Burst optical pulses are characterized by a broad spectrum of frequencies. For this reason, rotational sampling of the beam would lead to an unacceptable loss of detail. Therefore, a real-time optical sampling system was developed. Primary attenuation was achieved with an anti-reflection coated, ZnSe, window oriented as a beam splitter. Subsequent attenuation was accomplished with an adjustable ZnSe attenuator and various partially reflecting ZnSe optics. Finally, the attenuated beam was focused upon a PEM detector using a ZnSe lens, Figure 2.12. A summary of the optics and devices in this figure is presented in Table 2.5.

Beam diameter at MR1 was approximately 8 cm, as illustrated by a typical burn

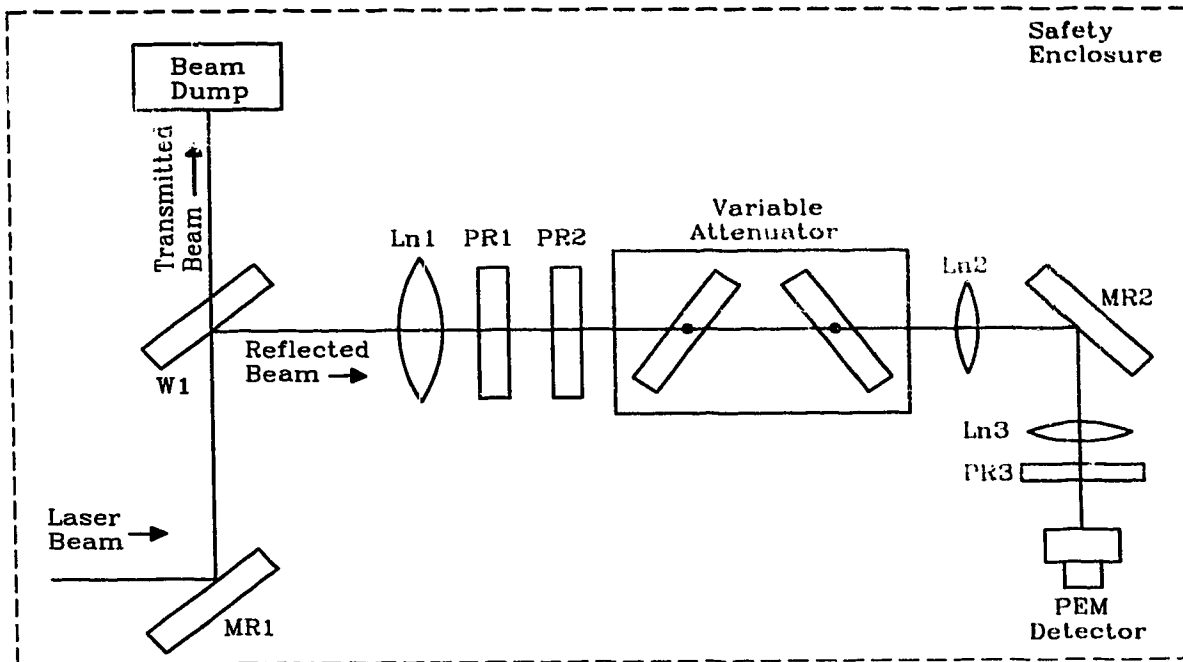


Figure 2.12: Optical attenuation system.

Component	Description
MR1 MR2	Flat mirrors
W1	12.7 cm diameter, 1.3 cm thick, AR coated ZnSe window
Ln1	10 cm diameter, $f = 30$ cm, ZnSe lens
Ln2	5 cm diameter, $f = 3.5$ cm, germanium lens.
Ln3	5 cm diameter, $f = 6.3$ cm, ZnSe lens
PR1	7.6 cm diameter, 15%, ZnSe partial reflector
PR2	7.6 cm diameter, 30%, ZnSe partial reflector
PR3	2.5 cm diameter, 90%, ZnSe partial reflector

Table 2.5: Optical attenuation system components as shown in Figure 2.12.

pattern in Figure A.4. Real time beam sampling was accomplished by orienting W1 at 45° to the incident beam axis. Multi-kilowatt power levels necessitated water cooling of W1.

In this orientation, approximately 5% of the incident beam was reflected to Ln1, with the remaining portion dissipated in an air cooled beam dump. At only 5% attenuation, additional partial reflectors, PR1 through PR3, were necessary to ensure that detector operating parameters were not exceeded. Beam focusing with lenses Ln1 through Ln3 was necessary for application to the 1 mm² detector surface. A variable attenuator was constructed consisting of two 1.3 cm thick ZnSe uncoated blanks mounted on a gear driven mechanical assembly. Mutual rotation of the blanks resulted in variable attenuation. With a fixed detector damage threshold of 100 W/cm², adjustment of the attenuation level was necessary at each average laser power explored in this study.

With the average laser power level sufficiently reduced to prevent detector damage or saturation, real-time monitoring of the laser output was possible. The following section describes the techniques developed for monitoring and recording optical data. A photograph of this apparatus is presented in Figure A.6.

2.4 Optical Monitoring

Multi-kilowatt CO₂ laser beam analysis is hampered by the high average power incident on detection devices. Pulsed lasers with sufficiently small duty cycles pose less of a problem in terms of average power, but peak powers can also lead to detector saturation and damage. While many IR detectors are available at 10.6 μm, pyroelectric detectors are the primary choice when high frequency, high peak power radiation is of interest⁴⁶.

For the burst application in this study, it is of interest to resolve the CW, low frequency and high frequency transient content of the optical pulses. As such, a DC to 1

MHz or higher frequency response is required in the detector. While pyroelectric detectors have excellent high frequency response, they saturate easily in low frequency applications. Photovoltaic detectors are more commonly used in such situations. The Mercury Cadmium Telluride (MCT) detector is the most common type of photovoltaic detector for such applications. MCT detectors are available in cryogenically cooled, thermoelectrically cooled and room temperature (T_a) models. In general, the detectivity increases with decreasing operating temperature. For this application, a T_a MCT detector was chosen for its frequency response and relative insensitivity to high incident laser power⁴⁷.

2.4.1 PEM Detector

A Vigo Sensor PEM-L-2 photo-electromagnetic (PEM) MCT detector⁴⁸, had ideal characteristics for this application. In the PEM effect, infra-red photons are absorbed at the surface of a semiconductor producing free electron-hole pairs which diffuse from the surface into the bulk, Figure 2.13. An applied magnetic field separates these charge pairs as they diffuse inward. Charge separation results in an open circuit electrical potential being impressed across the semiconductor terminals. Under short circuit conditions, the PEM effect produces a current which is proportional to incident photon intensity. Thus, operation of PEM detectors is possible in both current and voltage modes.

Experiments in our laboratory have indicated that this type of detector suffers from a thermally induced signal offset. Indeed, thermally generated electron-hole pairs are indistinguishable from optically generated carriers. Therefore, when a significant continuous optical power results in elevated substrate temperature, thermal electron-hole

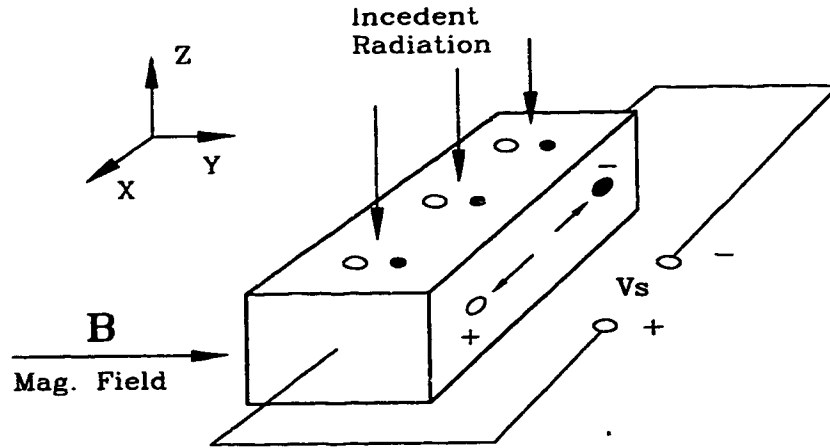


Figure 2.13: PEM detector schematic

creation results in an output signal offset. In testing this hypothesis, signal offset was observed in a number of average laser power trials. As expected, signal offset was proportional to average incident laser power.

Once the source of signal offset was identified, a simple offset correction routine was incorporated into the automatic data acquisition system discussed below. Given n data points d_i with known thermal offset P_{therm} the power P_i corresponding to each d_i is computed as in (2.1). Here, Λ is the data scaling factor and P_{therm} is the detector thermal offset power equivalent. P_{av} is the average laser power, measured independently with a spinning-cone calorimeter⁴⁹. This scaling method is independent of oscilloscope scale, thereby allowing for maximum scope resolution of the optical waveform.

$$P_i = \Lambda d_i - P_{\text{therm}} \quad (2.1)$$

where

$$\Lambda = \frac{(P_{av} - P_{therm})}{\frac{1}{n} \sum_n d_i} \quad (2.2)$$

P_{therm} is determined from a single low frequency case for which the optical output is known to decay to zero between bursts. The offset signal is taken as P_{therm} which can then be used to scale all data sets taken at the same average laser power.

2.4.2 Optical Detector High-speed Low-noise Amplifier

As discussed previously, the spectral content of the optical output from this system was expected to range from DC to approximately 1 MHz. Choice of the PEM detector required development of an amplifier which matched the detectors operational characteristics. With an average output signal on the order of 5 mV, the first requirement on the amplifier was high input impedance. Secondly, this small signal would require significant amplification for ease of data acquisition with a digital storage oscilloscope. Finally, the laboratory environment suffered from appreciable ambient radio frequency interference (RFI) as a result of the high frequency content in the ionization impulses. Thus, it was necessary to construct a high input impedance, high voltage gain, high speed, low noise amplifier. Again, an OP 37 amplifier was well suited to this task. A three stage cascaded amplifier was constructed as illustrated in Figure 2.14. Component values for this figure are summarized in Table 2.6.

The amplifier was tested against the original design constraints as summarized in the following figures. Figure 2.15 illustrates overall voltage gain with respect to frequency. Here, the 3dB point is found to be approximately 900 MHz; close to the design

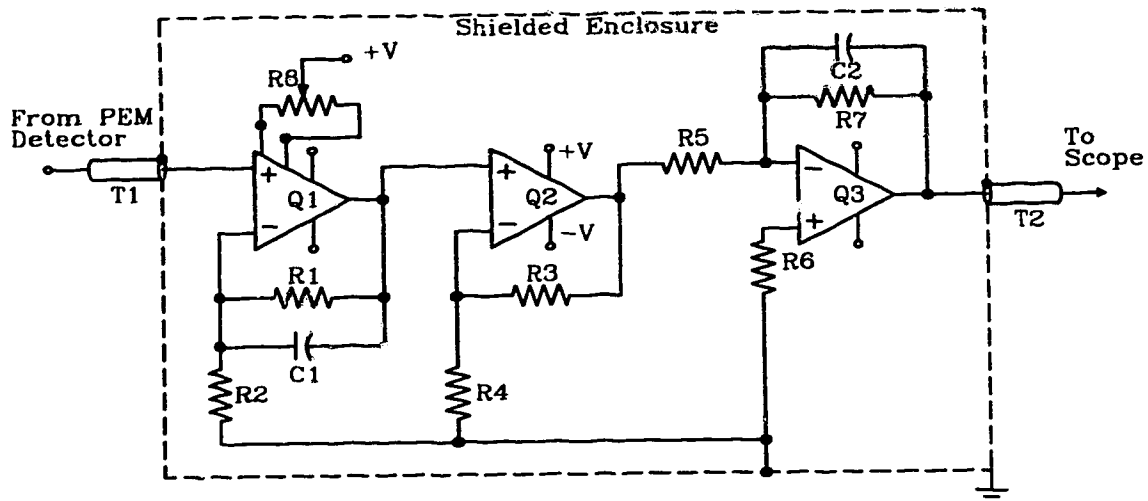


Figure 2.14: Optical detector high-speed, low-noise amplifier schematic.

Component	Description	Value
C1	stabilization capacitor	100 pF
C2		3.3 pF
Q1, Q2, Q3	op-amp: ultra-low noise high gain	OP 37
R1, R3	feedback resistors	2 k Ω
R7		20 k Ω
R2, R4	input resistors	270 Ω
R5		2.7 k Ω
R6		2.4 k Ω
R6	offset adjustment	40 k Ω
R7		10 k Ω pot
R8	offset adjustment	10 k Ω
+V	Battery supply	+9V
-V		-9V

Table 2.6: PEM detector amplifier circuit components as found in Figure 2.14

requirement. Figure 2.16 demonstrates the phase performance of the amplifier with respect to frequency.

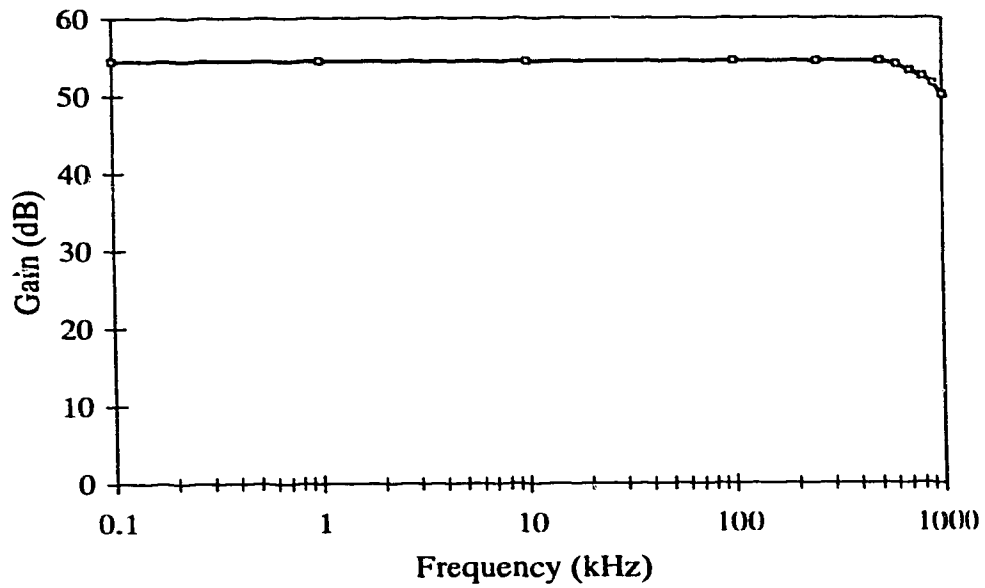


Figure 2.15: PEM detector amplifier gain with respect to operating frequency.

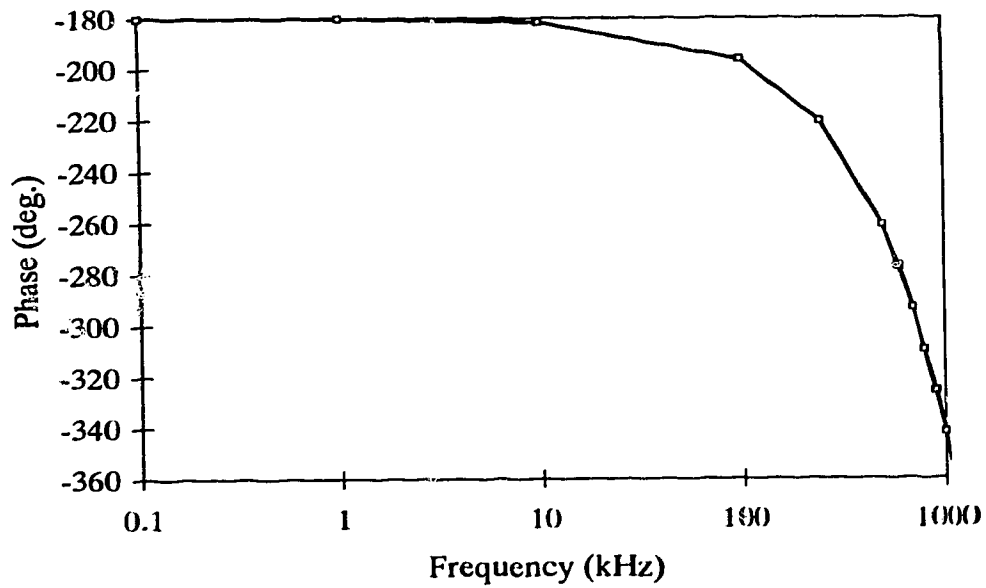


Figure 2.16: PEM detector amplifier phase with respect to operating frequency.

Figure 2.15 illustrates that the output from the amplifier is inverted through the last stage to accommodate the inverted signal emanating from the PEM detector. Isolation of the circuit was accomplished by construction of a self contained enclosure with internal batteries as power source. All external connections were implemented with shielded coaxial cable.

As discussed above, spectral energy density analysis was performed on the optical samples illustrated in Figures 3.5 through 3.9. Figure 2.17 shows spectral energy density,

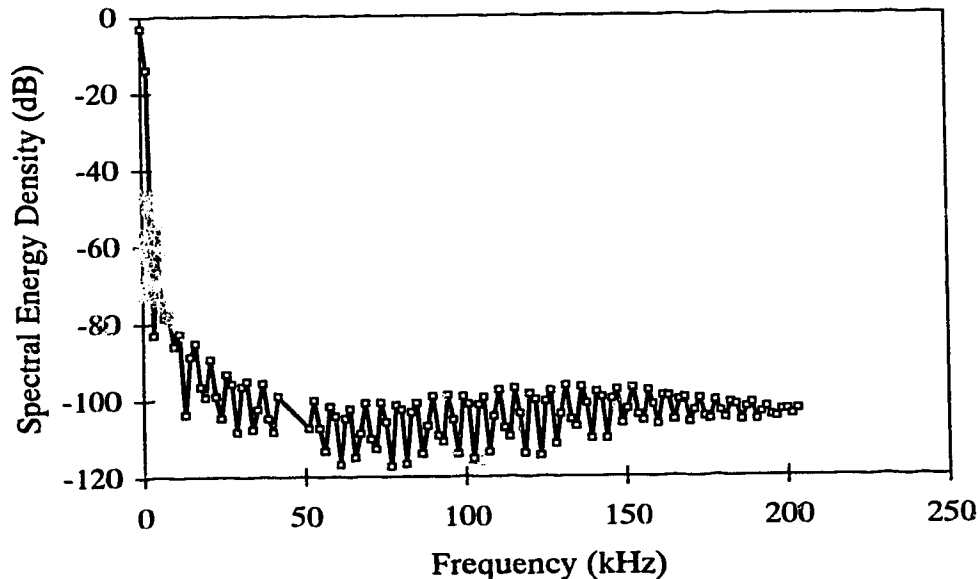


Figure 2.17: Spectral energy density for a typical optical waveform. Significant harmonic content is contained below 20 kHz. Harmonic effect of 5 kHz pulser repetition is also evident. Optical waveform: $P_{av}=4kW$, $f_b=200$ Hz and $N=3$.

normalized with respect to the total power, of a typical optical signal. Here, spectral energy density is found to drop about 100 dB in the first 20 kHz. A significant portion of

the spectral energy density is contained well within the linear operating region of the amplifier, as depicted in Figures 2.15 and 2.16. Once again, the original bandwidth assumption was conservative and thereby resulted in a high degree of confidence in the amplifier output results.

2.5 Data Acquisition and Processing

Primary interface between the output of both the optical and current amplifier circuits was a Phillips 3323 digital storage oscilloscope. Observation of various waveforms was made possible through the oscilloscope display. Permanent data recording was achieved with a data acquisition system interfaced with the oscilloscope. Over the course of this study, in excess of 400 current and optical waveforms were collected. Data volume required design of an automated data acquisition and processing system, to facilitate organization and comparison of the information.

Data transfer between the oscilloscope and an Intel based computer system was accomplished through an IEEE 488.8 standard bus interface. Automation was achieved through the development of a C programming language program to provide not only a man-machine-interface (MMI), but also control of collection and processing of data from the oscilloscope. Each waveform data set consisted of 4096 data points as well as scope timing, triggering, averaging and scale information. The system prompted the user for average laser power, burst frequency and N. An automated file naming convention, based on the month, day, hour, minute and second of data collection, was incorporated into the program. Each sample file name and other related data was subsequently logged to a file as a permanent record.

Based on user input and data collected from the oscilloscope, the program converted each plot to either current or laser power with respect to time. Data output was in the form of an ASCII text file. Generation of hard copy results from such a large data set also required automation.

Re-processing of this data in a reasonable time frame required computer processing power in excess of that available on the Intel system. For this reason, a Hewlett Packard 735 UNIX File Server was utilized for this task. Data manipulation routines were developed using the awk and sed scripting utilities within the UNIX operating system environment. Post-processing in UNIX included calculation of the PEM detector offset, discussed in Section 2.4.1 and generation of postscript files through the public domain software gnuplot.

This system allowed data processing to be performed quickly and consistently once the original files had been collected. In the end, amplifier output underwent unit conversion, scaling and offset correction before being output as a printed postscript document. In total, approximately 3000 lines of C code and 400 lines of awk and sed scripts were written in developing the data acquisition system.

Chapter 3

Discharge and Optical Performance

Study of the optical performance of this unique laser system involved observation of pulsed output over an extended range of average power levels. As mentioned previously, the existing system was designed for CW operation. As a result, the DC power supply pumping voltage was a primary limitation in this work. Thus, for this detailed parametric study of pulsed phenomenon, maximum average laser power was limited to about 6 kW.

3.1 Data Collection

Observation of the optical performance of the system indicated that a grid of sample data accurately represented the operational range. Data in Table 3.1 was collected at 2, 4 and 6 kW average power levels for each combination of f_b and N listed. Burst frequencies sampled were based on division of a 5 kHz clock, as discussed in Section 2.2.1. Choice of N at each frequency was a function of burst duty cycle (D_b) defined herein as:

$$D_b = \frac{N \cdot f_b}{5000} \cdot 100\% \quad (3.1)$$

Optical output data for D_b increments ranging from 5 to 50% was collected to identify a representative sample set. It was found that at D_b below 10%, insufficient pumping voltage was available to operate over the full range of f_b . Further, at D_b greater than 40%, optical pulses were found to overlap. Thus, N sampled at 10, 20 and 40% was determined to be representative of the overall pulse range. An additional sampling at $N=7$ was performed

Burst Frequency (Hz)	Number of Pulses (N)				
	Approximate Burst Duty Cycle (%)				
	10		20	40	
75	7		13	27	
100	5	7	10	20	
125	4	7	8	16	
152	3		7	13	
172	3		6	7	12
200	3		5	7	10
250	2		4	7	8
294	2		3		7
357	2		3	6	7
417	1		2	5	7
500	1		2	4	7
625	1		2	3	7
5000 (CW)	1				

Table 3.1: Optical and discharge current data collection grid summary for the 3 power levels collected. Optical and current data taken at each combination of f_b and N.

at each f_b as an additional control variable.

During the course of this work, a significant mechanical-frequency modulation of the optical output was discovered. Mechanical vibration stemmed from the gas transport blowers which were not adequately isolated from the optical bench. As such, low frequency vibration of the resonator mirrors lead to momentary changes in cavity alignment. In order to accommodate this fact, all optical data presented here was the result of averaging over 16 individual periods. Averaging was accomplished with the digital storage oscil-

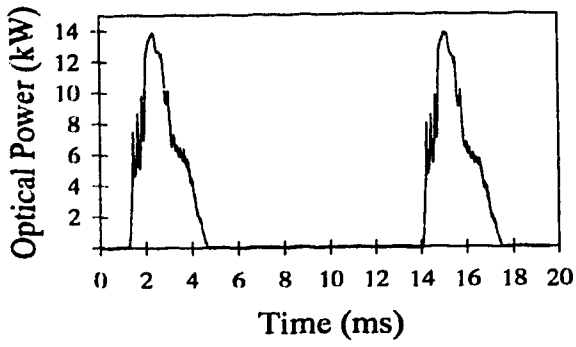
oscope discussed in Chapter 2.

3.2 System Trends.

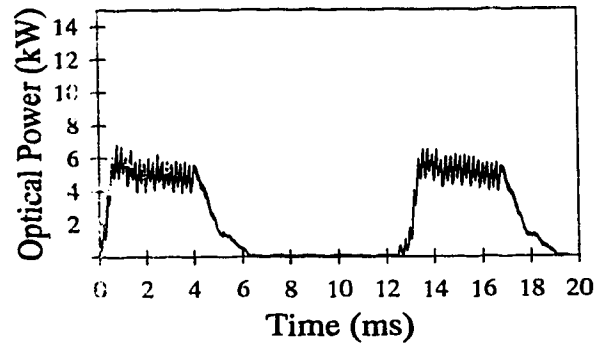
To quantify system operation in pulsed mode over the range of powers, the following figures are presented. Figure 3.1 represents operation of the laser system at 2 kW average power. Figures 3.2 and 3.3 represent 4kW and 6kW performance, respectively. The specific waveforms illustrated in these figures clearly indicate the broad range of optical outputs possible with this unique burst excitation technique. At low f_b , pulses are well defined and fall to zero power in-between pulses. This operational feature is illustrated by (A) and (B) in each figure. At the mid range of f_b , pulses become less defined and a constant light level exists in between each pulse event, see (D) in each figure. Ultimately, part (E) of each figure represents f_b increased to yield CW output. It is obvious from these figures that an identifiable optical output trend exists which is independent of average power level. For this reason, 4 kW data is used predominantly throughout this study as a representative example of device performance. Now that an overall optical trend has been established, a detailed examination of the optical waveforms presented is possible.

3.3 Discharge Characteristics

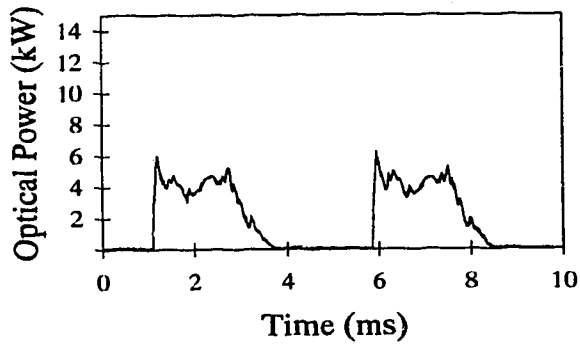
Figure 3.4 illustrates the dependence of average discharge current and DC voltage on burst frequency, under conditions of constant laser power. Figure 3.4 can be interpreted as follows. To achieve a given average current at a lower burst rate, an increase in DC voltage is required. This follows because the vibrational pumping field strength must compensate for a reduced production of electrons by gated pulser photoionization. Since the



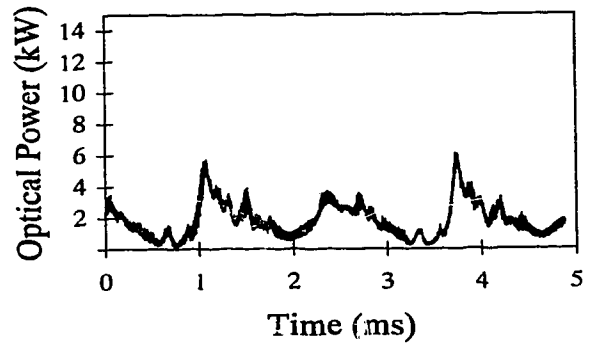
(A)



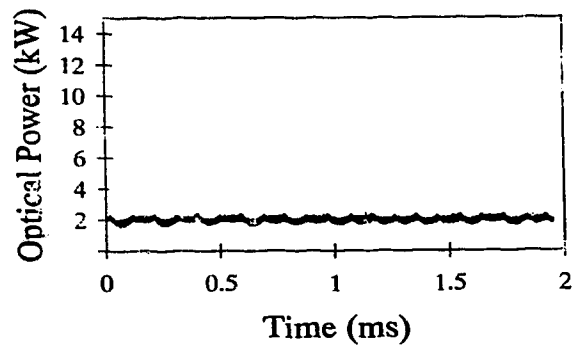
(B)



(C)

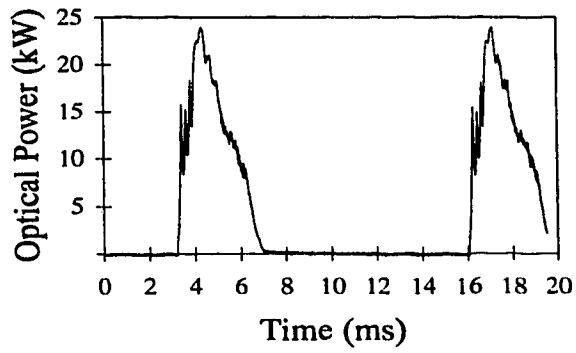


(D)

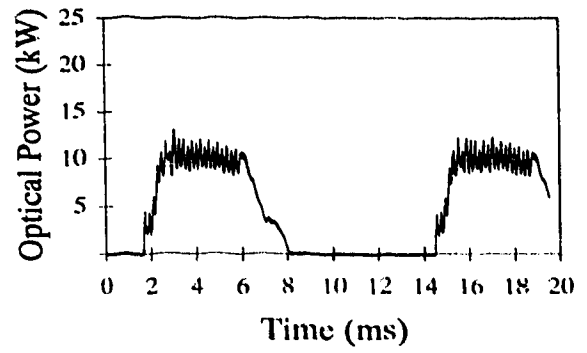


(E)

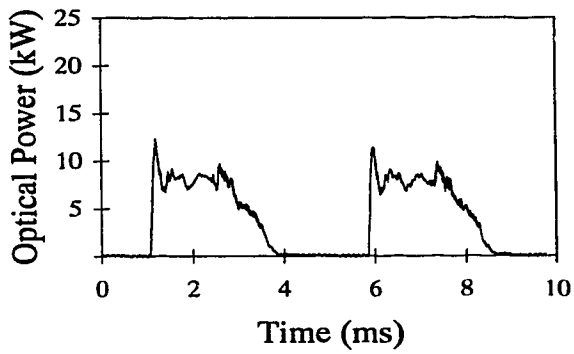
Figure 3.1: 2 kW average power pulsed optical output. (A) 75 Hz, 7 pulses, (B) 75 Hz, 27 pulses (C) 200 Hz & 3 pulses, (D) 357 Hz & 3 pulses, (E) CW.



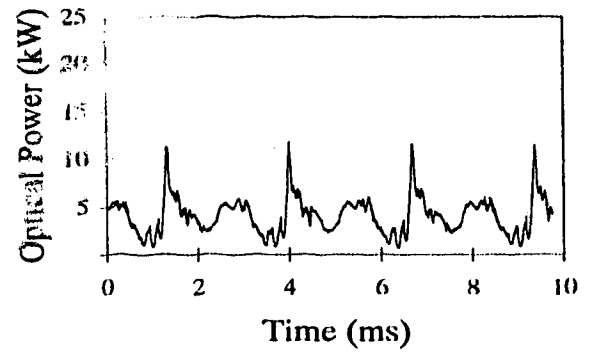
(A)



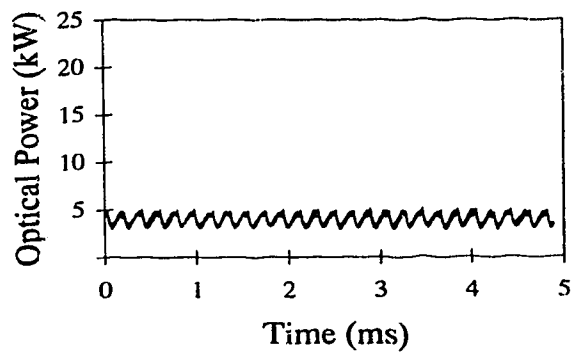
(B)



(C)

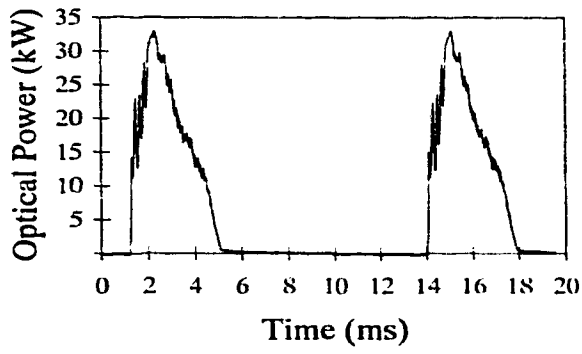


(D)

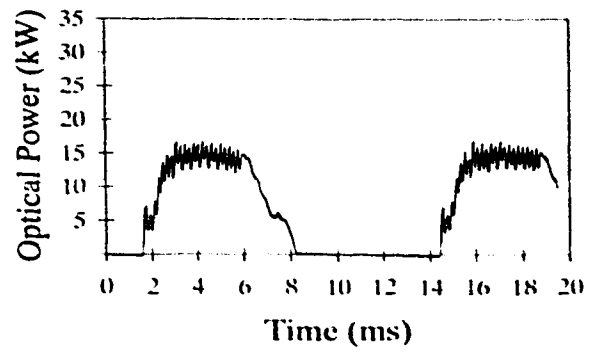


(E)

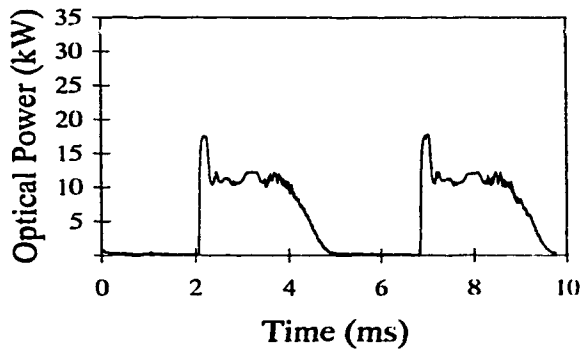
Figure 3.2: 4 kW average power pulsed optical output, (A) 75 Hz, 7 pulses, (B) 75 Hz, 27 pulses (C) 200 Hz & 3 pulses, (D) 357 Hz & 3 pulses, (E) CW.



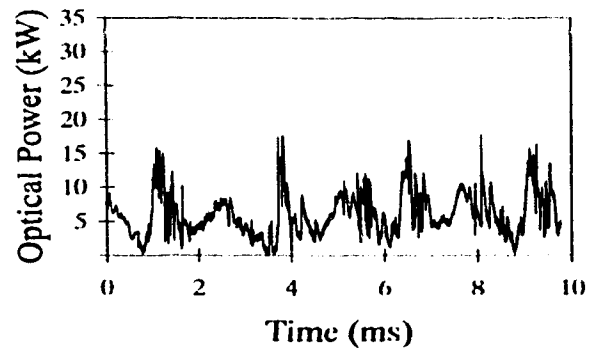
(A)



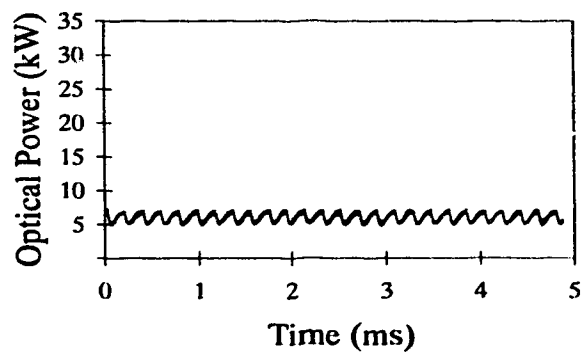
(B)



(C)



(D)



(E)

Figure 3.3: 6 kW average power pulsed optical output, (A) 75 Hz, 7 pulses, (B) 75 Hz, 27 pulses (C) 200 Hz & 3 pulses, (D) 357 Hz & 3 pulses, (E) CW.

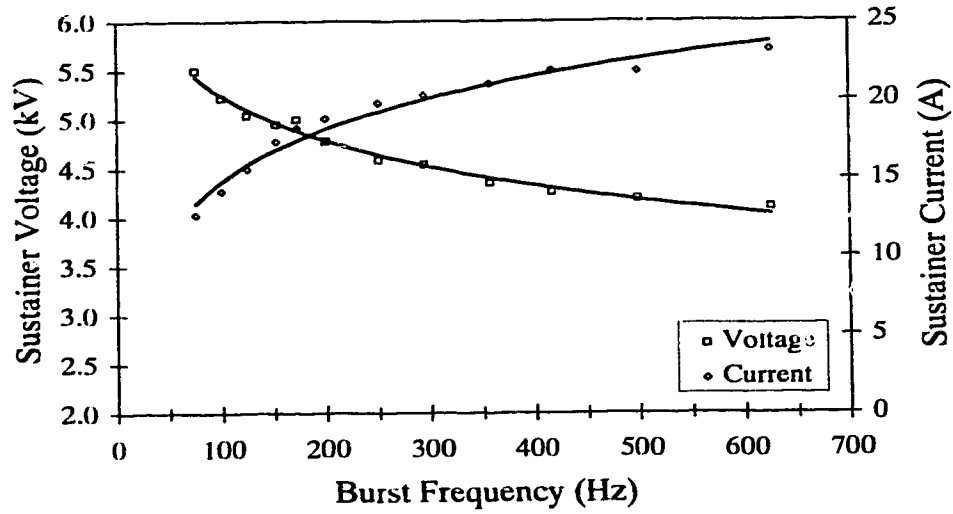


Figure 3.4: Discharge voltage and current with respect to f_b . $P_{av}=4kW$, $N=7$.

curves in Figure 3.4 are for constant output power, the required increase in DC voltage at lower burst rates corresponds to current increasing with higher burst rates.

It may also be noted in Figure 3.4 that laser efficiency improved from 4 to 6% as burst frequency was decreased from CW. Presumably this trend exists because the higher discharge E/n required at lower burst rates is more optimal for upper laser level pumping.

3.4 Optical Characteristics

As mentioned earlier, burst excitation involved modification of the CW driver in the system. Consequently it became feasible to produce laser output ranging from a purely pulsed profile to CW. In order to appreciate the nature of the optical output produced by this system, it is necessary to consider the discharge current associated with each optical

event. Figure 3.5 details optical and current waveforms at $f_b = 75$ Hz, $N = 7$ and $P_{av} =$

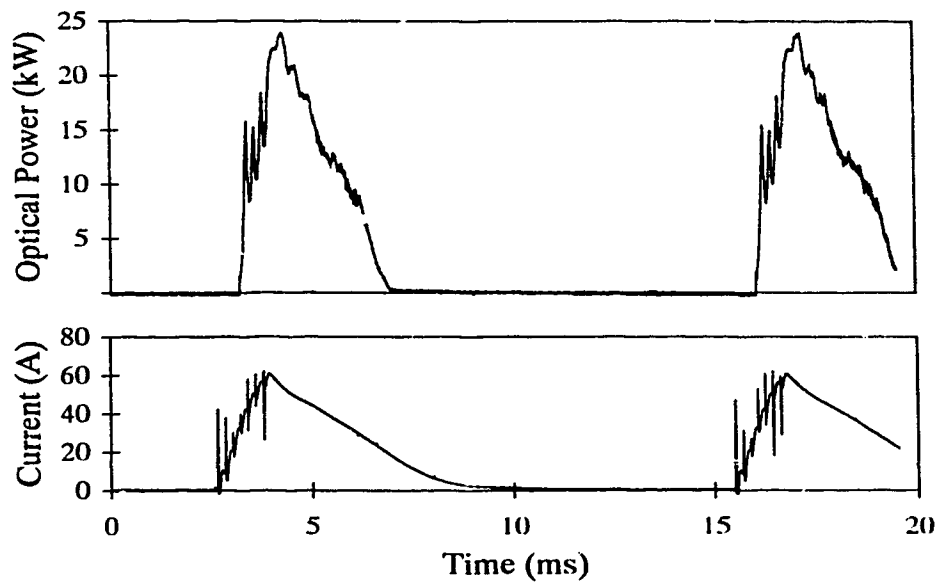


Figure 3.5: 4 kW Optical output and discharge Current, $f_b=75$ Hz, $N=7$.

4kW, representing the lower end of the f_b scale. In this regime, optical output is characterized by high peak power and zero laser power in-between pulses. At low f_b and large N , a typical optical output is found in Figure 3.6. Profiles represented in these two figures are referred to as the “distinct-pulse regime”. Figures 3.7 and 3.8 reflect 4 kW, $N = 3$, operation at 200 Hz and 357 Hz, respectively. In Figure 3.8, the pulse component of the optical output is less defined and a significant continuous offset exists between pulses.

A detailed discussion of the features presented in Figures 3.7 and 3.8 is included below. Figure 3.9 is a typical plot of the discharge current and optical output of the system under CW conditions. It is observable that CW output of the system is oscillatory in

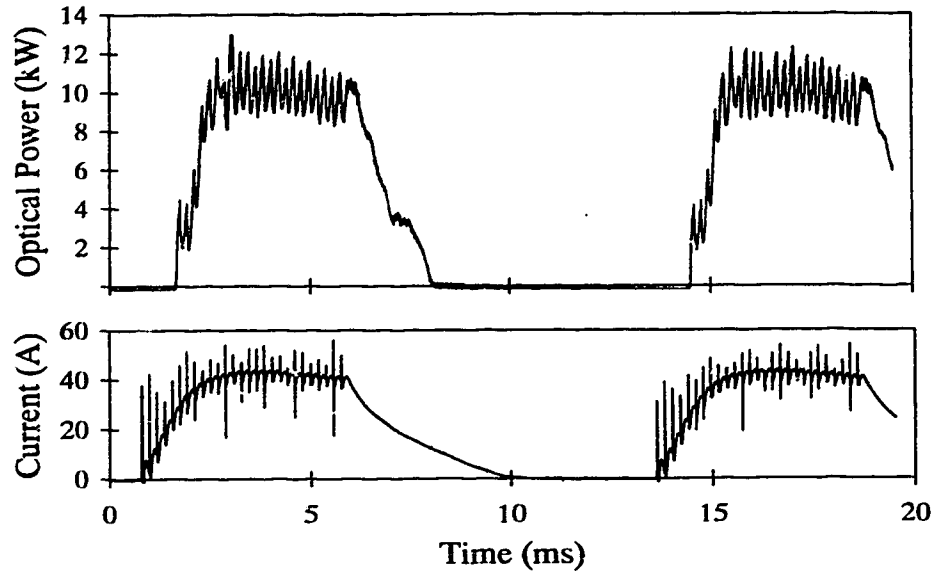


Figure 3.6: 4 kW Optical output and discharge Current, $f_b=75$ Hz, $N=27$.

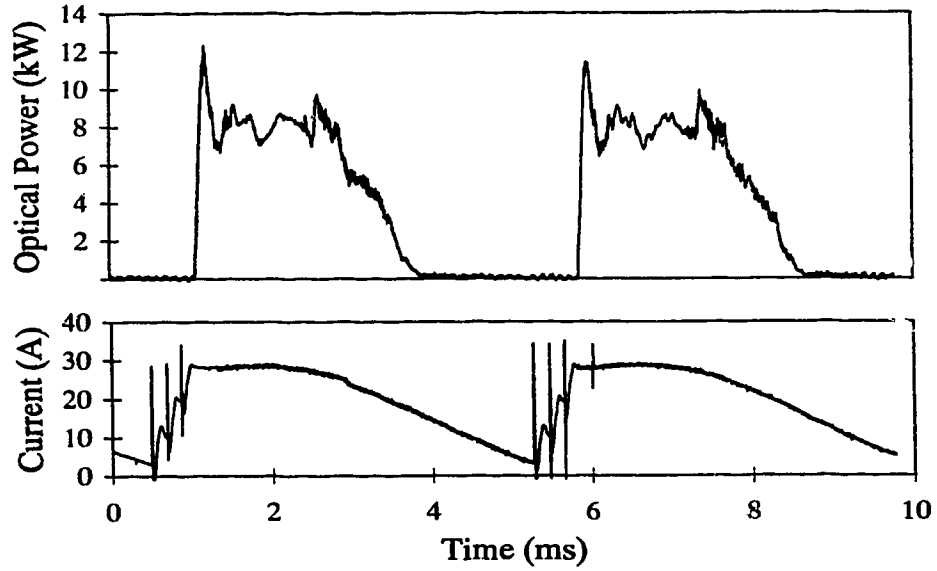


Figure 3.7: 4 kW Optical output and discharge Current, $f_b=200$ Hz, $N=3$.

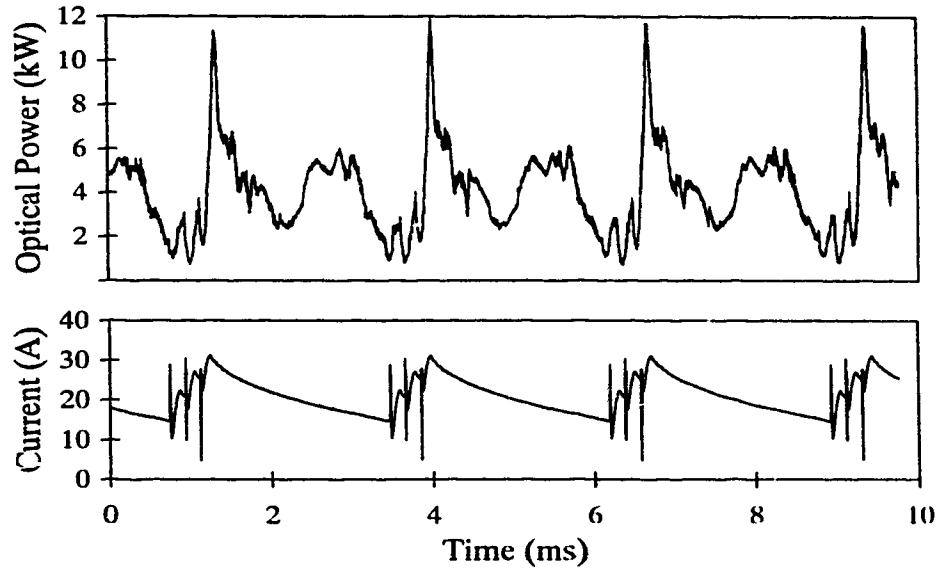


Figure 3.8: 4 kW Optical output and discharge Current, $f_b=357$ Hz, $N=3$.

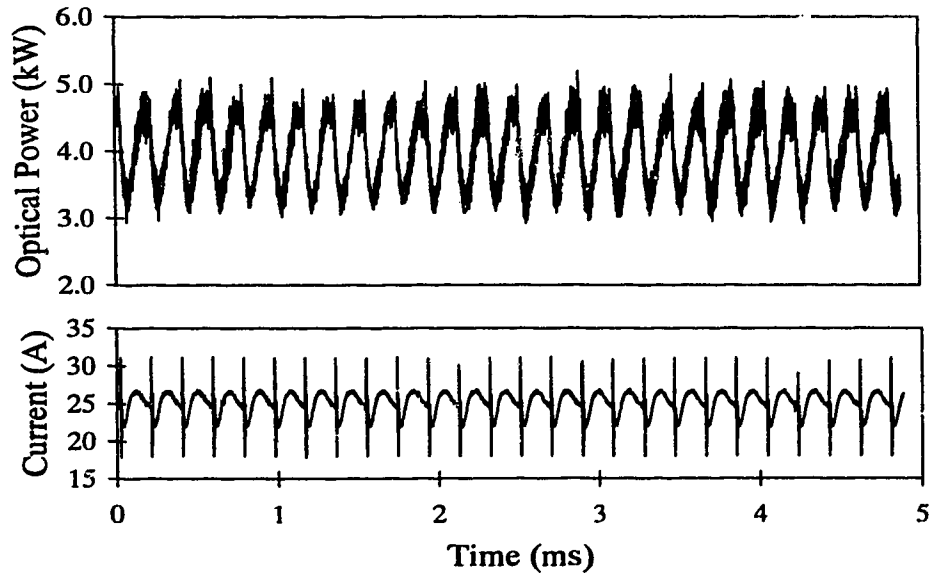


Figure 3.9: 4 kW CW Optical output and discharge current.

nature; a result of the 5 kHz ionization sequence. Another common feature illustrated in

all discharge current figures is the presence of short duration vertical spikes in the current waveforms, coincident with each ionization impulse event.

In the “distinct-pulse regime,” illustrated in Figure 3.5, each successive impulse increases discharge conductivity; with a net increase in electron density over each pulse cycle. If N was increased with f_b held constant, ultimately an equilibrium state would be reached, where electron loss over the pulse period offsets electron creation over the same interval. Such an asymptotic approach to equilibrium is evident in Figure 3.6. This effect is characteristic of a burst excited discharge, heavily influenced by its DC supply. The non-self-sustaining nature of the discharge is apparent in Figure 3.5, where discharge current decays to zero between bursts. Current rise and decay are limited by arc suppression inductors installed in the DC power supply of Figure 2.3.

Under higher f_b excitation, discharge conductivity has insufficient time to decay to zero between bursts. Thus, as shown in Figure 3.8, the discharge current is not extinguished. Fast rising leading spikes are characteristic of low N cases, illustrated in Figure 3.7. Interestingly, the optical waveform retains the spiked characteristic of gain switching, although it does not decay to zero between bursts. The spike is likely a result of more rapid pumping, and higher efficiency, due to a higher E/n ratio required to compensate for smaller pulse number. Figure 3.7 features the rapid rise associated with low N and square pulse profiles.

In Figure 3.9 the current waveform approaches steady-state asymptotically as either N or f_b are increased. In this case, the discharge is excited by a continuous 5 kHz pulse stream. Changing discharge conditions over the pulse cycle results in periodic modulation

of the optical waveform. While Figure 3.9 indicates that CW output from this laser is not a simple continuous light level, welding performance is consistent with that found in other industrial systems. Under normal welding conditions, with processing times commensurate with industrially acceptable rates, this 5 kHz modulation is not significant.

Consideration of the unique features of the optical waveforms above, documents burst process flexibility. As discussed previously, high initial peak power leads to improved coupling of laser energy into the material surface while appreciable average power is still necessary to maintain acceptable processing rates in deep-penetration welds. The proceeding optical results illustrate that burst output encompasses both high peak and average power thereby lending itself to a wide variety of material processing applications.

3.5 Optical Results

Burst operation of this laser system provides a wide range of optical output characteristics. Low frequency excitation induces fast rising, well defined, independent optical pulses with peak powers in excess of 5 times the CW or average laser power. A typical optical output produced at 75 Hz and 7 pulses is shown in Figure 3.5. Increasing burst frequency results in continuous laser output in-between pulses, Figure 3.8. Ultimately, the burst frequency can be increased to produce CW optical output as in Figure 3.9. The importance of these features will be investigated with particular emphasis on their utility in laser welding.

Burst pulsed optical output is characterized here in terms of three parameters, namely: peak optical power (P_p), energy per pulse (E_p) defined in (3.2) and optical duty cycle (D_o).

Optical duty cycle is defined as the “on-time” of the laser pulse with respect to the signal period.

$$E_p = \frac{P_{av}}{f_b} \quad (3.2)$$

As discussed previously, pulse shape is potentially of relevance in laser-materials interactions. However, a detailed investigation of pulse shape is beyond the scope of this investigation. For this reason, only preliminary observations regarding pulse shape are presented in the context of future study.

P_p and E_p are critical factors in determining maximum penetration achievable with the process. Deep penetration welding performance is closely linked to the peak power (P_p) deliverable by the laser. In general, higher peak optical power results in deeper weld penetration, for a given processing rate. There also exists a threshold of E_p which yields complete substrate penetration thereby forming a keyhole. At this point, f_b and welding speed also play a role in maintaining the keyhole. Closely linked to P_p and E_p is D_o , which represents the “on-time” of the optical output in the pulse train.

The data derived from this investigation will serve to clarify the relationship of these parameters to each other and on the overall welding sequence. Significant experimental documentation on CW laser welding is available in the scientific literature. However, to date, few investigations of deep penetration laser welding using high average power, high peak power, pulsed CO_2 lasers have been reported. For this reason, this study deals exclusively with the “distinct-pulse” or low frequency regime of the burst process.

3.6 Empirical Relationships

As indicated above, burst excitation is capable of producing a variety of optical outputs. This flexibility is well illustrated in Figure 3.10. From this plot, the transition from

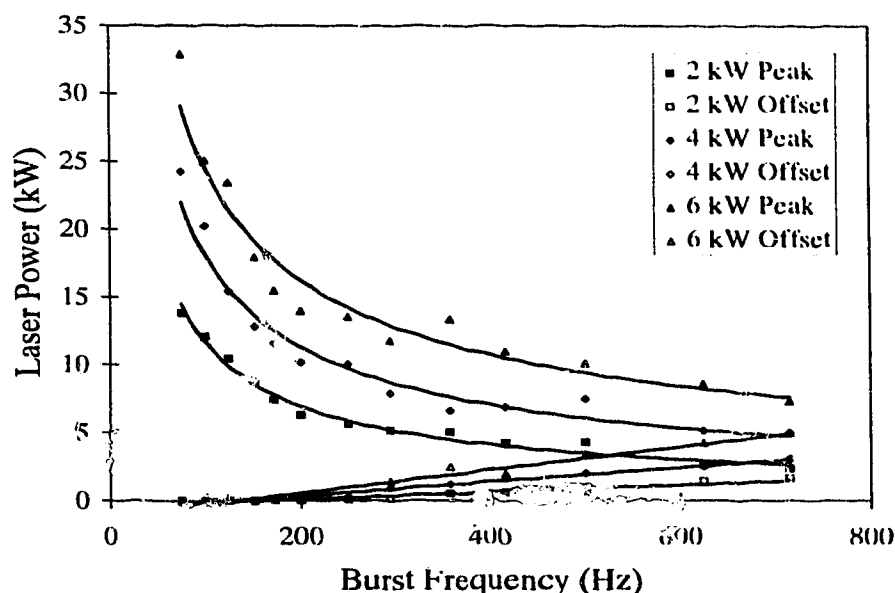


Figure 3.10: Dependence of laser peak and offset power on burst frequency and average laser power for 7 pulses.

distinct-pulse to CW is easily distinguished. As f_b increases, peak power begins to decrease. At approximately 200 Hz, a continuous offset or non-zero power level appears in-between the optical pulses. Finally at 715 Hz and $N=7$, CW operation is achieved. Referring to Figure 3.9, CW performance can be interpreted as the average of the peak power and offset. This is indicated on the right hand side of Figure 3.10. Figure 3.10 further demonstrates that the trend is independent of average laser power. It is the distinct-pulse regime, at f_b less than 200 Hz that is of primary interest in this study.

Designing a welding specification for traditional arc welding processes involves choosing major process parameters including, arc current, material preparation and electrode type. Laser welding generally requires little substrate preparation and is further simplified by the lack of an electrode. However, designing a pulsed laser welding specification does require intimate knowledge of the optical parameters. Conveniently, this work yielded simple empirical relationships which adequately summarize the results; and thereby greatly facilitated designing a pulsed laser welding specification. The following discussion will demonstrate that burst optical output in the pulse-periodic regime can be easily predicted through the use of two simple empirical relationships.

3.6.1 D_o Development

Optical duty cycle is inversely proportional to peak power when average power is held constant, as indicated in Figure 3.11. This feature follows from conservation of energy. At small optical duty cycles, a large gain-switched population inversion results in extremely high P_p with subsequent rapid decay. Peak power begins to drop off as D_o increases, due to a weaker pumping of the gain media. Indeed, for a given average power deposition, the larger the excitation duty cycle the smaller the initial gain switched population inversion.

In the distinct-pulse regime, D_o is roughly proportional to f_b , and depends only weakly on total average power; see Figure 3.12. As f_b increases, the D_o vs. f_b characteristics for different power levels become non-linear and diverge from one another. It is further observed in the distinct-pulse regime that D_o depends simply on N . In the following section, an empirical equation for D_o as a function of f_b and N is developed.

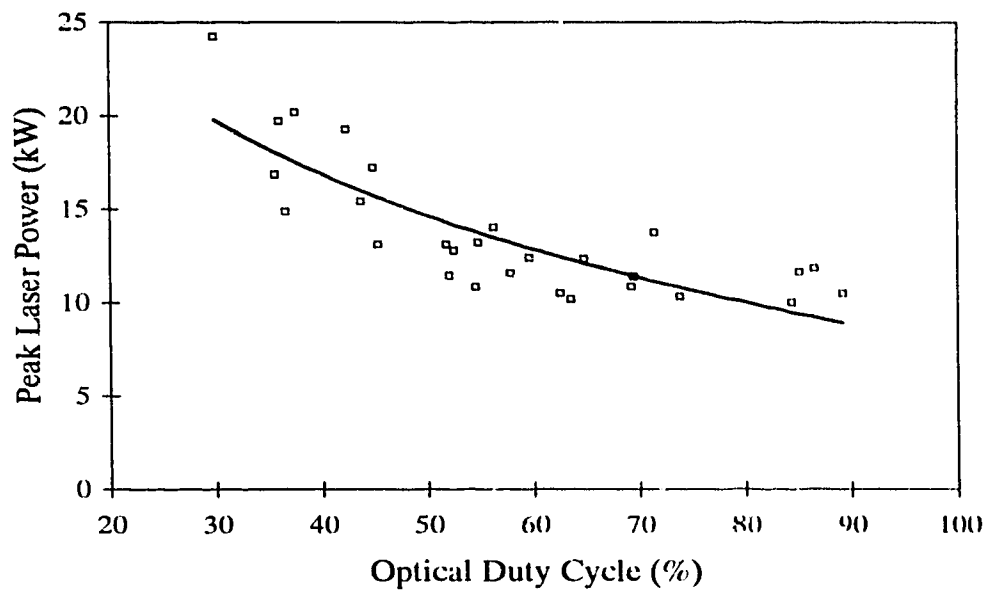


Figure 3.11: Peak laser power with respect to optical duty cycle at 4 kW average power.

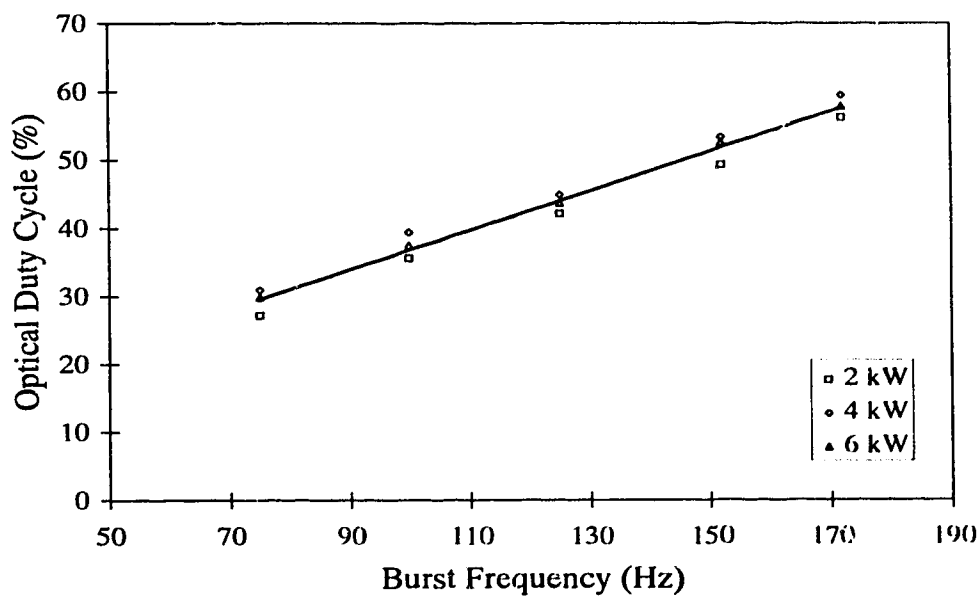


Figure 3.12: Dependence of optical duty cycle on burst frequency and average laser power for the case of 7 pulses.

First, consider the dependence of D_0 on f_b with N held constant at 7. Figure 3.12 illustrates this dependence for the three power levels in question. Only a weak dependence of D_0 on laser power is observed. Neglecting said dependence, the best linear fit to the data of Figure 3.12 is:

$$D_0|_{N=7} = 0.290f_b + 7.85 \quad (3.3)$$

Next, consider the dependence of D_0 on N , for several different burst frequencies. Figure 3.13 presents experimental results for the case where the average power is 4 kW.

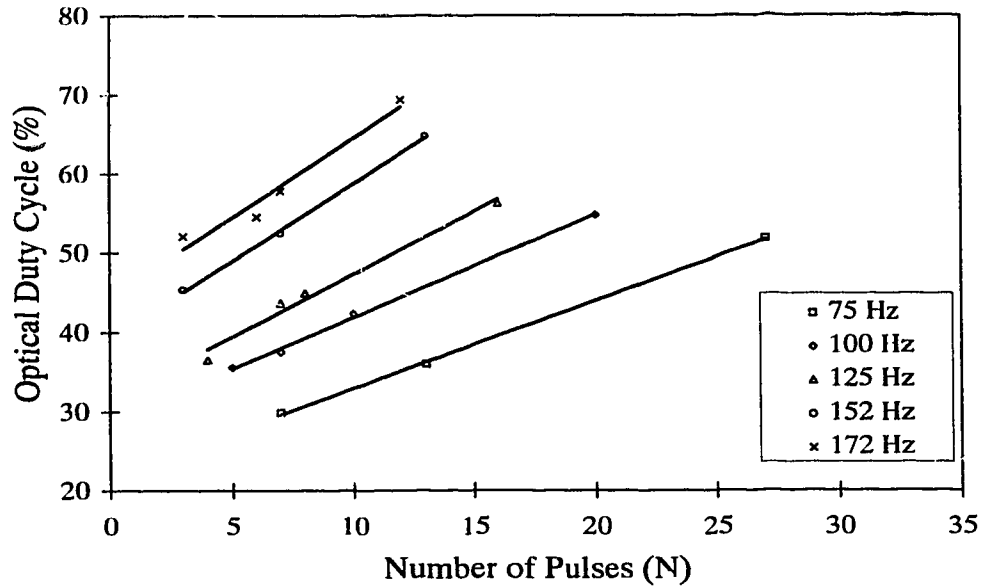


Figure 3.13: Optical duty cycle with respect to number of pulses at an average power of 4kW.

Dependence at each frequency is essentially linear, and may be represented by:

$$D_0 = \alpha N + \beta \quad (3.4)$$

Table 3.2 is a summary of the best fit linear relationships for the combined data of all

f_b	α	β
75	1.15	21.6
100	1.39	27.1
125	1.64	32.6
152	1.91	38.5
172	2.11	42.9

Table 3.2: Best fit linear relationships for all power levels.

power levels. Conveniently, α is a linear function of f_b , Figure 3.14, with a confidence

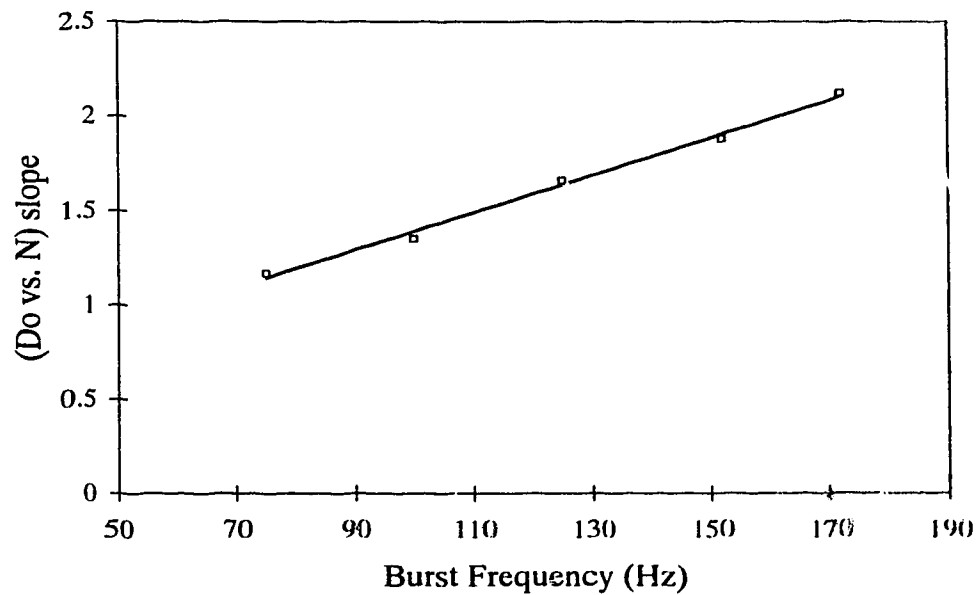


Figure 3.14: Optical duty cycle vs. N slope with respect to burst frequency.

factor, $R^2 = 0.99$. The best fit linear function is:

$$\alpha = 0.010 f_b + 0.40 \quad (3.5)$$

The general empirical equation for D_o , having the form of (3.4), now follows from (3.3) and (3.5):

$$D_o = (0.010 f_b + 0.40)N + 0.22 f_b + 5.0 \quad (3.6)$$

3.6.2 P_p Development

In the absence of offset power, P_p is observed to depend most strongly on E_p , and also to a lesser extent on N . An empirical equation for P_p as a function of E_p and N is next hypothesized.

Experiments indicate that P_p depends most weakly on N for $N < 15$. A large fraction of the observed dependence of P_p on N appears to be due to random experimental error. If P_p is averaged over N , a simple relationship between average P_p and E_p results, which is illustrated in Figure 3.15 for the three power levels considered in this work. The relationship is well approximated as:

$$P_p = 1.2 \cdot E_p^{0.75} \text{ kW} \quad (3.7)$$

Consistency of the trend is partial justification for the averaging, as is the degree of agreement between empirical predictions and experimental data, summarized in the following sections. Further semi-quantitative justification is possible. In other preliminary analysis, it appears that the N dependence may be described in terms of dependence on pulse profile shape. A simple numerical characterization of the pulse shape follows from a

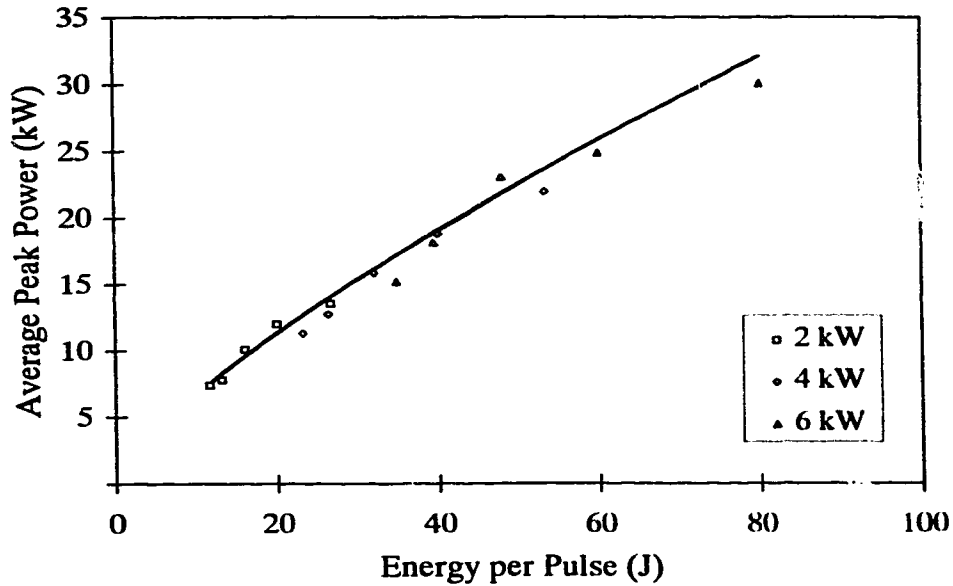


Figure 3.15: Average peak laser power with respect to energy per pulse for all three power levels.

“shape factor” (S_f) defined as:

$$S_f = \frac{f_b E_p}{D_o P_p} \quad (3.8)$$

Physically, $S_f=0.5$ corresponds to a triangle, and $S_f=1.0$ corresponds to a rectangle and $S_f=0$ represents an indeterminate shape. Over the range of experiments considered here, S_f varies by about 30%. Again, much of this variation is likely due to random experimental error. In the distinct-pulse regime, it is observed qualitatively that the pulse shape varies little for $N<15$, Figure 3.16. The limitation on N can be rephrased as a condition of similar shape factor. A dramatic change in shape factor is evident on transition to higher f_b , Figure 3.16. It appears possible to also correlate the change in α to a change in shape factor.

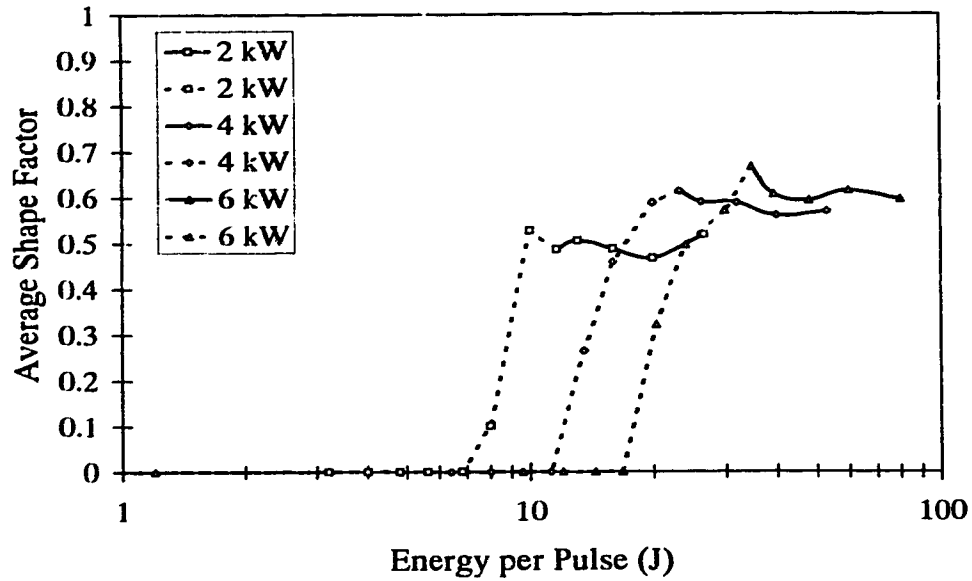


Figure 3.16: Average S_f with respect to E_p at the three power levels in question. Solid lines represent the distinct pulse regime, dashed lines indicate higher frequency operation.

3.7 Empirical Relation Tests

3.7.1 Optical Duty Cycle Test

A first test of empirical (3.6) is to consider the dependence of D_o on N and f_b at the power levels in question. Empirical lines plotted over experimental data for 2, 4, and 6 kW are presented in Figures 3.17, 3.18 and 3.19, respectively. The experimental data is seen to be well represented by the empirical equation in these figures. Quality of agreement between experimental data and empirical predictions is within 5% for all other power levels considered.

As a further test of (3.6), the dependence of D_o on E_p is considered, with respect to D_b . Note that burst duty cycle depends on both N and f_b . Experimental data is again well rep-

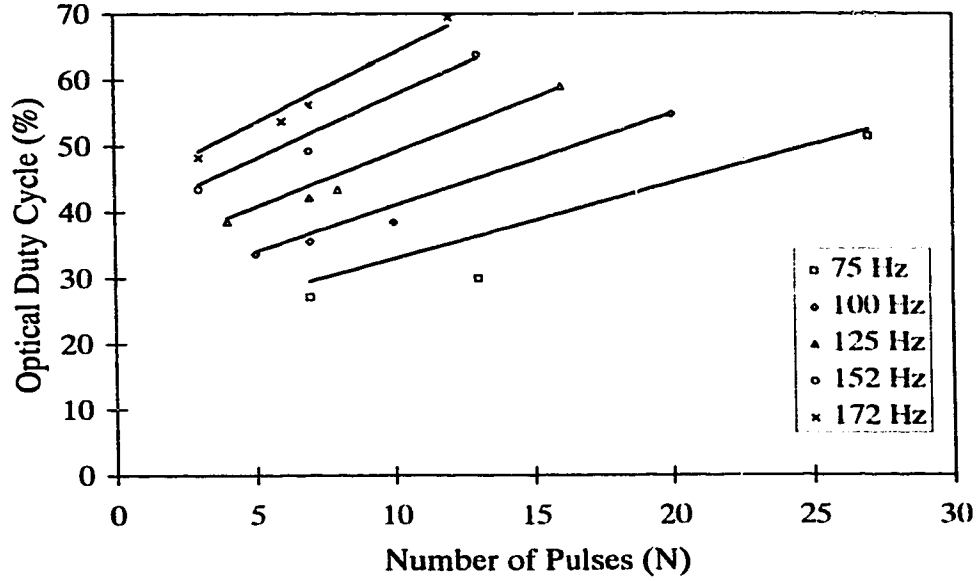


Figure 3.17: Optical duty cycle as a function of number of pulses and burst frequency at an average power level of 2 kW. Points are experimental data and solid lines represent (3.6).

resented at 2, 4, and 6 kW by (3.6) in Figures 3.20, 3.21 and 3.22, respectively. A range of burst duty cycles from 10 to 40% were considered, and in all cases the discrepancy between experiment and empirical prediction was approximately 5%. Given this degree of agreement, (3.6) does seem to capture the essence of D_o dependence on the discharge control parameters.

3.7.2 Peak Power Test.

A first test of the validity of the relationship in (3.7) is to consider the dependence of P_p on E_p , at 2, 4, and 6 kW, as in Figures 3.23, 3.24 and 3.25, without averaging over the dependence on N . All experimental data for N less than 15 is presented along with (3.7) in these figures. The discrepancy at 6 kW is less than 25% for E_p above 40J, where the

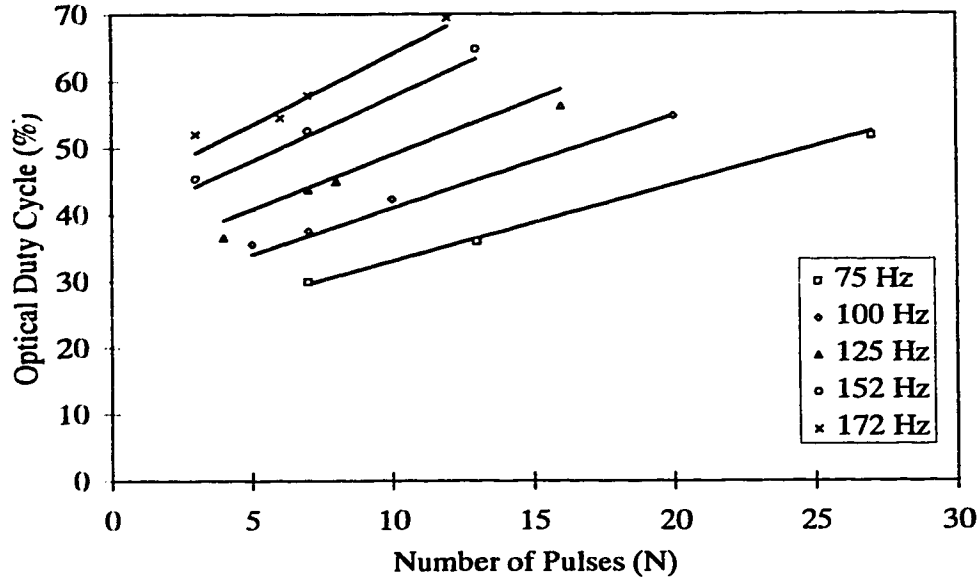


Figure 3.18: Optical duty cycle as a function of number of pulses and burst frequency at an average power level of 4 kW. Points are experimental data and solid lines represent (3.6).

dependence of P_p on N is weaker. For 2 and 4 kW, the agreement is marginally better. Although (3.7) accurately represents the dependence of P_p on E_p , as indicated in Figure 3.15, it is apparent from these figures that it does not capture the entire functional dependence.

It is instructive to consider a further test of (3.7), namely, the dependence of P_p on f_b for constant N . Since f_b is inversely proportional to E_p , this test is equivalent to the first, with constant N . In Figures 3.26, 3.27 and 3.28 the experimental data for $N=7$ is compared with (3.7). The discrepancy is less than 10%, typical of the 2 and 4 kW data. For the 6 kW data, the discrepancy is larger, at approximately 25%.

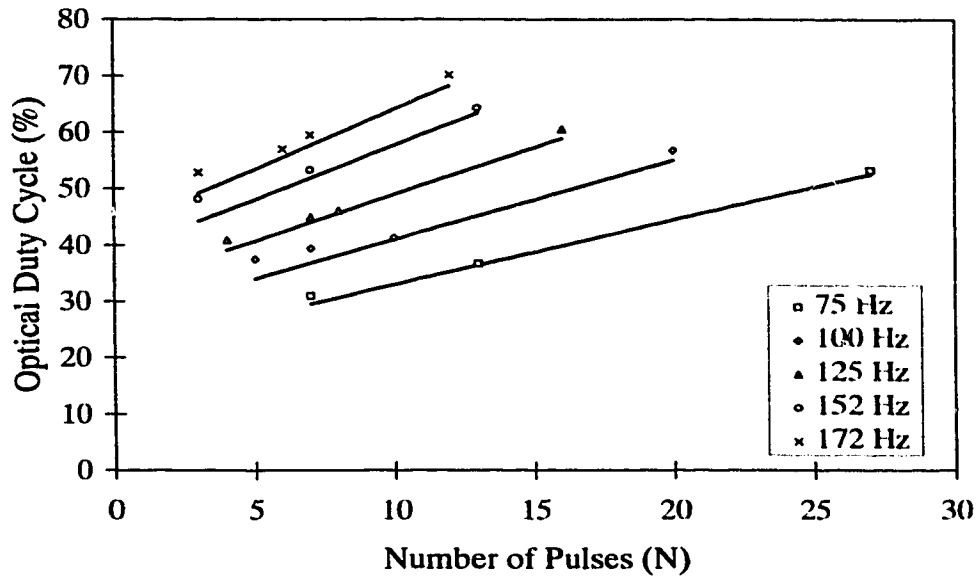


Figure 3.19: Optical duty cycle as a function of number of pulses and burst frequency at an average power level of 6kW. Points are experimental data and solid lines represent (3.6).

3.8 Discussion

Burst operation of the CO₂ laser in question has resulted in a significant increase in system flexibility. This unique laser process is amenable to multi-kilowatt average power operation with simultaneous control of pulse duration and peak power. Although not demonstrated here, pulse shape is also subject to control.

Investigation of the distinct-pulse regime indicates that laser output characteristics are predicted through the use of two simple empirical relationships. Both optical duty cycle and peak power can be controlled through choice of excitation burst frequency, number of impulses and average laser power. Importance of these empirical relationships is manifest in improved control of critical parameters which govern deep penetration welding per-

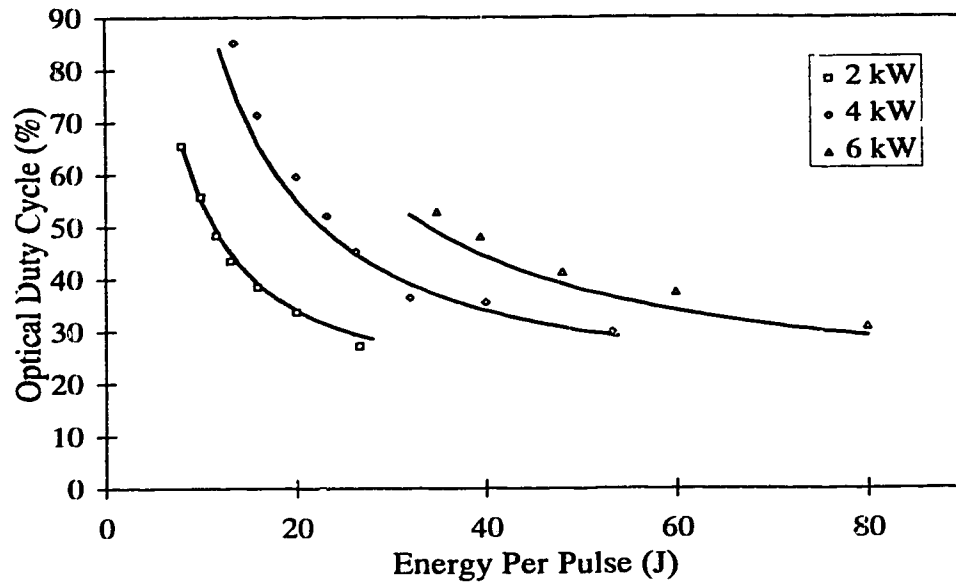


Figure 3.20: D_o with respect to E_p and average laser power at a burst duty cycle of 10%. Points are experimental data and solid lines represent (3.6).

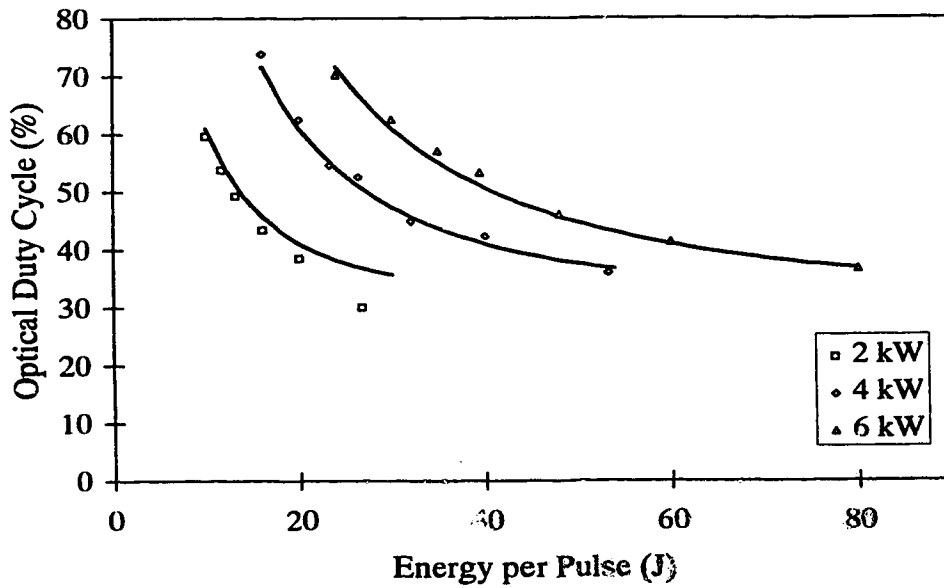


Figure 3.21: D_o with respect to E_p and average laser power at a burst duty cycle of 20%. Points are experimental data and solid lines represent (3.6).

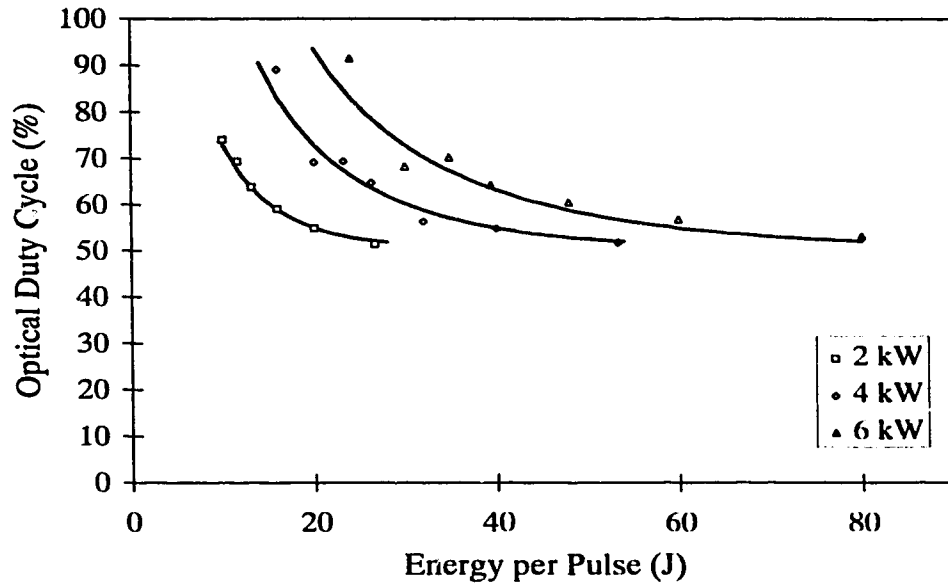


Figure 3.22: D_o with respect to E_p and average laser power at a burst duty cycle of 40%. Points are experimental data and solid lines represent (3.6).

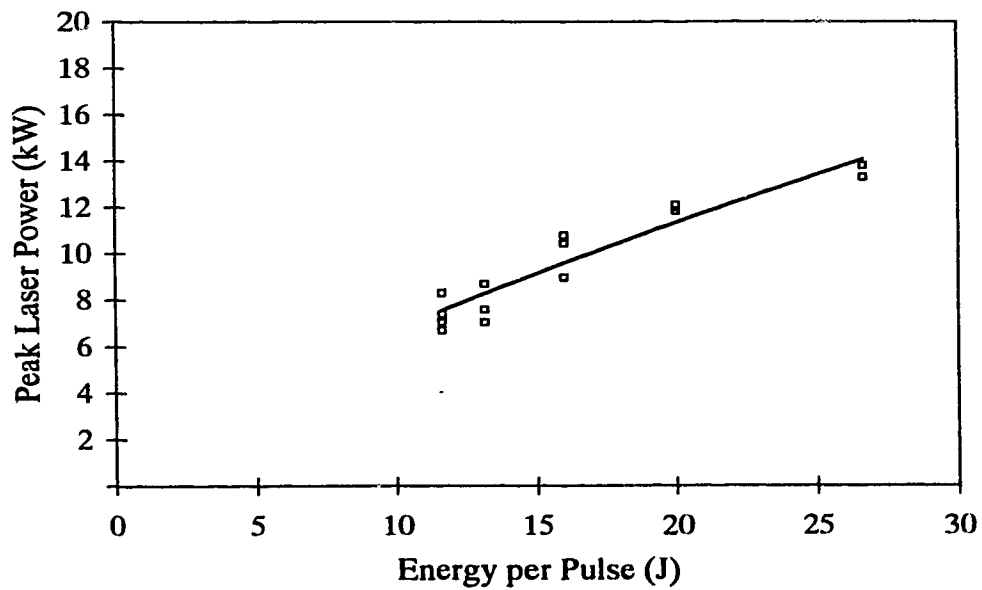


Figure 3.23: Dependence of P_p on E_p at $P_{av} = 2$ kW for $N < 15$. Points are experimental data and the solid line represents empirical (3.7).

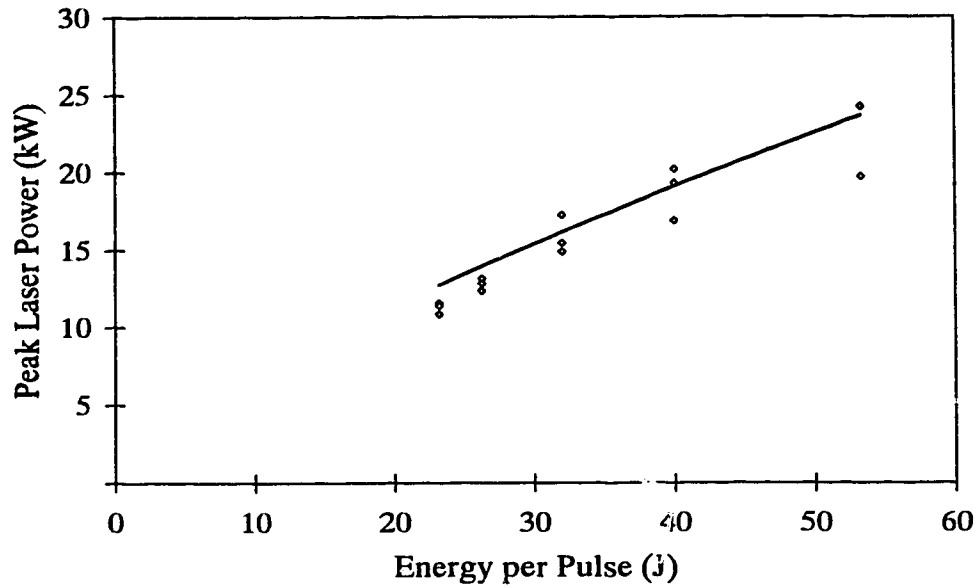


Figure 3.24: Dependence of P_p on E_p at $P_{av} = 4$ kW for $N < 15$. Points are experimental data and the solid line represents empirical (3.7).

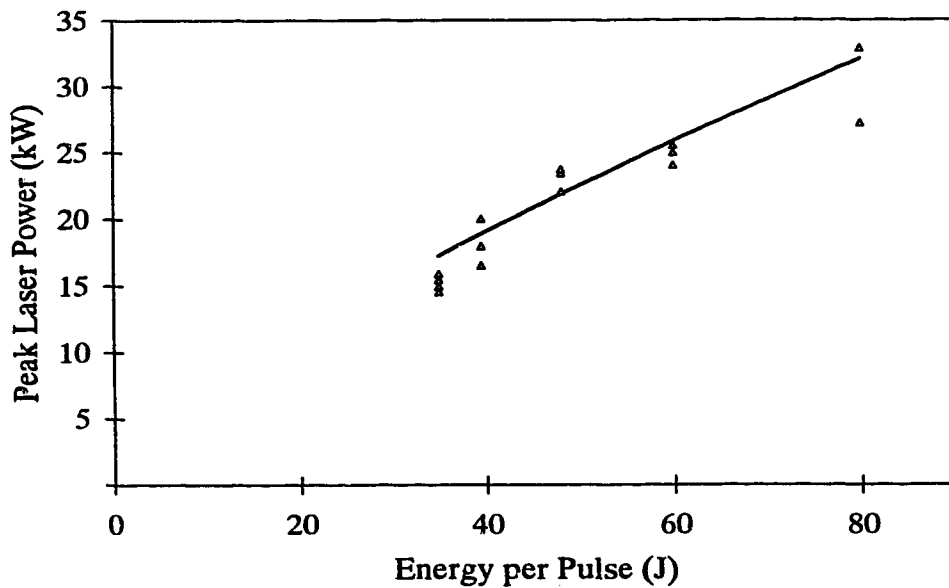


Figure 3.25: Dependence of P_p on E_p at $P_{av} = 6$ kW for $N < 15$ pulses. Points are experimental data and the solid line represents empirical (3.7).

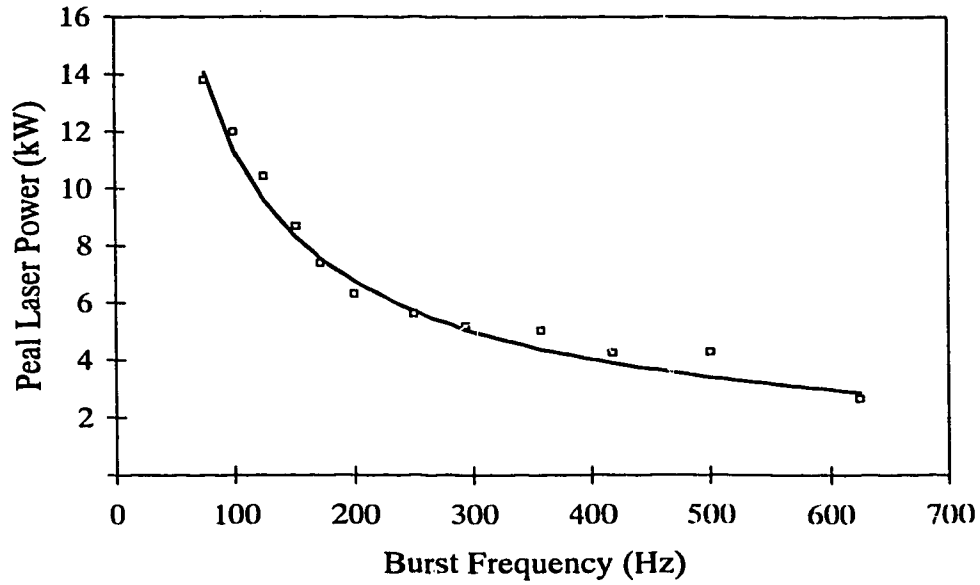


Figure 3.26: P_p with respect to f_b at $P_{av} = 2$ kW with 7 pulses. Points are experimental data and the solid line represents (3.7).

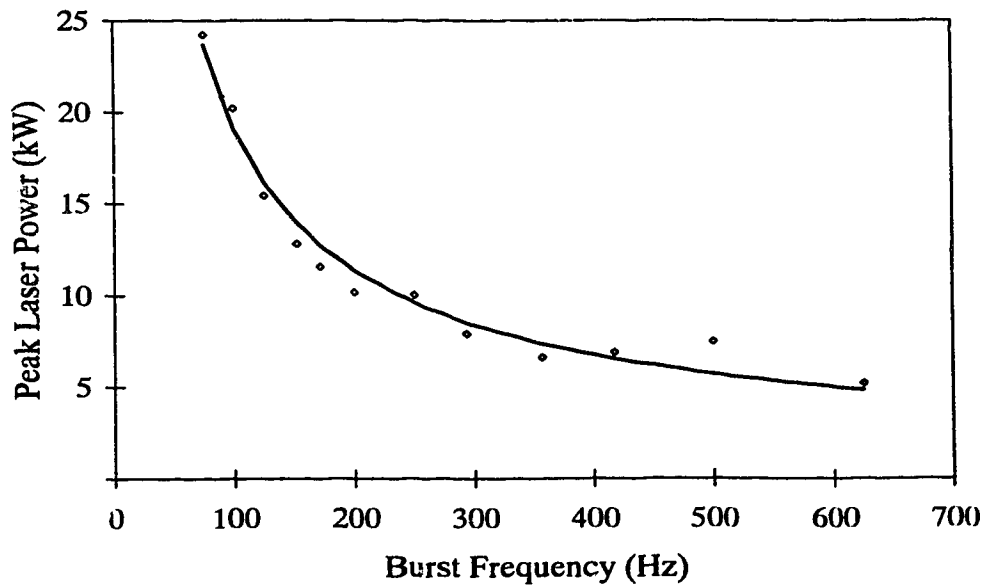


Figure 3.27: P_p with respect to f_b at $P_{av} = 4$ kW with 7 pulses. Points are experimental data and the solid line represents (3.7).

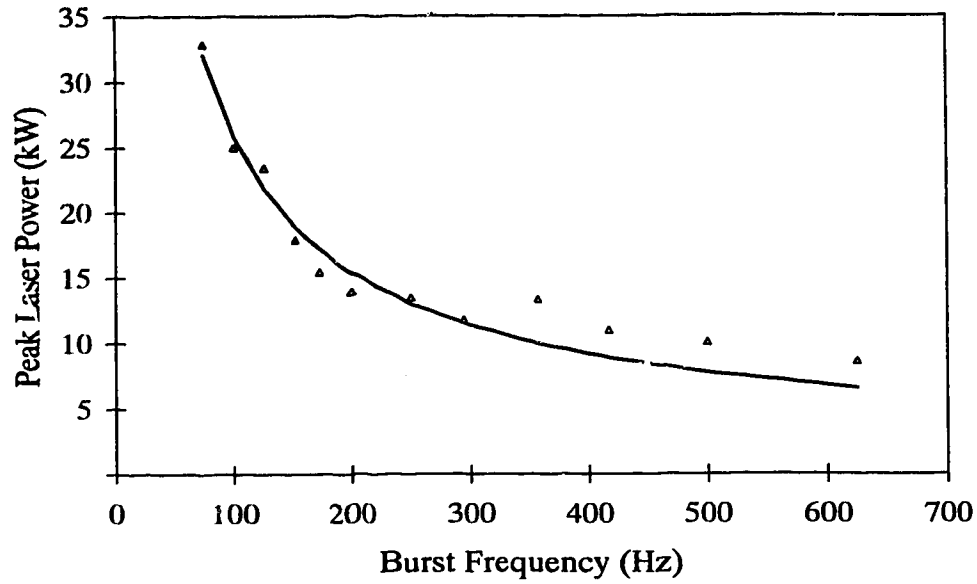


Figure 3.28: P_p with respect to f_b at $P_{av} = 6$ kW with 7 pulses. Points are experimental data and the solid line represents (3.7).

formance.

Validity of the empirical relationships is confirmed through a number of test cases where they accurately reproduce experimental data. In the first case, (3.6) represents the dependence of D_o on N and f_b with a 5% discrepancy. The second empirical relation, (3.7), represents the relationship between P_p , E_p and N with a maximum discrepancy of 25%. Improvement of this empirical relationship is anticipated through investigation of the functional dependence on N .

Chapter 4

Welding Performance

Deep penetration welding with CO₂ lasers has historically been limited by high capital investment and operating costs of multi-kilowatt laser systems. In general, only CW welding has thus far been extensively used in industry, due in part, to inflexible commercially available systems. Extensive scientific literature exists on all aspects of CW laser welding^{55,56,57}. To date, investigations of high-peak power, high average power laser welding have few citations. As such, the burst excitation process at issue here has an excellent potential to broaden application of CO₂ lasers in heavy section welding.

Results presented in Chapter 3 indicate that burst excitation of this PIE laser system results in a significant enhancement in flexibility of the system. With this technique, average power, peak power, pulse duration, pulse frequency and pulse shape are all subject to manipulation. Previously, only the average laser power in the system was subject to direct operator control. A full investigation of the possible applications of this new technique is beyond the scope of this work. For this reason, weld penetration was chosen as a representative test of the concepts discussed. This chapter will describe the performance of the various optical waveforms investigated in Chapter 3 with respect to weld penetration.

4.1 Data Collection

Welding experiments were performed to investigate the overall weld penetration

performance of the laser system in the distinct-pulse regime, as defined in Chapter 3. Laser welds presented here were performed at f_b and N combinations listed in Table 4.1. A

Burst Frequency (Hz)	Number of Pulses (N)			
	Approximate Burst Duty Cycle (%)			
	10	20	40	
75	7	13	27	
100	5	7	10	20
125	4	7	8	16
152	3	7	13	
172	3	6	7	12
5000 (CW)	1			

Table 4.1: Burst frequency and N combinations for laser welds performed in the complete study. Welds were performed at each combination of f_b and N at 2, 4 and 6kW laser power and 8, 12 and 16 mm/sec. welding speed.

weld was undertaken at each combination in Table 4.1 at 2, 4 and 6 kW laser power as well as 8, 12 and 16 mm/sec welding speed (v). Indeed, throughout the course of this work, in excess of 300 individual laser welds were conducted and analysed. While only burst frequencies below 200 Hz were of concern to this particular investigation, some higher frequency results have been included at the end of the chapter for completeness.

All welds in this study used Ipsco X-70 micro-alloy, arctic pipeline steel 1.6 cm in cross-section, as the base metal. Weld coupons approximately 3.8 x 7.6 cm were prepared for welding by sandblasting and degreasing the top surface. Each sample was used for two

individual welds by allowing sufficient time in-between passes for the substrate to return to room temperature.

Translation of the substrate was accomplished with a computer controlled X-Y table interfaced with a Motorola 68000 based computer system⁵⁰. Accurate control of sample placement and welding speed were easily achieved with this system. Power monitoring was performed with a spinning-cone calorimeter⁴⁹. For the welds in these experiments, the laser focus location was 0.4 mm below the substrate surface. Plasma suppression gas flow was held constant at a level consistent with that used in CW welding.

Beam delivery to the material surface was accomplished via a standard welding head configuration consisting of aluminium reflective optics. The annular beam from the laser was redirected with a skimmer to a second mirror which then focused it down through the skimmer hole. The welding head optic $f^\#$, defined as (4.1), was approximately 10.

$$f^\# = \frac{f}{D} \quad (4.1)$$

Here, f is the focal length of the focusing mirror and D is the clear aperture or diameter of the incident laser beam. Figure A.2 is a photograph of the complete laser welding head assembly.

The welding nozzle utilized a single Helium plasma suppression jet oriented towards the front of the keyhole and an Argon trail gas curtain. Accurate location of the plasma suppression jet was accomplished using a HeNe laser and manometer arrangement

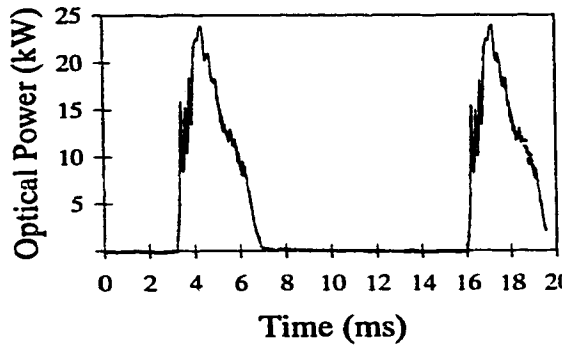
as described by Arata⁴.

A previous study using a carbon powder based beam visualization technique indicated that the laser focal spot size was on the order of $1 \text{ mm} \pm 0.1 \text{ mm}$ ⁵¹. Thermal lensing effects in the output window were found to be negligible at the power levels considered in this study.

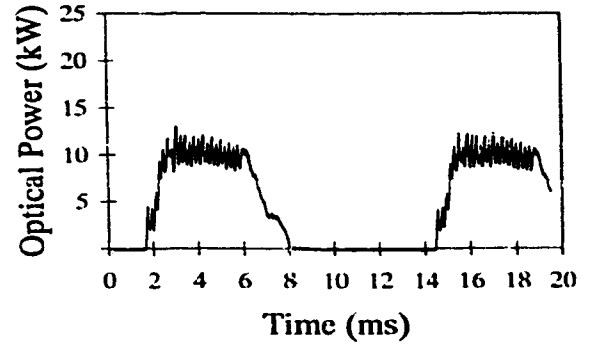
4.2 Weld Trends

Weld penetration was consistent over the range of parameters examined. A representative sample is provided to demonstrate trends. In general, 4kW data was found to be representative of the results at each power level. The distinct-pulse regime is bounded by a minimum f_b of 75 Hz and maximum of 172 Hz. For purposes of this chapter, weld macro-photographs are given for $N = 7$ and $D_b = 40\%$ at burst frequencies of 75, 125 and 172 Hz. The $N = 7$ case represents small N and was included at each burst frequency sampled. Furthermore, $N = 7$ depicts a relatively low D_b at each f_b considered here. A $D_b = 40\%$ case was chosen to illustrate large N and the high end of D_b sampled. Optical waveforms associated with these excitation conditions are provided in Figure 4.1 for reference in this chapter.

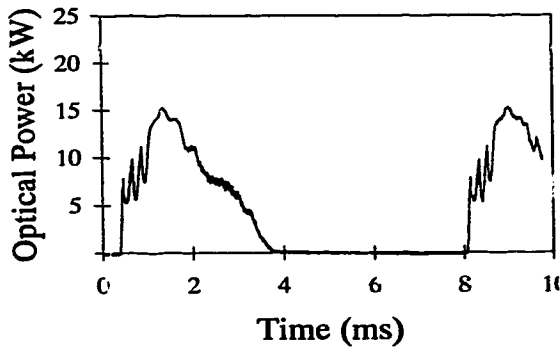
Since the primary focus of this investigation was weld penetration, optimization of other welding parameters was not attempted. Therefore, weld bead quality, microstructure and other parameters associated with a complete welding specification were beyond the scope of this thesis. Welds with imperfections are included in the following discussion in order to fully characterize trade-offs and limitations associated with using burst excitation



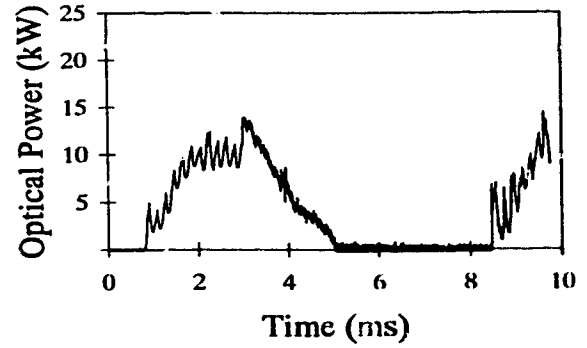
(A)



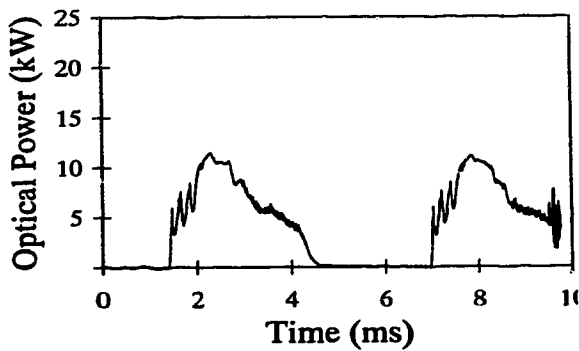
(B)



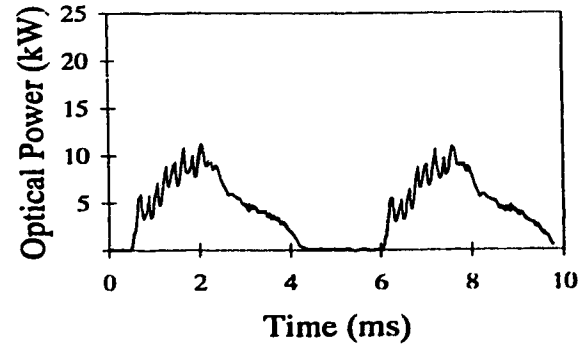
(C)



(D)



(E)



(F)

Figure 4.1: 4 kW average power pulse profiles applied to welding in this section;
 (A) $f_b=75$ Hz, $N=7$, (B) $f_b=75$ Hz, $N=27$, $D_b=40\%$, (C) $f_b=125$ Hz,
 $N=7$, (D) $f_b=125$ Hz, $N=16$, $D_b=40\%$, (E) $f_b=172$ Hz, $N=7$, (F) $f_b=172$
 Hz, $N=12$, $D_b=40\%$,

in practical deep penetration welding. Unless otherwise noted, macro-photographs were taken at a magnification of 4.7x.

Figures 4.2 through 4.8 represent burst and CW bead-on-plate welds performed at

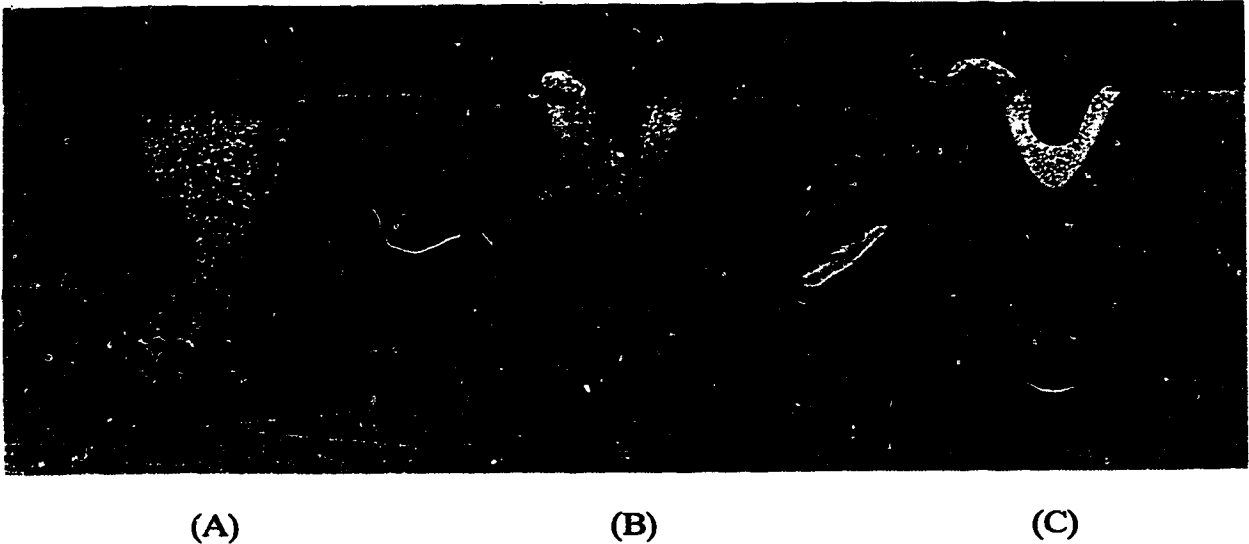


Figure 4.2: 4 kW Burst welds performed at $f_b=75$ Hz, $N=7$; (A) 8 mm/sec., (B) 12 mm/sec., (C) 16 mm/sec. 4.7x Magnification.

4 kW average laser power. The following macro-photographs are presented to demonstrate burst excitation weld trends with respect to burst frequency, number of pulses per burst, burst duty cycle and welding speed. Each of the figures in this section has three parts (a) through (c) which represent 8, 12 and 16 mm/sec. welds, respectively.

Figure 4.2 presents results for $f_b = 75$ Hz and $N = 7$ at 8, 12 and 16 mm/sec. With P_{av} and P_p fixed, decreasing penetration with increasing process speed was expected. Welding speed dictates the rate at which energy is deposited into the substrate. Therefore, less energy is deposited per cm^2 at higher processing rates. At low f_b and small N , P_p is

large, as much as 6 times the CW level as illustrated in Figure 4.1(A). A typical weld under these conditions is shown in Figure 4.2(A)

A significant lack of material is found at both root and cap in Figure 4.2(B). The cause of this weld defect can be understood as follows. To maintain a stable keyhole at low f_b , considerable pulse overlap is necessary to maintain the incident energy density required on the weld substrate. With increasing processing rate, less energy is deposited, resulting in keyhole instability. Sudden collapse of the keyhole leads to entrapment of gas or chill voids, as indicated at the root of Figure 4.2(B). At these pulse frequencies and processing rates, complete solidification of the molten metal is unlikely to occur in between pulses. This, coupled with an unstable keyhole can lead to violent expulsions of molten material with each subsequent pulse event. Thus, at increasing welding speeds and low f_b , large quantities of material are ejected from the keyhole region, leading to severe top-bead indentations. This feature is evident in Figure 4.2(C).

Another potential source of keyhole instability, which likely compounds this problem, was introduced in Chapter 3. Waveform recording required averaging of signals due to vibrational modulation of the optical output. Here, consistency and repeatability of the optical trends verified that such modulation was not related to discharge excitation. However, while welding there was no effective means of averaging the optical output of the laser. Control of ν provided the only method of averaging energy deposition, through pulse overlap. As discussed, this modulation led to an inconsistency in peak power. This inconsistency was most pronounced at low f_b and small N , where peak optical power was extremely high but pulse duration short.

With increasing N , peak power was reduced dramatically, as indicated in Figure 4.1(B). Greater pulse stability associated with a longer pumping cycle and lower P_p provided more consistent processing, as shown in Figure 4.3. Here, f_b remained at 75 Hz and

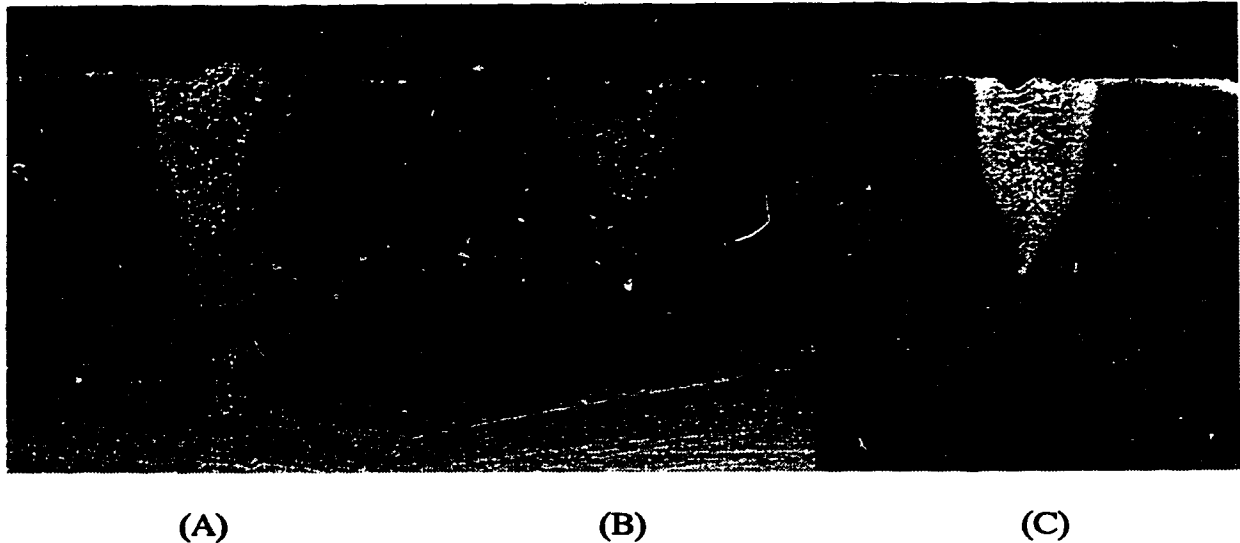


Figure 4.3: 4 kW Burst welds performed at $f_b=75$ Hz, $N=27$; (A) 8 mm/sec., (B) 12 mm/sec., (C) 16 mm/sec. 4.7x Magnification.

N has been increased to 27. Penetration in Figure 4.3 decreases with increasing v as found in the $N = 7$ case. Under these conditions, top bead profiles still indicate a slight lack of material, shown at the weld caps in Figure 4.3(B) and (C). Since weld coupons were cut from 60 cm diameter pipe, their overall cross section was not perfectly rectangular. As a result, mounting the sample surface perpendicular to the laser beam axis was not always possible. This explains the slight angle present in some welds.

Increasing f_b to the mid-range of the distinct pulse regime resulted in welds which were consistent with those discussed above. At $f_b = 125$ Hz and $N = 7$, Figure 4.1(C), P_p is

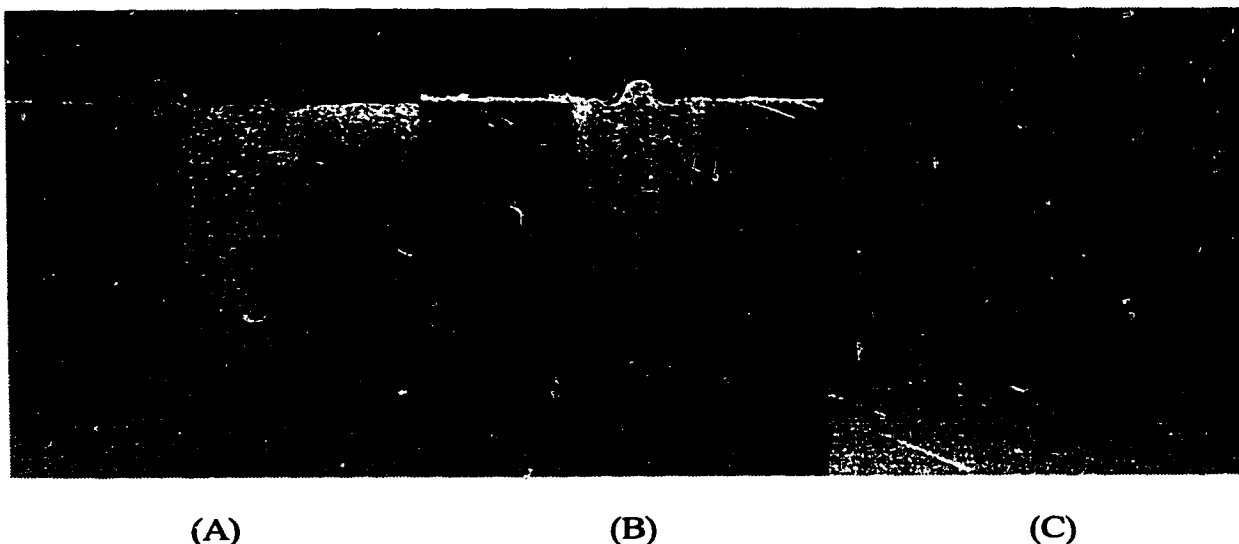


Figure 4.4: 4 kW Burst welds performed at $f_b=125$ Hz, $N=7$; (A) 8 mm/sec., (B) 12 mm/sec., (C) 16 mm/sec. 4.7x Magnification.

on the order of 15 kW. Penetration under these conditions decreased with increasing v , as illustrated in Figure 4.4. Keyhole instability defects associated with high process speeds were less pronounced at 125 Hz, but still observable at $v = 16$ mm/sec., Figure 4.4(C).

Holding f_b at 125 Hz and increasing N to 16 corresponded to a decrease in P_p and increase in pulse width, as in Figure 4.1(D). Under these conditions, penetration also decreases with increasing v . Figure 4.5 illustrates that increasing N to 16 resulted in improved weld quality. Here, weld cap profiles are more uniform when compared to the $N = 7$ case in Figure 4.4. Thus, under $f_b = 125$ Hz and $N = 16$ excitation, a stable keyhole produced good weld profiles at process rates up to 16 mm/sec.

A further increase in f_b to 172 Hz is characterized by a simultaneous decrease in P_p depicted in Figure 4.1(E) and (F). Reduction in P_p resulted in a similar decrease in penetration when compared to the lower frequency cases presented above. At $f_b = 172$ Hz and

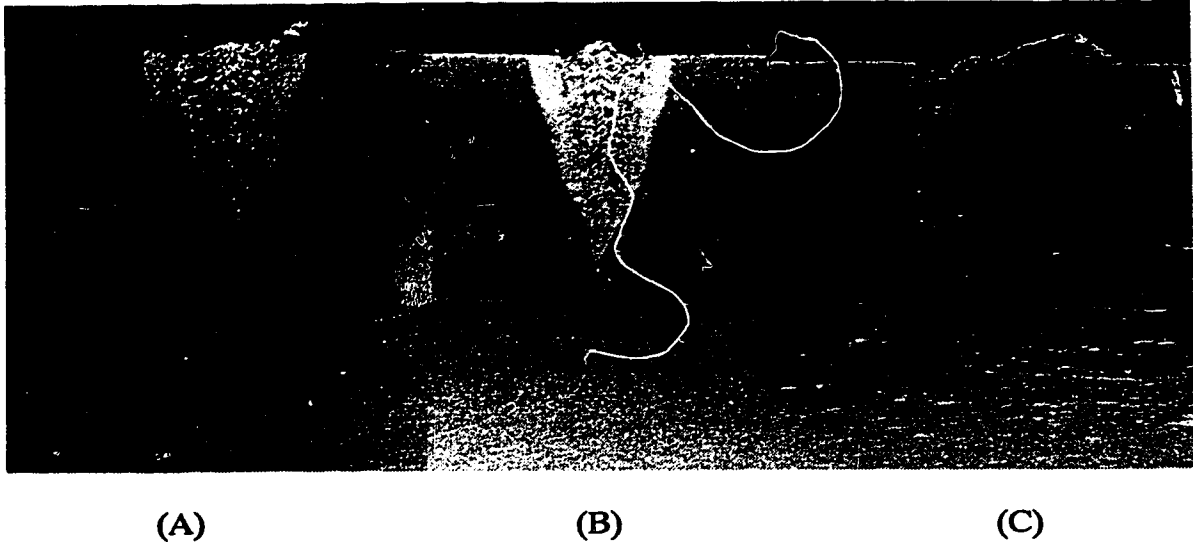


Figure 4.5: 4 kW Burst welds performed at $f_b=125$ Hz, $N=16$; (A) 8 mm/sec., (B) 12 mm/sec., (C) 16 mm/sec. 4.7x Magnification.

$N = 7$, Figure 4.5, a decrease in penetration with increasing v is evident. Operation at this

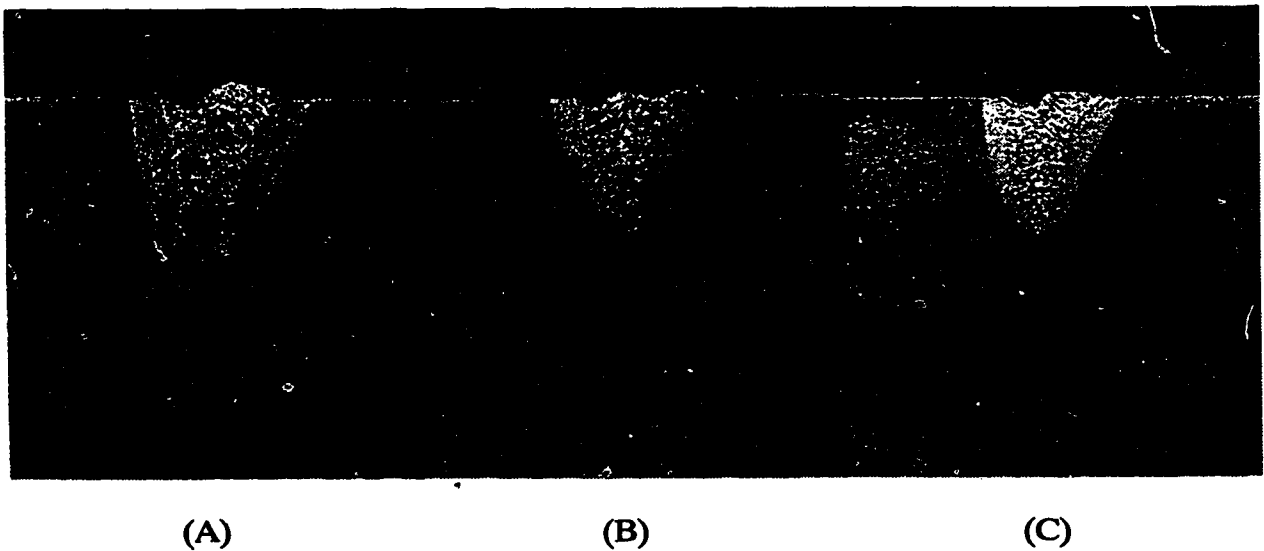


Figure 4.6: 4 kW Burst welds performed at $f_b=172$ Hz, $N=7$; (A) 8 mm/sec., (B) 12 mm/sec., (C) 16 mm/sec. 4.7x Magnification.

higher f_b produced improved crown profiles when compared to the $f_b = 75$ Hz case in Figure 4.2. Study of Figure 4.6 indicates a slight increase in weld crown width at this frequency. This observation can be understood as follows. As f_b was increased for a given N , the duration between subsequent pulses decreased. As a result, plasma radiation effects at the weld crown were significant. Details of this plasma interaction with the weld crown are discussed in the following sections.

Figure 4.7 illustrates welding results for $f_b = 172$ Hz with N increased to 12. The

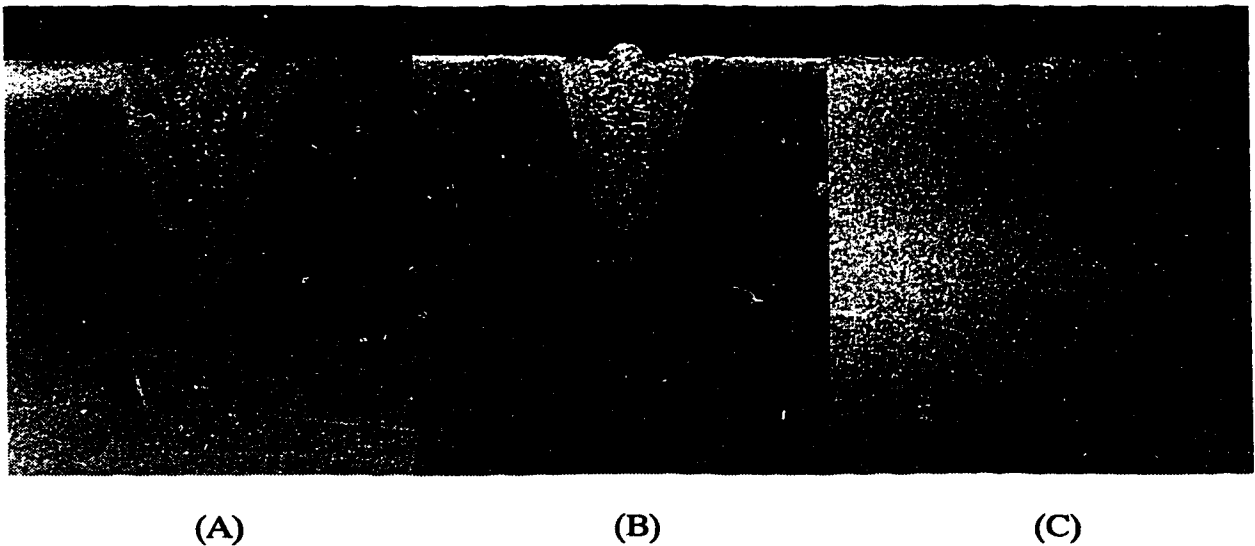


Figure 4.7: 4 kW Burst welds performed at $f_b=172$ Hz, $N=12$; (A) 8 mm/sec., (B) 12 mm/sec., (C) 16 mm/sec. 4.7x Magnification.

optical waveform corresponding to this excitation is provided in Figure 4.1(F). Figure 4.7 illustrates decreasing penetration with increasing v as well as improved crown profile when compared to Figure 4.2.

For comparison, Figure 4.8(A) through (C) present welds performed under CW

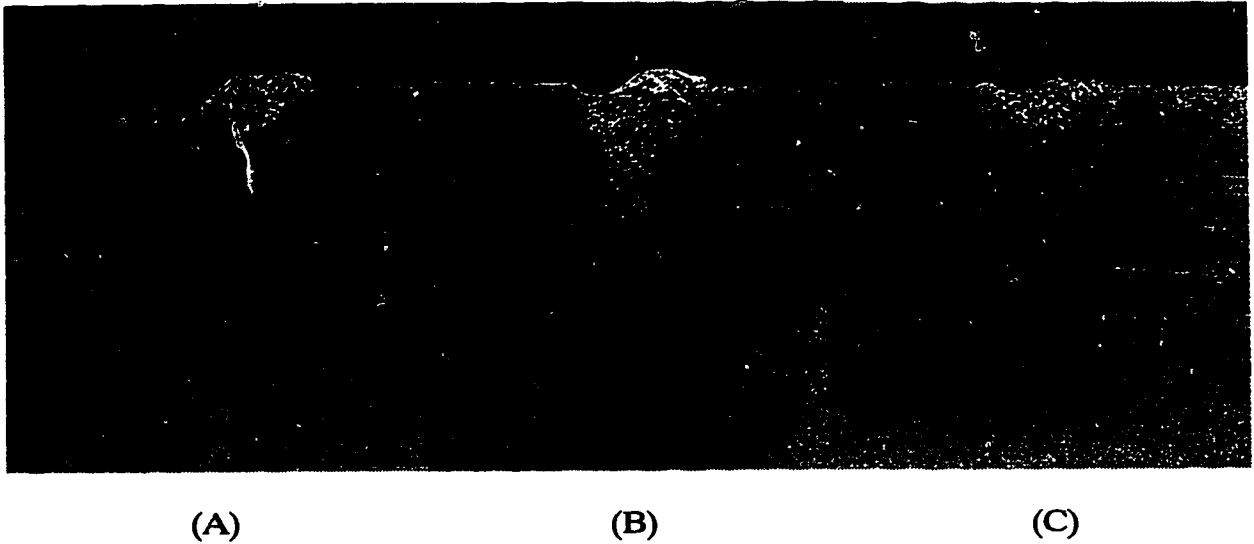


Figure 4.8: CW welds performed at; (A) 8 mm/sec., (B) 12 mm/sec., (C) 16 mm/sec. 4.7x Magnification.

conditions at 8, 12 and 16 mm/sec. Distortion of the top bead profile, evident in this figure, was attributed to a slight misalignment of the plasma suppression jet. This effect was most apparent at low v since the plasma suppression flow rate was fixed, in this study, at a level consistent with higher processing rates. Comparison with other CW welds indicated no significant difference in weld penetration. As such, weld penetration achieved under CW conditions here was consistent with results presented elsewhere^{52,53,54}.

The proceeding figures have demonstrated a number of trends with burst excitation. In general, as P_p decreased with increasing f_b , penetration decreased proportionately. For fixed average and peak laser power, weld penetration was found to decrease with increasing v . This trend was found to be independent of f_b and N . High peak powers associated with low f_b excitation resulted in excellent penetration performance. However, key-hole instability, resulting from optical output modulation, limited maximum processing

rate. Increasing N for a given f_b resulted in increased keyhole stability. The following sections will summarize the processing trends observed, in order to gain a better understanding of system performance.

4.2.1 Weld Penetration and Burst Frequency

As mentioned previously, P_p and P_{av} are significant factors in determining the maximum penetration achievable in a welding sequence. Figure 3.10 demonstrates that under burst mode excitation, peak laser power is inversely proportional to f_b , as it approaches CW operation. Based on this fact, a similar trend in weld penetration at a given average power level is expected. The preceding section presented 4 kW data as representative of the overall results observed. This section will present a graphical summary of weld penetration with respect to all power levels considered.

Figures 4.9 through 4.11 illustrate burst weld penetration as a function of f_b for fixed N and v . Figure 4.9 clearly illustrates the trend of decreasing weld penetration with increasing f_b . Decreasing P_p through increasing f_b results in a corresponding decrease in penetration. Here, agreement is best in the 8 mm/sec. case. At 12 mm/sec., Figure 4.10, the trend is still observable but less pronounced. Finally, at 16 mm/sec. data scatter results in a less defined trend, as shown in Figure 4.11. Overall, penetration was found to be inversely proportional to burst frequency. The increase in uncertainty at higher welding speeds was likely caused by two factors. As discussed above, an unstable keyhole resulted in violent expulsion of material from the weld region. This effect would lead to inconsistencies in penetration. Further, some uncertainty is also likely the result of vibration of the optical resonator leading to an inconsistency in peak power between pulses. Since v relates

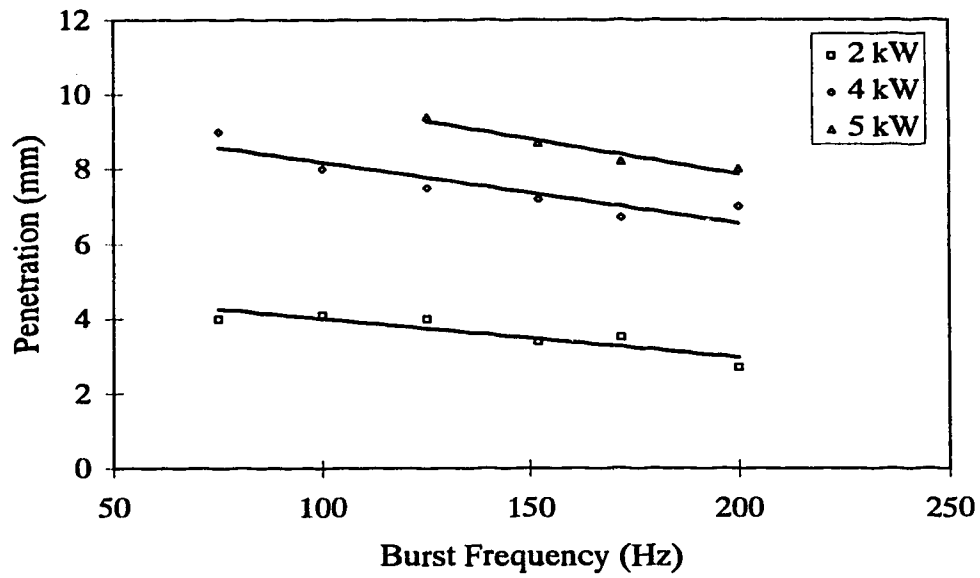


Figure 4.9: Weld penetration with respect to burst frequency at $N = 7$ and $v = 8$ mm/sec.

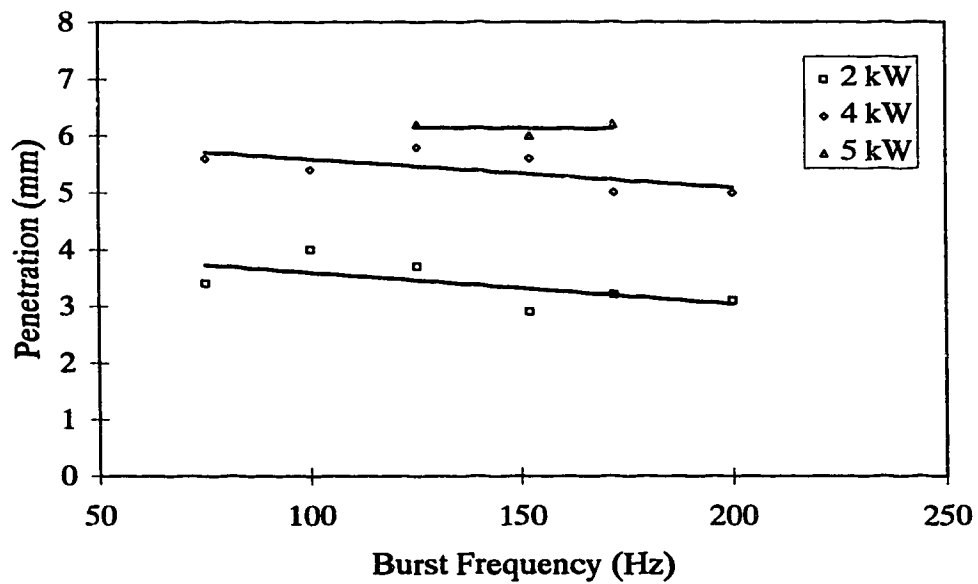


Figure 4.10: Weld penetration with respect to burst frequency at $N = 7$ and $v = 12$ mm/sec.

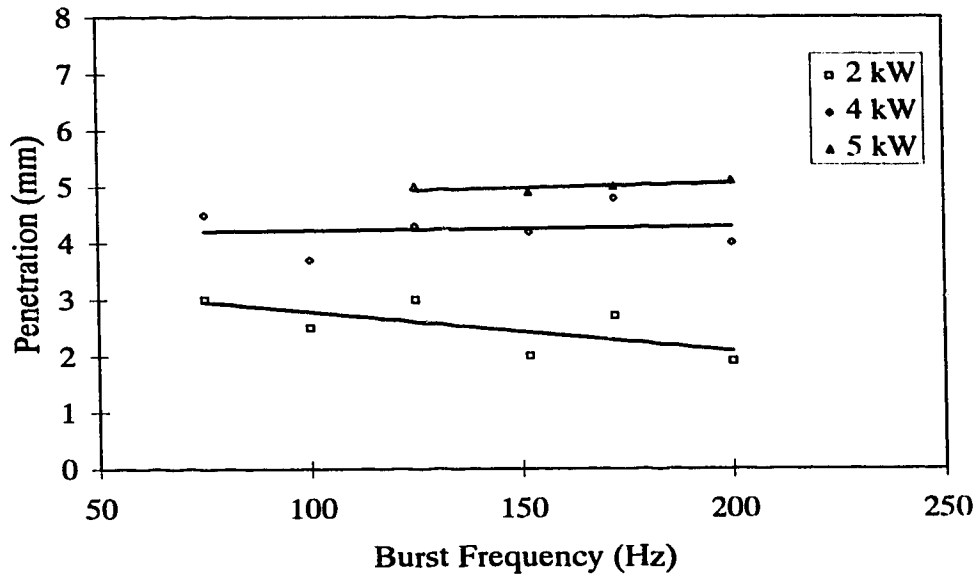


Figure 4.11: Weld penetration with respect to burst frequency at $N = 7$ and $v = 16$ mm/sec.

to overlap of optical pulses for a given f_b , increasing v results in less pulse overlap and therefore more variation in the mean weld penetration.

As discussed in Chapter 3, the maximum power output from the laser under the conditions of this research was 6 kW. However, subsequent to the collection of optical data, it was determined that 6 kW output at some low f_b and N combinations could not be consistently achieved without reaching the voltage limit of the power supply. As a result, welds were performed at these and all other points at $P_{av} = 5$ kW for ease of presenting the results. Results provided in these figures illustrate that the 5 kW data was consistent with the trends observed at 6 kW with only a proportional drop in penetration.

While there is some uncertainty in results at higher welding speed, the data is still

consistent with predictions. With average power and welding speed held constant, weld penetration is found to drop with increasing burst frequency.

4.2.2 Weld Penetration and Welding Speed.

A distinct advantage observed with this particular PIE laser system is the enhanced penetration associated with operation within the pulse-periodic excitation regime. As mentioned, weld speed dictates the rate at which energy is deposited. Thus, penetration is expected to decrease with increasing v with all other parameters held constant.

Figures 4.12 through 4.14 present a comparison of CW and burst weld penetration

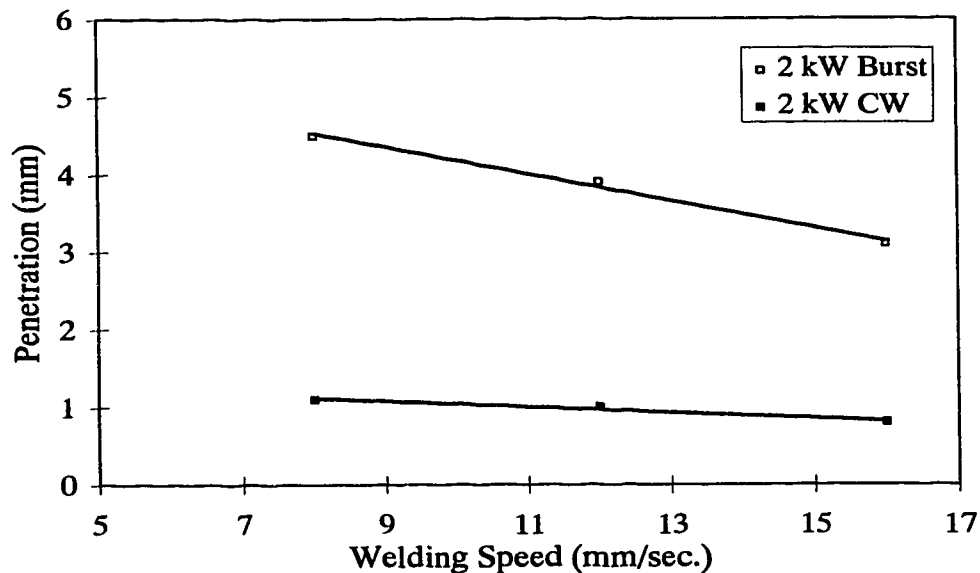


Figure 4.12: Weld penetration with respect to weld speed at $P_{av} = 2$ kW.

with respect to welding speed at a given average power. Here, maximum burst and CW

penetration are well contrasted. Figure 4.12 demonstrates that at 2 kW, both CW and burst penetration decreases with increasing welding speed. Figures 4.13 and 4.14 illustrate this

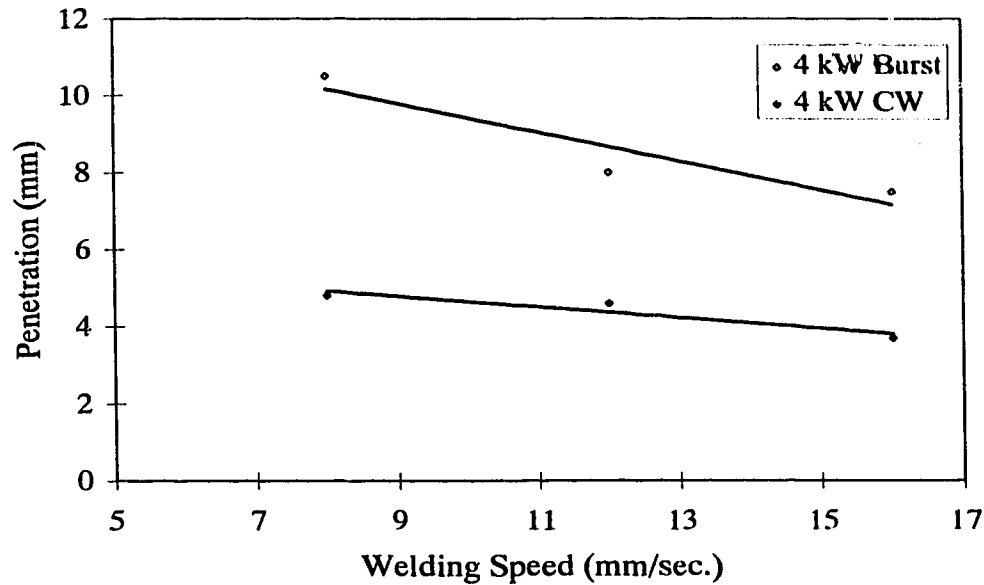


Figure 4.13: Weld penetration with respect to weld speed at $P_{av} = 4$ kW.

same general trend for 4 and 6 kW, respectively.

The difference between burst and CW penetration, at each power level in Figures 4.12 through 4.14 is inversely proportional to the average laser power. This aspect is discussed in the following section.

4.2.3 Comparison of CW and Burst Penetration Performance

Figure 4.15 is a plot of the percentage increase found in weld penetration between burst and CW operation as a function of v , at the extremes of the power levels considered

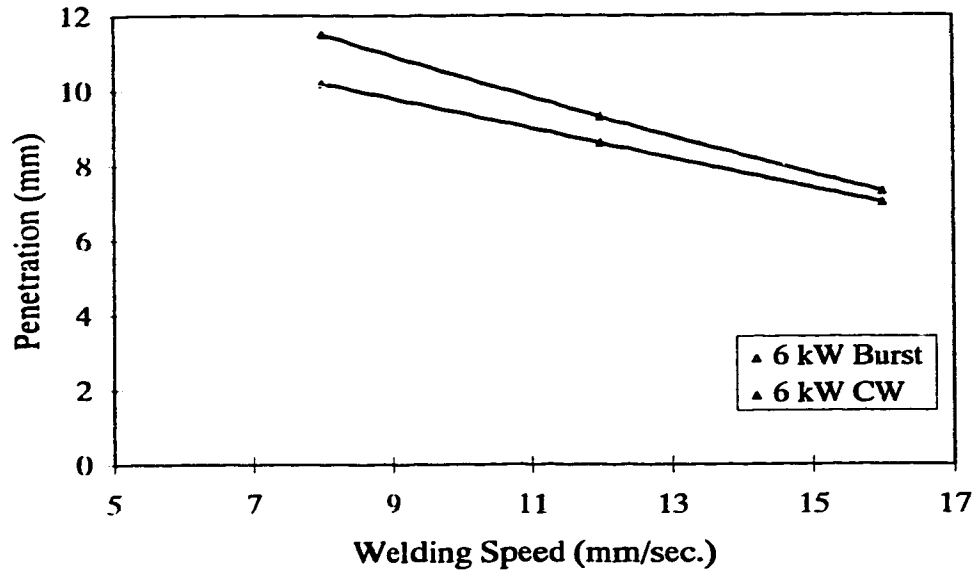


Figure 4.14: Weld penetration with respect to weld speed at $P_{av} = 6$ kW.

in this study. Burst data presented in Figure 4.15 represent the maximum weld penetration at low f_b for a given v . Equation (4.2) illustrates the calculation of %CW Penetration. This trend is consistent over the entire range of power levels examined to date.

$$\%CW \text{ Penetration} = \frac{\text{Burst Penetration}}{\text{CW Penetration}} \cdot 100\% \quad (4.2)$$

A dramatic enhancement in penetration is indicated in Figure 4.15. Burst weld penetration at $P_{av} = 2$ kW is found to be approximately 400% greater than under CW conditions at the same average power level. However, at $P_{av} = 6$ kW the difference is found to be smaller. Figure 4.15 can be understood in the following discussion. At 2 kW, power density in the incident CW beam is below threshold for keyhole formation. Conversely, the peak power within the burst beam, at the same average power level is approximately

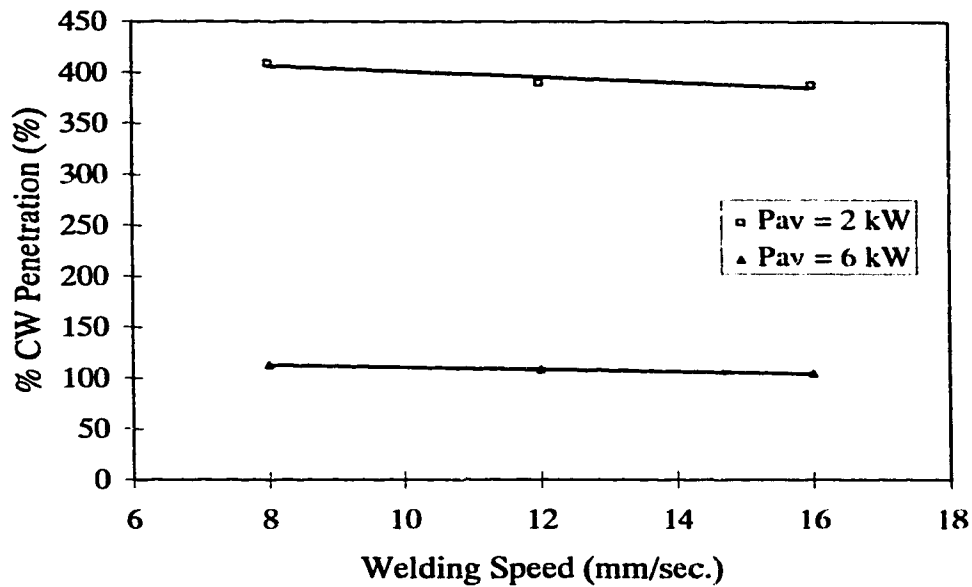


Figure 4.15: Penetration performance difference between Burst and CW welds with respect to welding speed.

12 kW. Thus, at 2 kW a significant penetration improvement under burst mode operation is achieved as a result of the increased peak laser power. When the average power level is increased to 6 kW, a different situation develops. With increasing power, CW penetration approaches that of burst mode. As the energy present in the CW beam increases, formation of a stable keyhole is possible. Thus, laser energy can now be transferred into the bulk of the material. At lower processing rates, burst mode still outperforms CW operation since the overlap of high intensity impinging pulses results in more energy deposition per unit area.

At higher average power levels, CW penetration is seen to approach that of burst mode. However, the quality of the weld profile is found to deteriorate in the CW case. Figure 4.16(A) is a typical macro photograph of a CW weld performed at $P_{av} = 6 \text{ kW}$, $v = 8$

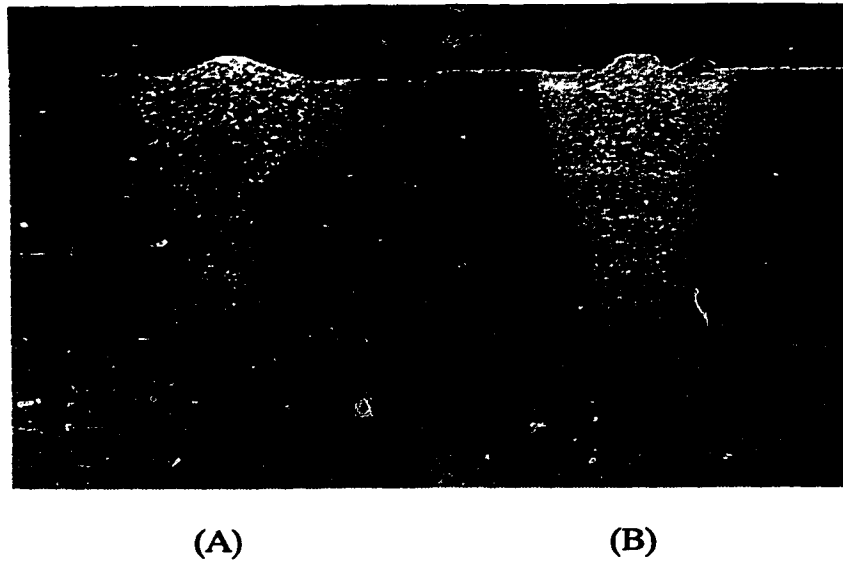


Figure 4.16: 6 kW laser welds, $v = 8\text{mm/sec.}$; (A) CW weld, (B) burst weld with $f_b = 75$ and $N = 13$. Magnification = 4.7x.

mm/s. A burst mode weld performed at the same average power and speed with $f_b = 75\text{ Hz}$ and $N = 15$ is presented in Figure 4.16(B).

In Figure 4.16(B), weld profile is seen to be extremely narrow, a characteristic of the burst excitation process. For a given processing rate, as the laser power increases, a greater proportion of the energy is absorbed in the metal vapour plasma formed at the top of the keyhole. This plasma is known to radiate energy in all directions. Of particular interest here is the energy radiated into the side-walls of the keyhole. With increasing power, the crown of the CW weld grows wider as a result of radiation from the plasma, Figure 4.16(A). This process ultimately results in an inferior weld profile, since a large portion of the surrounding base material becomes affected.

As discussed previously, with pulsed operation, sufficient time is available for the metal vapour plasma to extinguish in-between pulses. Consequently, weld profiles

become extremely narrow, Figure 4.16(B), with a minimum of surrounding material modification. The intermittent metal vapour plasma, produced during a burst excitation, reduces plasma suppression gas requirements. This aspect could be a major benefit in continuous production environments since it can significantly impact processing costs.

4.2.4 Extension to High Average Power Levels

This parametric study was limited to maximum power levels of 5 to 6 kW in order to observe the entire range of f_b . As discussed in Chapter 3, this was the result of voltage limitations in the DC pumping supply. Operation of this PIE system at higher average laser powers was possible with a concomitant decrease in the low f_b operating range. Indeed, welding results are equally dramatic with this technique at increasing average power levels.

In general, at power levels exceeding 6 kW, burst operation is limited to minimum burst frequencies on the order of 200 Hz with the current DC supply. As demonstrated in Chapter 3, the transition from the distinct pulse regime occurs at approximately this frequency. Thus, the higher power results were in general beyond the scope of this work.

Figure 4.17 represents a $P_{av} = 9$ kW, CW weld performed at $v = 7$ mm/sec. The extremely wide weld profile is consistent with a CW weld performed at a relatively slow processing rate. This figure represents an extension of the discussion associated with Figure 4.16(A). Figure 4.18 illustrates a burst mode weld at $P_{av} = 9$ kW, $f_b = 200$ Hz and $N = 7$. This figure illustrates the dramatic performance of this burst technique. Side-wall profile is extremely narrow and penetration is on the order of 18 mm.

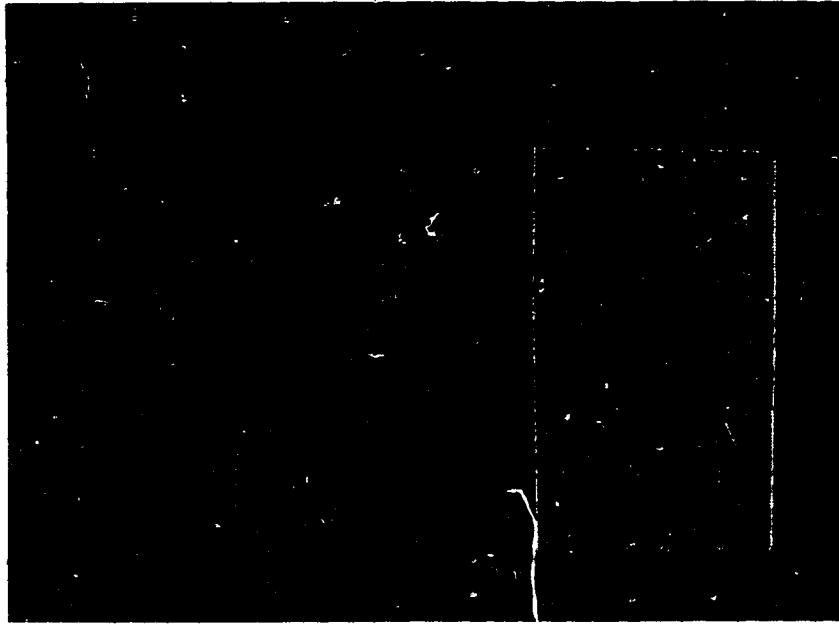


Figure 4.17: CW weld micrograph, $P_{av} = 9 \text{ kW}$, $v = 7 \text{ mm/sec}$.

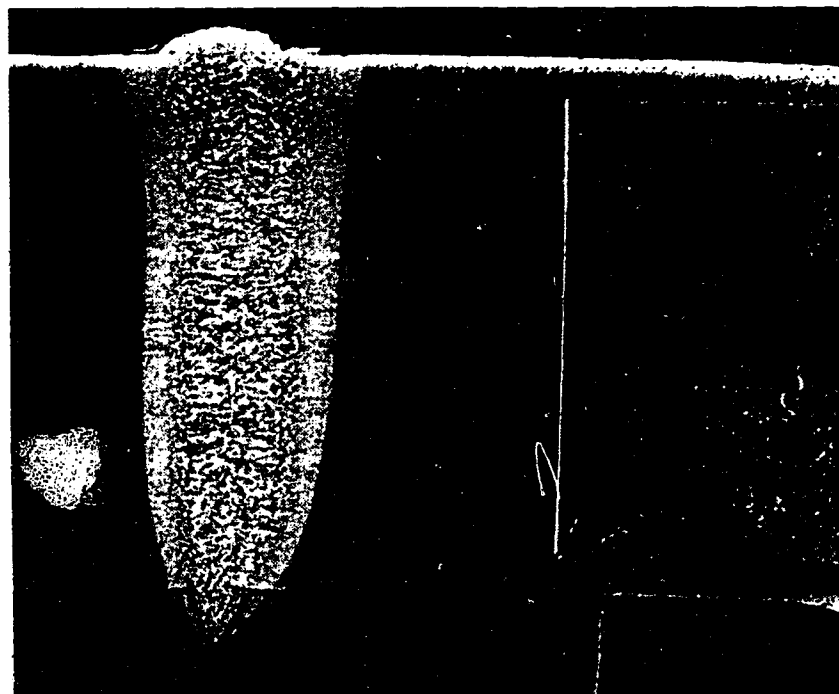


Figure 4.18: Burst weld micrograph, $P_{av} = 9 \text{ kW}$, $f_b = 200 \text{ Hz}$, $N = 7$, $v = 7 \text{ mm/sec}$.

4.3 Discussion

As a result of the low frequency modulation of the optical signal, strict application and testing of the empirical relationships developed in Chapter 3 was not possible. These relationships were based on a consistent pulse signal as a result of oscilloscope averaging. It would be necessary to apply a consistent optical signal to the weld region in order to use these expressions. Elimination of the optical modulation would require major modifications of the laser system which is beyond the scope and time frame of this thesis.

These weld results demonstrate the significance of the burst excitation technique. With this process, laser penetration enhancement on the order of 400% has been achieved. This and the dramatic results at higher average power levels indicate the potential of future study.

Chapter 5

Conclusions and Proposals for Future Research

5.1 Summary of this Investigation

Results presented in this thesis have demonstrated the viability of a unique burst excitation technique for deep penetration CO₂ laser welding applications.

Characterization of the optical aspects of this process required design and development of a wide range of systems and apparatus. An understanding of the technique was gained through observation of the laser discharge current behaviour. In order to observe the discharge parameters, a high precision, optically isolated, current monitoring system was implemented. Performance of this system was shown to exceed the requirements of the application.

Similarly, observation of the optical signals associated with burst excitation required development of an optical monitoring system. The broad-band frequency content of the optical signal precluded use of rotational sampling as a means of data collection. Thus, a real time beam attenuation system was required. A series of reflecting and transmissive optics were utilized to reduce the average laser power by 6 orders of magnitude. At this reduced average power level, a photo-electromagnetic detector was well suited to pulsed radiation with significant average and peak power levels. However, thermal generation of charge carriers was found to introduce a continuous signal offset in the detector. An algorithm was developed, tested and implemented to correct for this offset. A high

speed, low noise amplifier was designed as interface between the optical detector and a digital storage oscilloscope. Performance of this amplifier was also found to exceed the requirements of the signals collected.

Acquisition of optical and current data was accomplished through development of a C based program interfacing the user and a digital storage oscilloscope. Manipulation of the data for thermal offset correction and postscript output was accomplished with a series of UNIX based scripts.

Optical data was collected at 2, 4 and 6 kW average laser power levels. The range of power levels sampled was limited by DC pumping supply limitations. Variation of the excitation burst frequency and number of pulses per burst yielded a wide range of optical pulse characteristics. A consistent trend in peak power, pulse width and pulse shape was demonstrated over the full range of power levels investigated. Consequently, the 4 kW data was used as a representative data set for subsequent calculations.

Optical and current waveforms were collected over the practical operating range of this laser system. The minimum burst frequency available over the range of power levels considered was 75 Hz. Data was collected from this point up to CW. Operation of the system was observed at burst duty cycles of 10, 20 and 40%. This range represented optical output ranging from extremely short pulse duration at each frequency to the limit of pulse overlap.

A significant low frequency modulation of the optical output was attributed to lack of vibrational isolation of the cavity optics. Thus, averaging of the optical waveforms was

necessary to observe trends. The overall consistency and trends spanning all power levels was reasonable justification for this averaging.

A direct correlation between the discharge current and optical output was discovered. Low burst frequency and small N excitation was characterized by peak powers up to 6 times the CW level. Laser pulses had a predominantly triangular shape and laser power fell to zero in between pulses. This operational mode was referred to as the distinct-pulse regime. At low burst frequency and large N , a discharge equilibrium is eventually reached where electron creation is balanced by electron loss. Here, the optical waveform peak power saturates and the pulses assume a square or rectangular profile. DC supply components were found to have a significant influence on the characteristics of the current waveforms.

At increasing burst frequencies, discharge conductivity was found to have insufficient time to decay to zero in between pulses. As a result, a constant optical power level was maintained. Ultimately, current and optical characteristics approached CW conditions as burst frequency was further increased. The distinct pulse regime was chosen as the primary focus of this thesis investigation.

Consistency of the optical trends observed, over the range of power levels in question, prompted investigation of the relationships between the primary excitation parameters. It was suggested that peak power, pulse duration, average power and pulse shape would ultimately effect the characteristics of pulsed laser welds. In order to implement such a technique in an industrial environment, it was necessary to have a means to predict the optical characteristics when designing a welding specification.

Two empirical expressions were developed relating the excitation burst frequency, number of pulses and average power to the optical energy per pulse, peak power and optical duty cycle. These expressions were found, through a number of test cases, to predict the parameters in question with reasonable certainty.

Burst excitation laser welding was found to offer a number of advantages over CW operation. Laser penetration at a given average power level and processing speed was consistently greater with this process. Laser peak power was found to decrease with increasing burst frequency. Thus, for a given average laser power and processing rate, laser penetration was also found to decrease with increasing burst frequency. Similarly, weld penetration was found to decrease with increasing welding speed for a given burst frequency. This was expected since welding speed dictates the rate at which energy is deposited at the material surface.

Welding speed was also found to have a direct effect on the overall final weld profile. In CW welding, a large steady state plasma was present at the top of the laser keyhole. For a fixed processing rate and increasing power, the plasma radiated energy into the side walls of the weld. Thus, CW welds were characterized by a relatively wide weld crown. Conversely, with burst welding, sufficient time existed in between pulses for the metal vapour plasma to extinguish. As a result, burst welds had a more narrow parallel side wall profile when compared to CW welds at the same power level. Further, a potential reduction in the plasma suppression requirement is possible as a result of the intermittent nature of the plasma. Helium is the most common gas used for plasma suppression and represents a significant portion of CW laser operating costs.

Burst welding was found to provide significant advantages over CW at low average power levels. Here, insufficient power existed in the CW beam to provide the necessary energy density for stable keyhole formation. Burst welding at the same average power levels was characterized by peak powers many times the CW level. Thus, sufficient energy density was present to form a stable keyhole. As the average powers increased, CW performance was found to approach that of burst welding. Overall, the burst process was still capable of greater penetration since the peak powers were still many times greater than the average level.

Some inconsistencies and instabilities were attributed to modulation of the optical waveform. While the oscilloscope was able to average successive pulses to indicate overall trends, the only means of averaging while welding was lowering the processing rate. Thus, under low burst frequency conditions, where peak optical power modulation was most apparent, high processing speed resulted in poor quality welds.

5.2 Proposals for Future Research

The interesting results of this research warrant further investigation of a number of aspects of this laser excitation technique. This section will briefly outline some potential areas of exploration.

A study should be performed to conclusively identify the source of the vibrational modulation of the optical output. Likely, a solution will be found in better isolation of the optical bench from the laser enclosure. At present, the blower assembly is rigidly mounted to the laser structure. Isolating the blowers from the entire structure may further limit the

vibration affecting the optical bench.

One primary limitation in this study was the lack of DC supply voltage to fully characterize the burst excitation performance over the entire operating range of the laser. An increase in the voltage output is attainable through a number of means. A preliminary investigation suggested that connecting the central point of the Y-secondary of the supply transformer to the reference point or ground of the DC supply would result in increased output voltage potential. A second approach would involve replacing the transformer with a higher voltage unit. Both of these solutions would require careful attention to the maximum voltage ratings of the various devices contained within the supply.

As discussed previously, the current behaviour of the discharge is defined primarily by the massive inductors located between the supply and the discharge. These inductors are present to limit the current rise associated with a potential arc in the discharge. Such an arc could lead to catastrophic failure of the multi-element pin electrode structure. Since the optical pulse characteristics depend so heavily on the current characteristics, it follows that the full potential of the optical performance was limited by these arc prevention inductors. Addition of relatively small ‘peaking’ capacitors after the large inductors could provide increased flexibility in the optical signals. These capacitors could be chosen such that they could store ample energy for a pulse event at a given frequency, but their stored energy would still be limited to a level which could not cause damage to the electrode structure. This additional current capacity could serve to further enhance the optical output under burst excitation.

Further study of the optical output of the laser is warranted by some of the discrep-

ancy associated with the empirical relationships developed. Preliminary results indicated that the shape factor associated with the number of pulses per burst may be a necessary component of a fully developed empirical relationship between all the process parameters. This study should likely not be undertaken until the optical modulation can be eliminated.

Despite the variation in optical output, the welding results presented here demonstrate the potential of this process. Extension of this work to higher power levels could potentially produce dramatic deep penetration welding results at relatively common average power levels. Ultimately, this may represent a technique that could reduce the size and complexity of a CO₂ laser necessary to achieve a given weld penetration.

A significant reduction in the plasma suppression requirement, through burst operation, could dramatically reduce the operating costs of a laser welding process. A study could be conducted utilizing a simple optical detector to determine the optimum plasma suppression requirement under burst excitation conditions. Mounted near the top of the keyhole, the detector could monitor the light emissions from the vapour plasma ball. Using this technique, plasma suppression flow rate could be optimized for a given pulsing condition.

References

- 1 C.K.N. Patel, "Interpretation of CO₂ Optical Maser Experiments," Phys. Rev. Lett., 12, 588 (1964).
- 2 G. Chryssolouris, "Laser Machining - Theory and Practice," Mechanical Engineering Series, (Springer-Verlag, New York, 1991).
- 3 W.J. Witteman, "The CO₂ Laser," Springer Series in Optical Sciences, 53, (Springer-Verlag, Berlin, 1987)
- 4 Y. Arata, "Plasma, Electron and Laser Beam Technology," (American Society of Metals, Metals Park, Ohio, 1986).
- 5 V.E. Merchant, M.R. Cervenak and H.J.J. Seguin, "An Industrial Quality 20 kW Infrared Laser," Proc. International Conference on Lasers '85, 642-646 (1985)
- 6 The Laser's Edge, United Technologies Industrial Lasers Newsletter, March, (1992).
- 7 E.F. Yelden, H.J.J. Seguin, C.E. Capjack and S.K. Nikumb, "A Multi-channel Slot Discharge CO₂ Laser Employing a Toric Unstable Resonator," Opt. Commun. 82, 503, (1991).
- 8 W.D. Bilida, J.D. Strohschein, H.J.J. Seguin, C.E. Capjack, "Multi-channel

slab CO₂ laser excitation with resonant cavities,” accepted for publication in *Optics & Laser Technology*, (1996).

- 9 E.F. Yelden, S.W.C. Scott, J.D. Strohschein, H.J.J. Seguin, C.E. Capjack, and H.W. Reshef, “Symmetry Enhancement and Spot-Size Reduction Through Radial Beam Stacking in a Multi-channel CO₂ Laser Array,” *J. Quant. Elec.*, 30 (8), 1868-1875, (1994).
- 10 Personal communication with J.D. Strohschein.
- 11 Hyperpulse is a trademark of PRC Corporation, Landing, N.J.,
- 12 C.M. Sharp and R.D. Young, "Method and Apparatus for Laser Processing of Materials", United States Patent #4,752,669, June 21, 1988
- 13 H.J.J. Seguin, A.K. Nam and J. Tulip, "The Photoinitiated Impulse-Enhanced Electrically Excited (PIE) Discharge for High-Power CW laser Applications," *Appl. Phys. Lett.*, 32, 418-420, (1978)
- 14 K.H. Nam, H.J.J. Seguin and J. Tulip, "Operational Characteristics of a PIE CO₂ Laser." *IEEE J. of Quant. Elec.*, QE-15, 44-50 (1979)
- 15 A.K. Nath, H.J.J. Seguin and V.A. Seguin, "Optimization Studies of a Multi-kilowatt PIE CO₂ Laser," *IEEE Journal of Quantum Electronics*, QE-22, 269-274 (1986)
- 16 S. K. Nikumb, H. J. J. Seguin, V. A. Seguin, R. J. Willis and H. W. Reshef,

- "High-Average Power-Pulsed Performance of a Multikilowatt PIE Laser,"**
IEEE J. Quant. Elec. 25 (7), 1725-1735, (1989).
- 17 **S.K. Nikumb, H.J.J. Seguin, V. A. Seguin and D. Presakarchuk, "High repetition rate operation of a photoinitiated impulse-enhanced electrically excited CO₂ laser discharge using a burst-mode technique," Appl. Phys. Lett., 53, (14, Oct. (1988)**
- 18 **S. K. Nikumb, H. J. J. Seguin, V. A. Seguin, R. J. Willis, Z. Cheng and H. W. Reshef, "Burst-mode gain switched technique for high peak and average optical energy extraction," Appl. Optics 28 (9), 1624-1627, (1989).**
- 19 **S. W. C. Scott, K. Rogozinski and H. J. J. Seguin, "High peak power, burst mode operation of a multikilowatt CO₂ laser for deep penetration welding," Appl. Phys. Lett. 65 (3), 286-288, (1994).**
- 20 **S. W. C. Scott, J. D. Strohschein and H. J. J. Seguin, "Deep Penetration Welding Performance of a High Average Power, Multi-kilowatt Peak Power Carbon Dioxide Laser," Presented at the 14th International Congress on Applications of Lasers & Electro-optics - ICALEO '95, San Diego, (1995).**
- 21 **M.W. Sasnett, "Comparing Industrial CO₂ Lasers," Lasers and Applications, 85, (1984).**
- 22 **W.B. Tiffany, R. Tang and J.D. Foster, "Kilowatt CO₂ Gas Transport Laser," Appl. Phys. Lett., 15 (91), (1969).**

- 23 H.J.J. Seguin, J. Tulip and D McKen, "UV Photoionization density measurements in TEA lasers," Appl. Phys. Lett., 23 (6), (1973).
- 24 A. Thompson, "Advances in laser-pulse performance", Industrial Laser Review, 3, (9), Feb. (1989).
- 25 J.T. Verdeyen, "Laser Electronics," Prentice-Hall Series in Solid Physical Electronics, 2nd Ed., (Prentice-Hall, New Jersey, 1989)
- 26 M.W. Sasnett, "CO₂ laser design considerations for pulsed material processing", Proc. 3rd Int. Conf. Lasers in Manufacturing, Paris: Springer-Verlag, June (1986).
- 27 W. Schock, Th. Hall, E. Wildermuth, K. Wessel, E. Gehringer, P. Schnee, F. Hadinger, "Compact transverse flow CO₂ laser with RF excitation," Proc. SPIE 1031, 76-81, (1988).
- 28 A.P. Schwarzenbach and U.W. Hunziker, "Industrial CO₂ laser with high overall efficiency", SPIE 1020, (1988).
- 29 A. Thompson, "CO₂ Laser Cutting of Highly Reflective Materials", Industrial Laser Handbook-Annual review of laser processing, 149-153, (1988).
- 30 Data supplied by the PRC Corporation. Landing NJ.
- 31 C.M. Sharp and C.J. Nilsen, "The Development and Implementation of High-Speed Laser Beam Welding in the Can-Making Industry", Welding Journal,

Jan. (1988).

- 32 V.P. Garashchuk, O.A. Velichko and V.B. Davydova, "Effects of the Mean Intensity of Illumination in a Spot of Light, and of Defocusing, on the Depth of Penetration During Pulsed Laser Welding," Automatic Welding, 24, 29-34 (1971)
- 33 N.G. Basov, et. al., "Physico-technological special features of laser welding in continuous and pulse-periodic regimes," Welding Production, 8, 5-7, (1985).
- 34 S.V. Drobyazko, et. al., "Weld formation in welding with the radiation of a pulsed periodic CO₂ laser," Welding International, 1, 19-21, (1989).
- 35 S. Kimura, N. Sano, S. Sugiyama and M. Mizutame, "Welding Properties with High Power Pulsed CO₂ Laser," Proc. LAMP '87, 169-174, (1987).
- 36 M.H. McCay, T.D. McCay, N.B. Dahotre, C.M. Sharp, A. Sedghinasab and S. Gopinathan, "Pulsed Laser Welding of INCO 718," L.I.A. ICALEO '89 69, 229-238,(1989).
- 37 A. G. Grigor'yants, et al., "Technological possibilities of welding and cutting metals with a peak radiation structure,' Welding Production, 11, 10-12, (1986)
- 38 B. Basu, "Critical Heat Transfer Analysis of Pulsed Laser Melting of Pure Metals," Appl. Phys. Lett., 58, 6 (1991).
- 39 V.K. Lebedev, V.T. Granitsa and V.F. Garashchuk, "Effects of Radiation Pulse

- Shape on the Depth of Penetration Zone in Laser-Beam Welding," *Automatic Welding*, 26, 9-12 (1973)
- 40 H. J. J. Seguin, A. K. Nam and J. Tulip, "An efficient multielement cathode for high-power electric discharge laser applications," *J. Appl. Phys.* 49 (8), 4566-4567, (1978).
 - 41 Z. Cheng, H. J. J. Seguin, S. K. Nikumb, V. A. Seguin, and H. Reshef, "Annular-coupled concave-convex stable resonator for large-volume high-quality energy extraction," *Appl. Optics*, 27 (5), 836-842, (1988).
 - 42 D. R. Akitt, H. J. J. Seguin, M. R. Cervenak and S. K. Nikumb, "Electronic Mode and Power Control of a High-Power CO₂ Laser," *IEEE J. Quant. Elec.* 26 (8), 1413-1417, (1990).
 - 43 C. V. Sellathamby, H. J. J. Seguin and S. K. Nikumb, "Performance characteristics of a high power CO₂ laser with computer vision mode and power control," *Appl. Optics* 29 (30), 449-4503, (1990).
 - 44 V.E. Merchant, H.J.J. Seguin and J. Dow, "Novel transformer designs for high-power high-repetition-rate applications," *Rev. Sci. Instrum.*, 50, 9, (1979)
 - 45 A.V. Oppenheim, A.S. Willsky, "Signals and Systems," Prentice-Hall Signal Processing Series, 53, (Prentice-Hall, New Jersey, 1983).
 - 46 D.E. Marshall, "A Review of Pyroelectric Detector Technology," *SPIE* 132, (1978).

- 47 J. Piotrowski, W. Galus and M. Grudzien, "Near Room-Temperature IR Photo-Detectors," *Infrared Phys.*, 31 (1), 1-48, (1991).
- 48 Vigo Sensor, Model PEM-L-2, Boston Electronics, Brookline, MA.
- 49 H. J. J. Seguin, V. A. Seguin, A. K. Nath and J. Radzion, "Spinning water film power meter for high-power CW lasers," *Rev. Sci. Instr.* 57 (2), 185-190, (1986).
- 50 C.V. Sellathamby, "A Computer Vision System for On-Line Laser Beam Control and Diagnostics," PhD Thesis, University of Alberta, (1992).
- 51 K. Rogozinski, S.W.C. Scott and H.J.J. Seguin, "Direct Visualization of the Focal Parameters of a High Power CO₂ Laser Beam," *Rev. Sci. Instrum.*, 65 (12), 3616-3620, (1994).
- 52 S. Hiramoto, M. Ohmine, T. Okuda, Y. Myoi, M. Hishii, H. Nagai and A. Shinmi, "Deep Penetration Welding with High Power CO₂ Laser," *Electron and Laser Beam Welding, Proc. of Conf., Tokyo* (1986)
- 53 M. Funk, U. Kohler, K. Behler and E. Beyer, "Welding of Steel with a CO₂ Laser of 20 kW," *SPIE* 1132, 174-180, (1989)
- 54 J. H. P. C. Megaw, M. Hill and S. J. Osbourn, *SPIE* 650 311 (1986)
- 55 L. Garifo and A. Sona, "The State of the Art and the Trends in High Power CO₂ Lasers for Materials Processing," *High Power Lasers and Their Industrial*

Applications: Divisional Meeting of the Quantum Electronics Division/European Physical Society, Dieter S

- 56 L. Mannik and S.K. Brown, "A Relationship Between Laser Power, Penetration Depth and Welding Speed in the Laser Welding of Steels," Journal of Laser Applications, Summer/Fall, 22-25 (1990)**
- 57 D.R. Martyr and T. Holt, "High power laser processing of materials", High Power Lasers: Sources, Laser-Material Interactions, High Excitations, and Fast Dynamics in Laser Processing and Industrial Applications, E.W. Kreutz, A. Quenzer, D. Schuocker, editor**

Appendix A

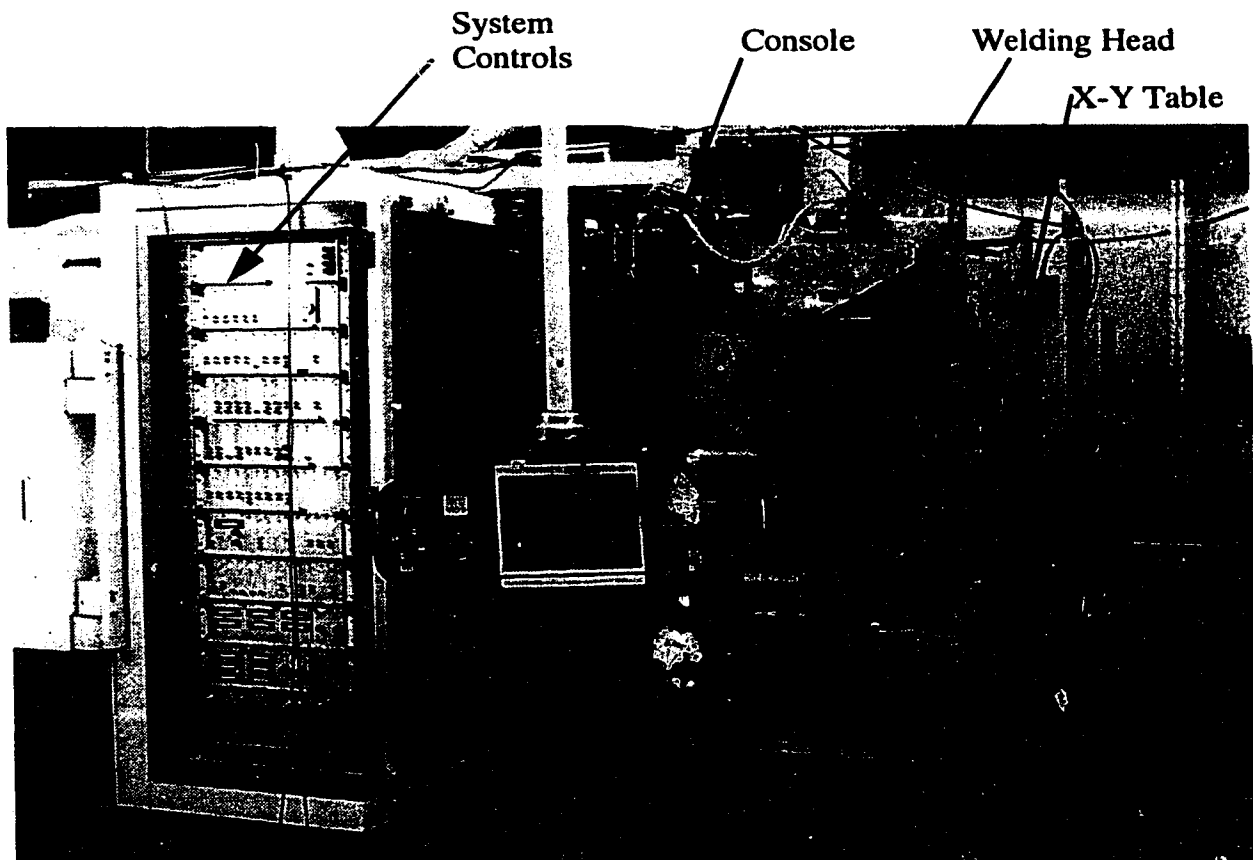


Figure A.1: PIE IV Laser system illustrating the operators console, welding head, X-Y table and system controls.

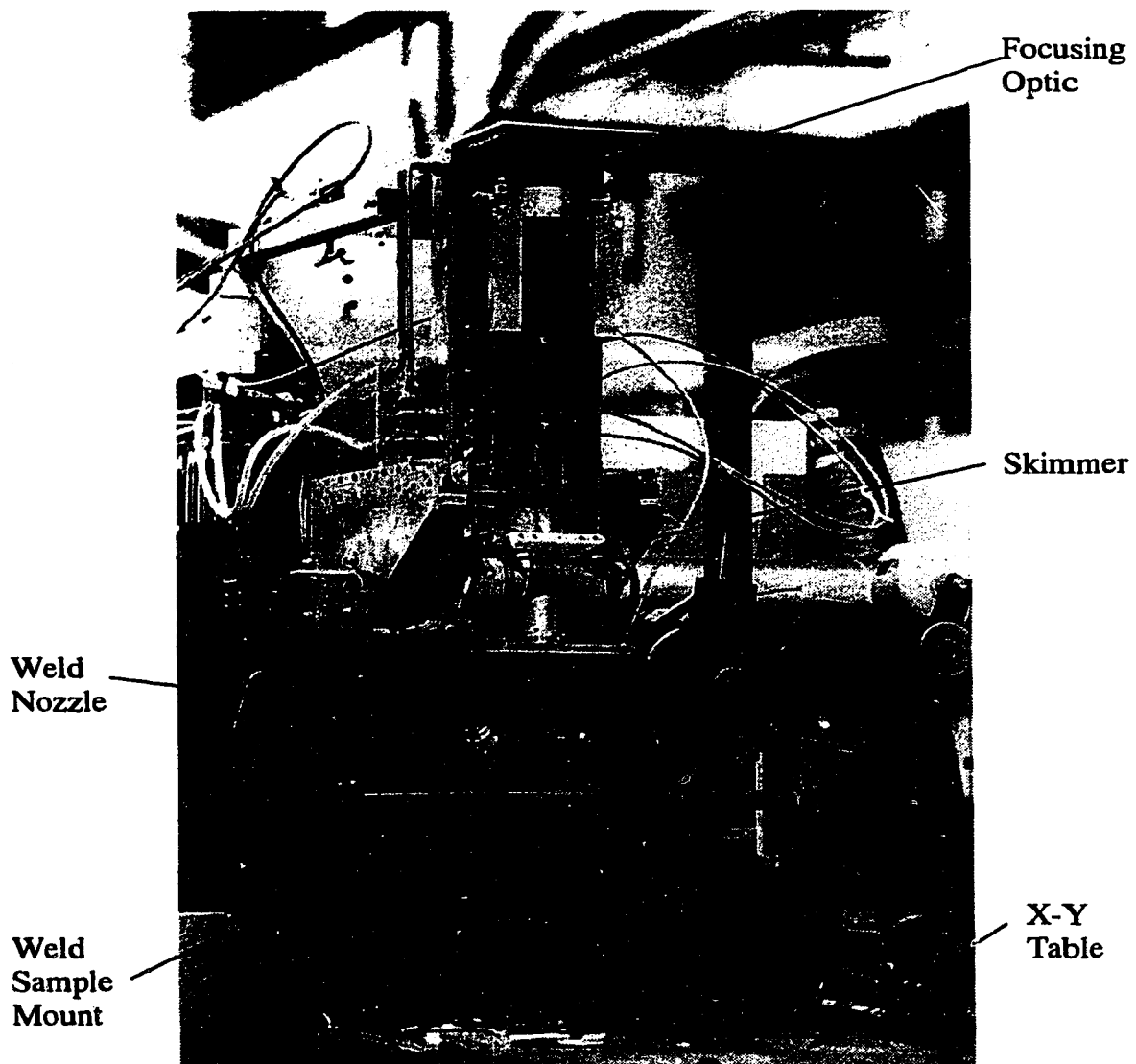


Figure A.2: Laser welding head illustrating beam handling optics, welding nozzle, X-Y table, and weld sample mount.

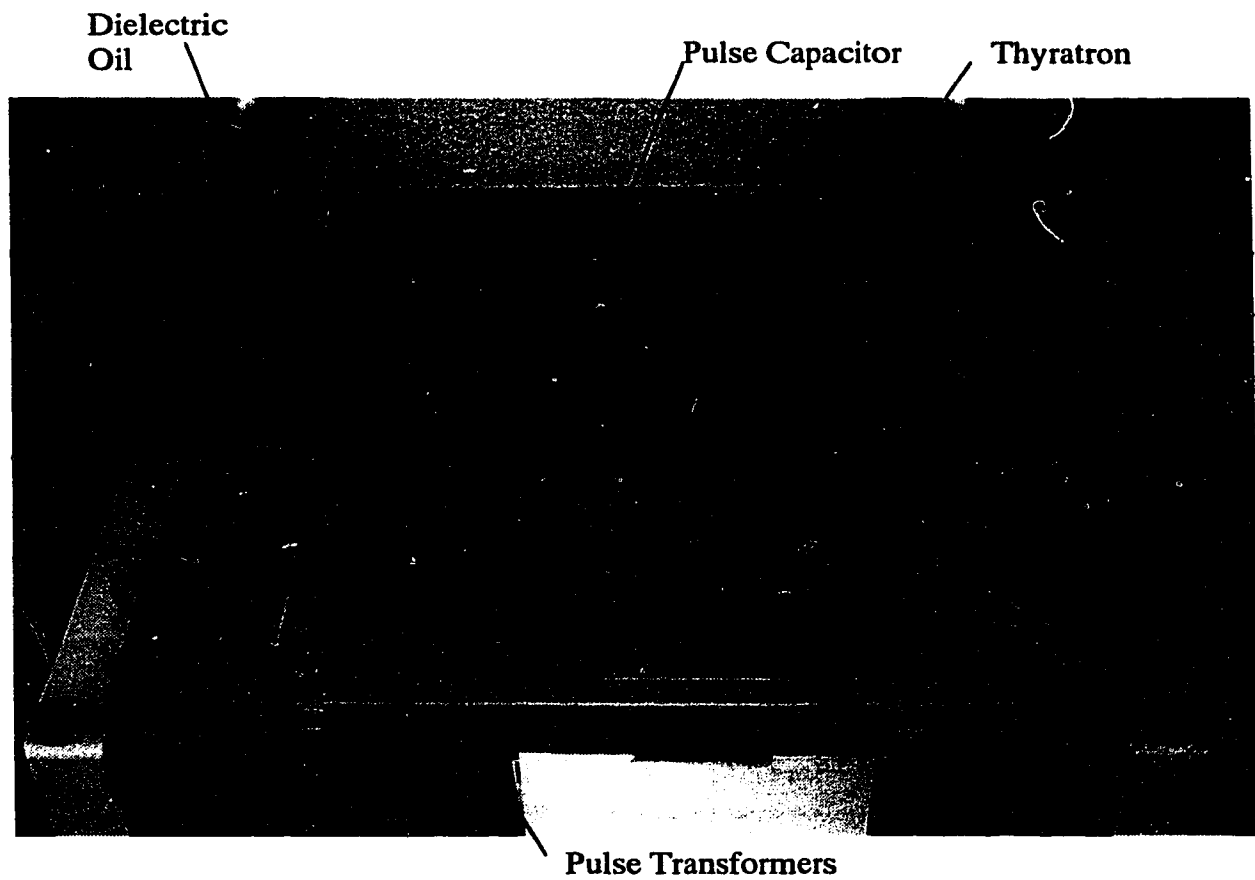


Figure A.3: Laser pulser control box illustrating the oil immersed hydrogen thyratron, pulse capacitors pulse transformers and high voltage connections.



Figure A.4: Typical laser beam burn pattern in fire brick.

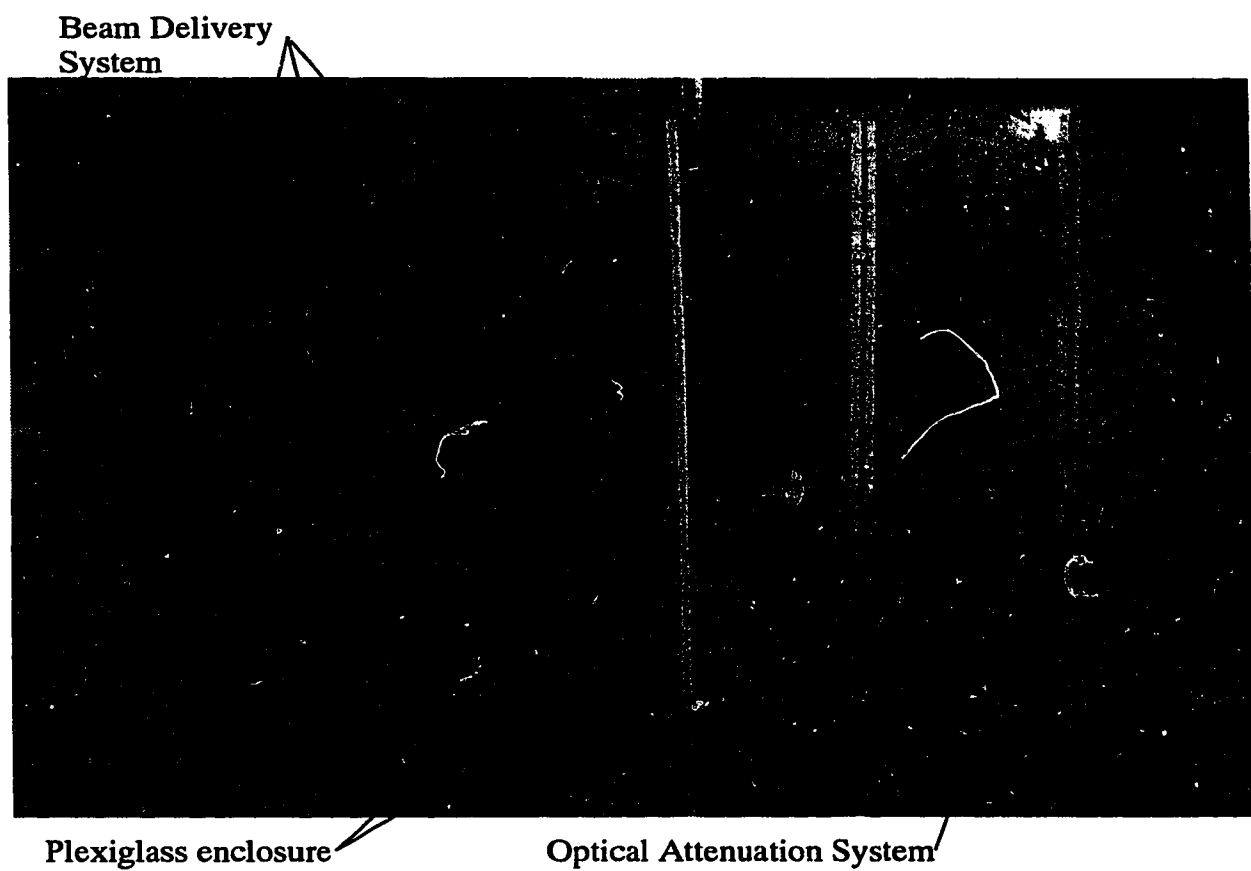


Figure A.5: Optical bench safety enclosure illustrating the beam delivery and optical attenuation system.

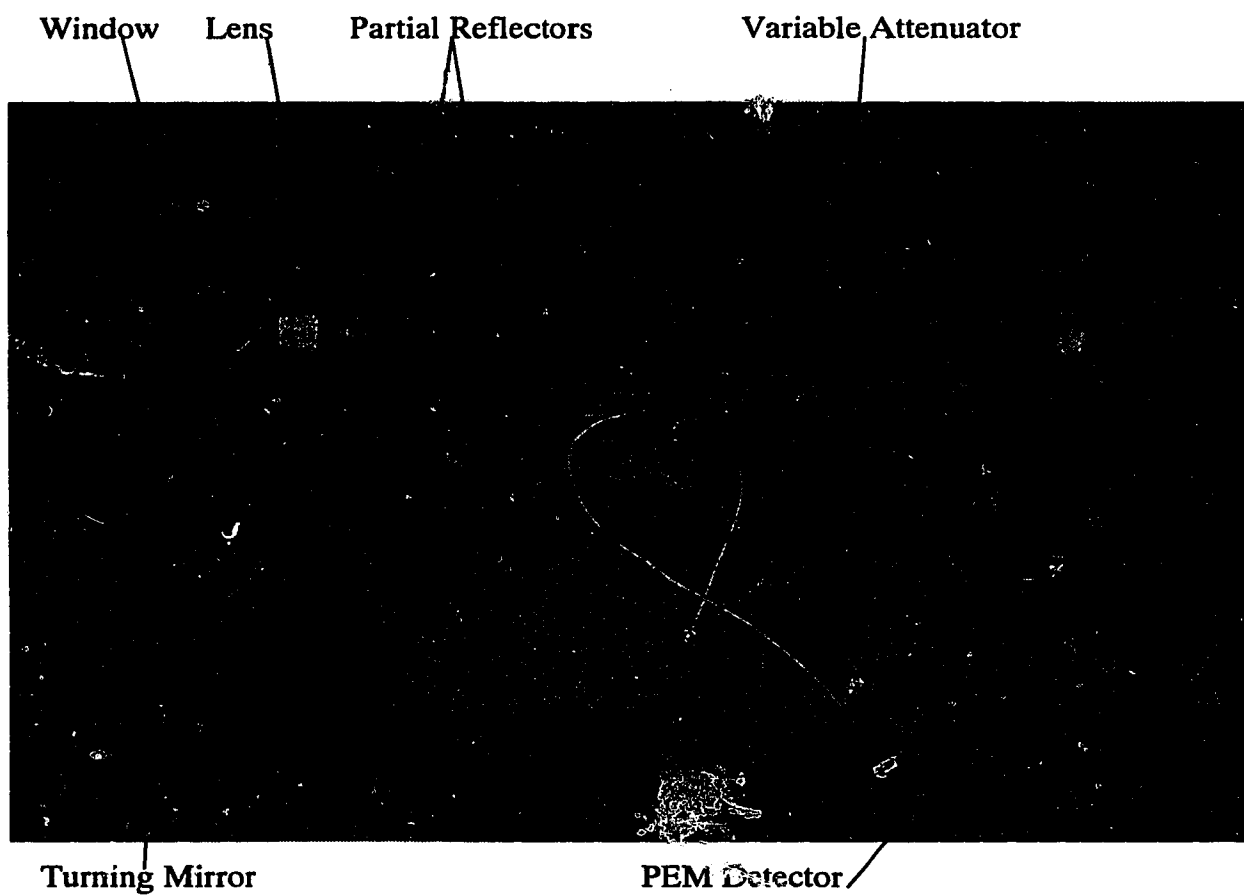


Figure A.6: Overhead view of the optical attenuation system and PEM detector apparatus.